INL/EXT-23-63549-R001

Fission Product Transport in TRISO Particles and Pebbles

January 2023

Technical Report

Wen Jiang[1], Aysenur Toptan[1], Russell Gardner[2], Jason D. Hales[1], Albert Casagranda[1], Benjamin W. Spencer[1], and Stephen Novascone[1]

[1]Idaho National Laboratory
[2]Kairos Power

INL is a U.S. Department of Energy National Laboratory operated by Battelle Energy Alliance, LLC

Fission Product Transport in TRISO Particles and Pebbles

Technical Report

Wen Jiang[1], Aysenur Toptan[1], Russell Gardner[2], Jason D. Hales[1], Albert Casagranda[1], Benjamin W. Spencer[1], and Stephen Novascone[1]

[1]Idaho National Laboratory
[2]Kairos Power

January 2023

Idaho National Laboratory
Computational Mechanics and Materials Department
Idaho Falls, Idaho 83415

http://www.inl.gov

Prepared for the
U.S. Department of Energy
Office of Nuclear Energy
Under DOE Idaho Operations Office
Contract DE-AC07-05ID14517

Page intentionally left blank

Abstract

This document demonstrates completion of the goals described in the technical narrative of the FOA project titled: "Modeling and Simulation Development Pathways to Accelerating KP-FHR Licensing" regarding fission product transport in the Kairos-proposed fuel pebble by Idaho National Laboratory and Kairos Power. Showcased in this report are code developments and simulations in BISON that extend the state of the art in computation and understanding of fission product transport in a TRISO fuel particle and pebble. These enhancements lay the foundation for making predictions of fission product transport that can be used as input in the fuel licensing process. This was achieved by installing existing fuel material models originally used in PARFUME, developing a new failure probability method that is efficient and multidimensional, employing material homogenization, and expanding verification and validation simulations to demonstrate the efficacy of the work. All this work is leveraged to spotlight the main deliverable—a three-dimensional model and corresponding demonstration simulation of a pebble, which will serve as the starting point for models used to predict fission product release.

Page intentionally left blank

Acknowledgments

This manuscript has been authored by Battelle Energy Alliance, LLC, under Contract No. DE-AC07-05ID14517 with the U.S. Department of Energy. The U.S. Government retains and the publisher, by accepting the article for publication, acknowledges that the U.S. Government retains a nonexclusive, paid-up, irrevocable, world-wide license to publish or reproduce the published form of this manuscript, or allow others to do so, for U.S. Government purposes.

This research made use of the resources of the High Performance Computing Center at Idaho National Laboratory, which is supported by the Office of Nuclear Energy of the U.S. Department of Energy and the Nuclear Science User Facilities under Contract No. DE-AC07-05ID14517.

Page intentionally left blank

Contents

List of Figures

List of Tables

Acronyms

AGR	Advanced Gas Reactor
BAF	Bacon anisotropy factor
3D	three-dimensional
CASL	Consortium for Advanced Simulation of light-water reactors (LWRs)
CO	carbon monoxide
D-EMT	differential effective medium theory
DIRK	diagonally implicit Runge-Kutta
DOE	U.S. Department of Energy
DTF	Designed-to-Fail
EMT	effective medium theory
EDC	effective diffusivity coefficient
ETC	effective thermal conductivity
FCC	face-centered cubic
FE	finite element
FEA	finite element analysis
FOA	Funding Opportunity Announcement
FP	fission product
HC	hexagonal close
INL	Idaho National Laboratory
KP-FHR	The Kairos Power FHR
LTE	linear truncation error
LWR	light-water reactor
MOOSE	Multiphysics Object-Oriented Simulation Environment
PARFUME	Particle Fuel Model
PDE	partial differential equation
PIE	post-irradiation examination
PyC	pyrolytic carbon
QoI	quantity of interest

IPyC	inner pyrolytic carbon
OPyC	outer pyrolytic carbon
R/B	release-rate over birth-rate
RHS	right-hand side
SC	simple cubic
SiC	silicon carbide
TRISO	tri-structural isotropic
UCO	uranium oxicarbide
UO_2	uranium dioxide
WBS	Work Breakdown Structure

1. Introduction

Kairos Power and the Idaho National Laboratory participated in a project to enhance fuel performance modeling and simulation capability for the purpose of helping answer regulatory licensing questions about Kairos Power's new reactor regarding fission product release. The Kairos Power website states: The Kairos Power FHR (KP-FHR) is a novel advanced reactor technology that leverages TRISO fuel in pebble form combined with a low-pressure fluoride salt coolant. The technology uses an efficient and flexible steam cycle to convert heat from fission into electricity and to complement renewable energy sources (`https://kairospower.com/technology/`). This report documents the work done in that project, which enabled state-of-the-art fission product transport calculations. The work accomplished includes the implementation of particle fuel material models, creation of probabilistic tools used to assess failure, multidimensional fission product transport, and demonstrations of solution verification and validation. These developments enable a modern and accurate estimate of fission product release from particle fuel embedded in a pebble.

The technical narrative of the Funding Opportunity Announcement (FOA) project titled: "Modeling and Simulation Development Pathways to Accelerating KP-FHR Licensing" (LLC et al. (2018) henceforth referred to as the FOA) provides a description of the tasks to be accomplished; this report documents the completions of those tasks. Quoting from the FOA: "The goal of the work is to provide a robust understanding of what data is available and best modeling approaches to apply. This scope of work is broken into three categories: Work Breakdown Structure (WBS) (Work Breakdown Structure, see FOA reference) 2.1 is work performed at Idaho National Laboratory (INL) to better understand and predict fission product transport using the BISON fuel performance code, WBS 2.2 is work performed at Idaho National Laboratory (INL) in modeling the TRISO particle failure probability in the KP-FHR using capability currently being implemented in the BISON fuel performance code Williamson et al. (2021), WBS 2.3 is work performed at Kairos on the validation of BISON for KP-FHR application." Chapter 2 documents the thermal-mechanical, fission product diffusion, and fission gas models utilized for the analysis. The material model section includes Section 2.4, which describes the one-, two-, and three-dimensional (1-D, 2-D, and 3-D) meshes used in simulations that serve as good visual references to communicate mesh design, symmetry, mesh aspect ratio, and where the material models are applied. Chapter 3 showcases the extensive developments for failure probability calculation in Multiphysics Object-Oriented Simulation Environment (MOOSE) during the last 2 years, which have resulted in a robust, flexible, and more geometrically informed capability. In Chapter 4, the topic of homogenization is described, which is a necessary simplification that adequately describes the

thermal behavior of the particle fuel and pebble in a fashion that allows reasonable computation time. Verification of basic physics calculations that represent heat conduction, mass diffusion, and mechanics (stress, strain, displacement) is presented in Chapter 5. Validation using the Advanced Gas Reactor (AGR)-1 and AGR-2 data sets is shown in Chapter 6. Finally, a 3-D demonstration simulation, which will serve as the baseline for fission product release prediction calculations for regulatory licensing requirements, is presented in Chapter 7.

The first version of this report was published around June 2021 and documented the original work scope of the FOA. KP-FHR and INL were granted a no-cost extension through January of 2023, where work scope was added to compliment earlier work. This extended work consisted of:

- Simulating particles embedded in a compact with 3D features and particle-pebble thermal coupling. This demonstrates the importance of 3D effects and varying particle temperature on fission product release. You can find this in *Section* 7.4
- Implementing and exploring use of direct integration for the purpose of accuracy and computation efficiency. This is documented in *Section* 3.5
- The addition of an interface diffusion feature that simulates mass transfer across the buffer and IPyC gap. Simulating mass transfer across the gap was previously performed by the thermal contact feature. A description of this is found in *Section* 7.2.
- Further documentation on calculating and standards for reporting fission gas release are documented in *Section* 5.4.

2. Material Model Implementation

2.1 Thermal-mechanical Properties

TRISO fuel thermomechanical properties for the uranium oxicarbide (UCO) kernel and coating layers are described in this section. These include elastic, creep, swelling, thermal expansion, and thermal conductivity.

2.1.1 UCO Fuel Kernel

Legacy TRISO fuel development programs have predominantly focused on uranium dioxide (UO_2) fuel; consequently, most UCO kernel properties currently used in BISON are derived from experimental data on UO_2 and assumed valid for UCO, due to lack of relevant UCO data.

The thermal conductivity of the kernel, k (W/m-K), is given by Miller et al. (September, 2018):

$$k = 0.0132 \exp\left(0.00188 T_C\right) + \begin{cases} \dfrac{4040}{464 + T_C} & \text{for } T_C < 1650°C \\ 1.9 & \text{for } T_C \geq 1650°C \end{cases} \tag{2.1}$$

where T_C (°C) is the temperature of the kernel.

The specific heat capacity of UCO is calculated from its molar heat capacity (Fink, 2000) and molar mass:

$$c_P = \frac{1}{M}\left(52.1743 + 87.951 t_K - 84.2411 t_K^2 + 31.542 t_K^3 - 2.6334 t_K^4 - \frac{0.71391}{t_K^2}\right) \tag{2.2}$$

where c_P (J/kg-K) is specific heat capacity, $t_K = T_K/1000$ (K) is the reduced temperature, and M (kg/mol) is the molar mass. The molar mass of the kernel, M (kg/mol), is computed for i =UO_2, UC_2, and UC by:

$$M = \sum_i^N af_i \times aw_i \tag{2.3}$$

with

$$af = \begin{cases} 0.5OU & \text{for } UO_2 \\ 0.5OU + CU - 1.0 & \text{for } UC_2 \\ 2.0 - (OU + CU) & \text{for UC} \end{cases} \tag{2.4}$$

and

$$aw = \begin{cases} 0.23504\epsilon + 0.23805(1.0 - \epsilon) + 0.03200 & \text{for } UO_2 \\ 0.23504\epsilon + 0.23805(1.0 - \epsilon) + 0.02402 & \text{for } UC_2 \\ 0.23504\epsilon + 0.23805(1.0 - \epsilon) + 0.01201 & \text{for UC} \end{cases} \tag{2.5}$$

where ϵ (wt.%) is the initial U-235 enrichment, OU (-) and CU (-) are the initial oxygen-to-uranium and carbon-to-uranium stoichiometries of UCO, af (-) is the atomic fraction, and aw (kg/mol) is the atomic weight. The atomic weights of the UCO constituents are tabulated in Table 2.1.

Table 2.1. Atomic weights of the UCO constituents.

	aw (g/mol)
uranium-235	235.04
uranium-238	238.05
oxygen	16.00
carbon	12.01

The following temperature-dependent Young's modulus of the kernel was obtained by digitizing a plot in Olander (1976) and by fitting the resulting curve:

$$E = 219(1.0 - 1.07 \times 10^{-4} T_C - 2.16 \times 10^{-7} T_C^2 + 3.10 \times 10^{-10} T_C^3 - 1.54 \times 10^{-13} T_C^4) \left(\frac{1.92\rho - 0.92\rho_{th}}{\rho_{th}} \right) \tag{2.6}$$

where E (GPa) is Young's modulus of the kernel, T_C (°C) is the temperature of the kernel, ρ (g/cm^3) is the density of the kernel, and ρ_{th} (g/cm^3) is the theoretical density of UCO.

The theoretical density of the kernel, ρ_{th} (kg/m^3), is calculated as:

$$\rho_{th} = \frac{1}{\frac{wf_{UO_2}}{\rho_{th}^{UO_2}} + \frac{wf_{UC}}{\rho_{th}^{UC}} + \frac{wf_{UC_2}}{\rho_{th}^{UC_2}}} \tag{2.7}$$

$$wf = \frac{af \cdot aw}{M} \tag{2.8}$$

where wf (-) is the weight fraction of each component. The theoretical densities of the UCO mixture components are tabulated in Table 2.2.

Table 2.2. Theoretical densities of the UCO mixture components.

	ρ_{th} (g/cm^3)
UO_2	10.96
UC	13.63
UC_2	11.28

The Poisson's ratio of the kernel, ν (-), is given by:

$$\nu = 1.35\left(\frac{1.92\rho - 0.92\rho_{th}}{1.66\rho - 0.66\rho_{th}}\right) - 1 \tag{2.9}$$

where ρ (g/cm^3) is the density of the kernel and ρ_{th} (g/cm^3) is the theoretical density of UCO.

Kernel swelling occurs throughout irradiation as solid and gaseous atoms released by fission accumulate in the kernel, resulting in a volume increase of the kernel. The volumetric fission-induced swelling model of UCO is taken from the PARFUME code and assumes a constant rate of volume increase due to fission:

$$\Delta\epsilon_{sw} = 2.9\Delta Bu \tag{2.10}$$

where $\Delta\epsilon_{sw}$ (-) is the volumetric swelling increment of the kernel and ΔBu (fissions/atoms-U) is the burnup increment.

2.1.2 Buffer

The thermal conductivity of the buffer is taken from the PARFUME code:

$$k = \frac{k_{init}k_{theo}\rho_{theo}(\rho_{theo} - \rho_{init})}{k_{theo}\rho_{theo}(\rho_{theo} - \rho) + k_{init}\rho(\rho - \rho_{init})} \tag{2.11}$$

where k (W/m-K) is the thermal conductivity of the buffer and ρ (kg/m^3) is the density of the buffer. The values at initial (ρ_{init}) and theoretical ($\rho_{theo} = 2250$ kg/m^3) densities are taken from Ho (July, 1993).

The initial thermal conductivity (k_{init}) of the buffer is set to 0.5 W/m-K. It is intended for an initial buffer density of 1000 kg/m^3 but is also used for slightly different densities ($\pm$ 10%). Thermal conductivity of the buffer at its theoretical density (k_{theo}) is set to 4.0 W/m-K.

The specific heat capacity of the buffer is given by Barabash et al. (2002) as 720 J/kg-K.

The isotropic coefficient of thermal expansion of the buffer is given by Miller et al. (September, 2018); Ho (July, 1993):

$$\alpha = 5\left(1 + 0.11\left[\frac{T_C - 400}{700}\right]\right) \tag{2.12}$$

where T_C (°C) is the temperature of the buffer. The thermal expansion strain is calculated as:

$$\epsilon_{te} = \alpha(T_K - T_{StressFree}) \tag{2.13}$$

where T_K (K) is the temperature of the buffer and $T_{StressFree}$ (K) is the stress-free temperature.

The Young's modulus of the buffer, E (GPa), is given by Miller et al. (September, 2018); Ho (July, 1993):

$$E = 25.5 \times (0.384 + 0.324 \times 10^{-3}\rho)(1.0 + 0.23\phi)(1.0 + 1.5 \times 10^{-4}[T_C - 20]) \tag{2.14}$$

where ρ (kg/m^3) is the density of the buffer, ϕ (10^{25} n/m^2, E >0.18 MeV) is the fast neutron fluence, and

T_C (°C) is the temperature of the buffer.

The Poisson's ratio of the buffer is set to a constant value of 0.33 (Miller et al., September, 2018; Ho, July, 1993).

The irradiation creep of the buffer and pyrolytic carbon (PyC), which leads to their gradual deformation in response to irradiation-induced damage, is directly proportional to the fast neutron fluence. The irradiation creep correlations for the buffer and PyC are taken from Petti et al. (December, 2004); Powers and Wirth (2010); Hales et al. (2013). With K (m^2/MPa-n) as the creep constant, σ_i as one of the principal stresses, ν_c as the Poisson's ratio for creep, and Φ (10^{25} n/m^2, E >0.18 MeV) as the fast neutron fluence, the creep rate is computed as:

$$\dot{\epsilon}_1 = K[\sigma_1 - \nu_c(\sigma_2 + \sigma_3)]\dot{\Phi} \tag{2.15}$$

where

$$K = K_0[1 + 2.38(1.9 - \rho)]M_{\text{Irr,Creep}}. \tag{2.16}$$

The steady-state creep coefficient, K_0, is given by Miller et al. (September, 2018) as:

$$K_0 = 2.193 \times 10^{-29} - 4.85 \times 10^{-32}T + 4.0147 \times 10^{-35}T^2 \tag{2.17}$$

where $M_{\text{Irr,Creep}} = 2$, ρ is in g/cm^3, and T is in °C and bounded by 600°C and 1350°C. The irradiation-induced creep coefficient is plotted at different temperatures and densities in Figure 2.1.

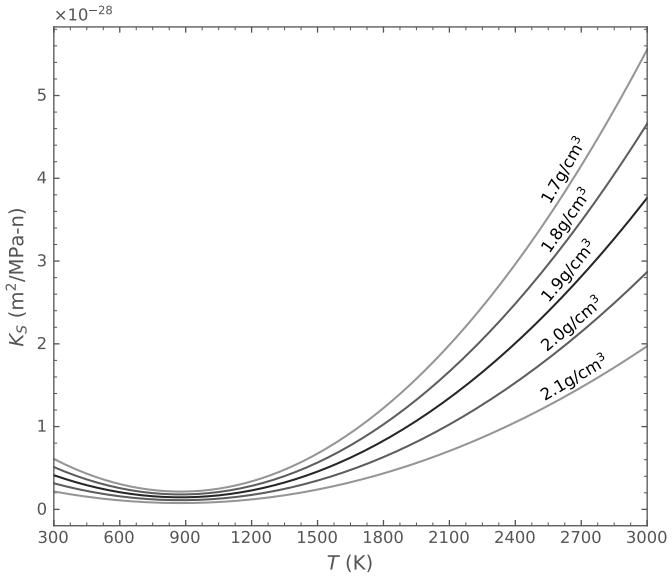

Figure 2.1. Temperature-dependent, irradiation-induced creep coefficient for the buffer layer at various densities.

The Poisson's ratio for creep in the buffer is set to a constant value of 0.5 (Miller et al., September, 2018;

Ho, July, 1993).

The buffer experiences isotropic irradiation-induced strain, given by Miller et al. (September, 2018); Ho (July, 1993):

$$\epsilon_{iso} = a_1\phi + a_2\phi^2 + a_3\phi^3 + a_4\phi^4 \tag{2.18}$$

where ϕ (10^{25} n/m^2, E >0.18 MeV) is the fast neutron fluence and a_1 through a_4 are temperature-dependent polynomial coefficients given in Figure 2.2. The polynomial coefficients at other temperatures are interpolated from Figure 2.2 and tabulated in Table 2.3.

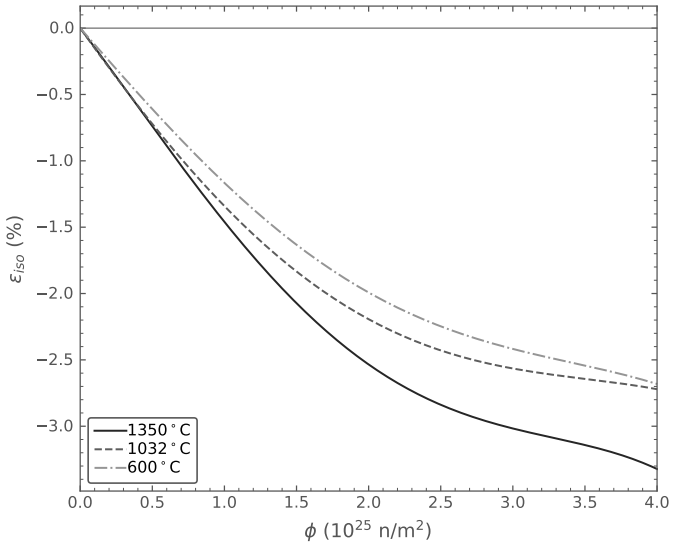

Figure 2.2. Buffer irradiation-induced isotropic strain at a density of 1.96 g/cm^3.

Table 2.3. Polynomial coefficients for the irradiation-induced strain in the buffer material at a density of 1.96 g/cm^3.

T (°C)	a_1	a_2	a_3	a_4
1350	-1.42840	-0.19563	0.18991	-0.02591
1032	-1.52390	0.13048	0.06299	-0.01072
600	-1.24080	0.00175	0.08533	-0.01253

For other densities, ϵ_{iso} is adjusted by applying a multiplier, given by $\mu = f(\rho)/f(\rho_0 = 1.96)$ where ρ (g/cm^3) is the density of the buffer. The isotropic density scaling factor is calculated using the values in Table 2.4, showing the relationship between isotropic strain and density at an irradiation temperature of 1100°C and a fast fluence of 3.7×10^{25} n/m^2 (E >0.18 MeV).

Table 2.4. Isotropic strain at an irradiation temperature of 1100°C and a fast fluence of 3.7×10^{25} n/m^2 (E >0.18 MeV).

$\boldsymbol{\rho}$ **(g/cm^3)**	1.0	1.2	1.4	1.5	1.6	1.8	1.9	1.96	2.0
$\boldsymbol{f(\rho)}$	-16.15	-13.11	-9.98	-8.93	-6.97	-4.42	-3.41	-2.75	-2.33

2.1.3 PyC

The thermal conductivity of the PyC layers is 4 W/m-K (Miller et al., September, 2018). The specific heat capacity is 720 J/kg-K (Barabash et al., 2002).

The radial and tangential coefficients of thermal expansion of PyC are given by Miller et al. (September, 2018). The thermal expansion strains, ϵ_i (-), for i = radial, tangential are:

$$\epsilon_i = \alpha_i \left(T - T_{StressFree}\right) \tag{2.19}$$

where α_i is the thermal expansion coefficient (1/K), T (K) is the temperature, and $T_{StressFree}$ (K) is the stress-free temperature.

Thermal expansion coefficients, α_i (10^{-6}/K), for i = radial, tangential are:

$$\alpha_r = (30 - 37.5R_r)\left(1 + 0.11\left[\frac{T-673}{700}\right]\right) \tag{2.20}$$

and

$$\alpha_t = \left(36[R_t - 1]^2 + 1\right)\left(1 + 0.11\left[\frac{T-673}{700}\right]\right) \tag{2.21}$$

with

$$R_r = \frac{2}{2+BAF} \quad \text{and} \quad R_t = \frac{1+BAF}{2+BAF} \tag{2.22}$$

where R_i (-) is the orientation parameter in the i-th direction and T (K) is the temperature. The BAF is a direct measure of the crystallographic anisotropy of pyrolytic carbon coatings deposited on spherical fuel particles. The BAF increases with fast fluence, and the ratio of irradiated to unirradiated BAF values is tabulated in Table 2.5 as a function of fast fluence.

Table 2.5. BAF vs. fast neutron fluence (E > 0.18 MeV).

$\boldsymbol{\phi}$ **(x10^{25} n/m^2)**	0.0	1.0	2.0	3.0	3.5	4.0	4.5	≥5.0
BAF/BAF$_0$	1.0000	1.0019	1.0114	1.0219	1.0286	1.0324	1.0362	1.0381

The Young's modulus of the PyC layers is given by Miller et al. (September, 2018); Ho (July, 1993). The elastic modulus, E (GPa), is computed as:

$$E = \frac{E_r + E_t}{2} \tag{2.23}$$

with its radial and tangential components, E_r and E_t, as:

$$E_r = 25.5(0.384+0.324\times10^{-3}\rho)(1.463-0.463BAF_0)(2.985-0.0662L_c)(1+0.23\phi)[1+0.00015(T-20)] \quad (2.24)$$

and

$$E_t = 25.5(0.384+0.324\times10^{-3}\rho)(0.481+0.519BAF_0)(2.985-0.0662L_c)(1+0.23\phi)[1+0.00015(T-20)] \quad (2.25)$$

where ρ (kg/m^3) is the density, BAF_0 (-) is the as-fabricated BAF, L_c (Å) is the crystallite diameter, ϕ (10^{25} n/m^2, $E > 0.18$ MeV) is the fast neutron fluence, and T (°C) is the temperature. The default value of L_c is set at 30 Å, so the factor of that term takes a value of one. The PyC elastic modulus is plotted at different temperatures, fluences, and BAFs in Figure 2.3.

The Poisson's ratio is set to a constant value of 0.33 (Miller et al., September, 2018; Ho, July, 1993).

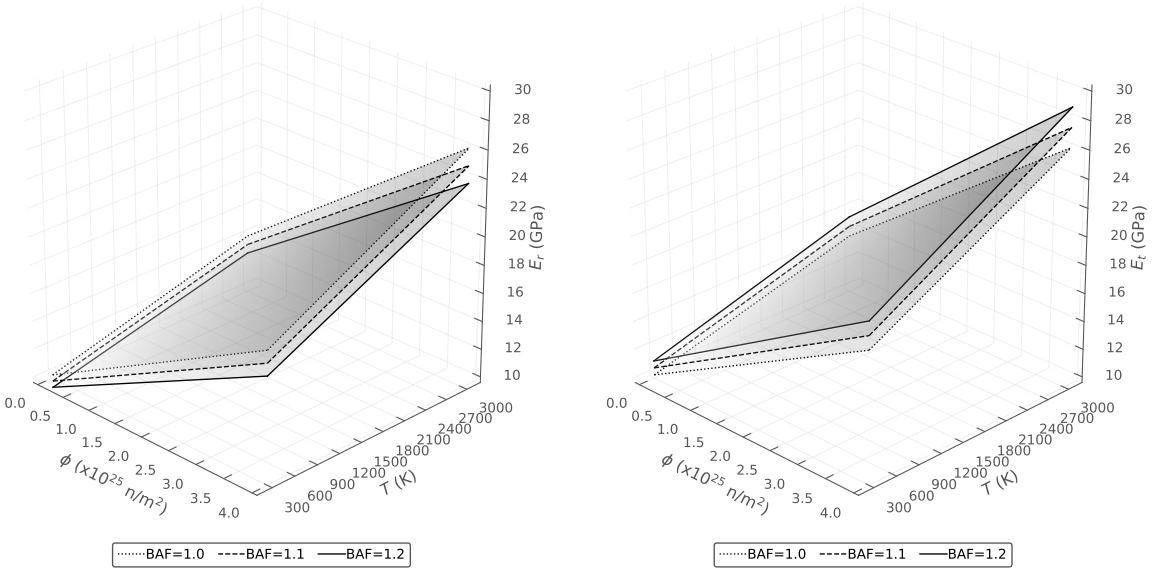

(a) Radial.

(b) Tangential.

Figure 2.3. Elastic modulus of PyC as a function of fluence and temperature for various values of BAF.

The irradiation creep model for the PyC is the same as for the buffer. The Poisson's ratio for creep of the PyC layers is set to a constant value of 0.5.

Under irradiation, PyC shrinks in both the radial and tangential directions. At modest fast neutron fluences, however, it begins to swell in the radial direction. The anisotropic strains, ε_i (-), for i = radial,

tangential, and isotropic are given by Miller et al. (September, 2018); Ho (July, 1993):

$$\varepsilon_i = a_1\phi + a_2\phi^2 + a_3\phi^3 + a_4\phi^4, \tag{2.26}$$

where ϕ (10^{25} n/m^2, E >0.18 MeV) is the fast neutron fluence and a_1 through a_4 are BAF- and temperature-dependent polynomial coefficients, listed in Table 2.6 and Table 2.7 in terms of the tangential and radial components, respectively. The polynomial coefficients at other temperatures are interpolated or extrapolated from these tables, while at other BAFs they are only interpolated from these tables. The PyC radial and tangential strains computed using these coefficients are plotted in Figure 2.4a and Figure 2.4b, respectively.

Table 2.6. Polynomial coefficients for PyC radial strain components.

		BAF					
		1.0000	**1.0212**	**1.0488**	**1.0769**	**1.1746**	**1.2787**
600°C	$\mathbf{a_1}$	-1.24080	-1.10640	-0.94333	-0.78045	-0.15714	0.40265
	$\mathbf{a_2}$	0.00175	-0.03128	-0.03589	-0.02975	-0.14889	-0.16501
	$\mathbf{a_3}$	0.08533	0.09184	0.08184	0.06655	0.07546	0.03676
	$\mathbf{a_4}$	-0.01253	-0.01220	-0.00958	-0.00626	-0.00293	0.00706
1032°C	$\mathbf{a_1}$	-1.52390	-2.07520	-2.00470	-1.81690	-1.18540	-0.45900
	$\mathbf{a_2}$	0.13048	1.37845	1.30380	1.10850	0.64995	0.51172
	$\mathbf{a_3}$	0.06299	-0.48993	-0.37280	-0.23868	0.01380	-0.03245
	$\mathbf{a_4}$	-0.01072	0.06602	0.04538	0.02484	-0.01284	-0.00142
1350°C	$\mathbf{a_1}$	-1.42840	-1.54330	-1.49640	-0.89522	1.20930	3.71620
	$\mathbf{a_2}$	-0.19563	0.59804	1.16621	0.80331	-0.53861	-2.70420
	$\mathbf{a_3}$	0.18991	-0.09997	-0.30106	-0.09009	0.43114	1.17990
	$\mathbf{a_4}$	-0.02591	0.00978	0.03475	0.00467	-0.05590	-0.13910

Table 2.7. Polynomial coefficients for PyC tangential strain components.

		BAF					
		1.0000	**1.0303**	**1.0769**	**1.1250**	**1.2258**	**1.3333**
600°C	$\mathbf{a_1}$	-1.24080	-1.38550	-1.46790	-1.64660	-1.84990	-2.19190
	$\mathbf{a_2}$	0.00175	0.05307	-0.02836	0.03928	-0.09358	0.02675
	$\mathbf{a_3}$	0.08533	0.07620	0.12139	0.10067	0.18119	0.15352
	$\mathbf{a_4}$	-0.01253	-0.01245	-0.01948	-0.01764	-0.03036	-0.02972
1032°C	$\mathbf{a_1}$	-1.52390	-1.57590	-1.32200	-1.18700	-0.96963	-0.81239
	$\mathbf{a_2}$	0.13048	0.09019	-0.51928	-0.90635	-1.59110	-2.20760
	$\mathbf{a_3}$	0.06299	0.05306	0.27603	0.41046	0.64689	0.88496
	$\mathbf{a_4}$	-0.01072	-0.00815	-0.03465	-0.05067	-0.07682	-0.10457
1350°C	$\mathbf{a_1}$	-1.42840	-2.24680	-2.82930	-3.25550	-4.44780	-5.67140
	$\mathbf{a_2}$	-0.19563	0.48243	0.76088	0.90423	1.60320	2.41920
	$\mathbf{a_3}$	0.18991	-0.07687	-0.22314	-0.33175	-0.58683	-0.86155
	$\mathbf{a_4}$	-0.02591	0.00464	0.02431	0.04329	0.07458	0.10668

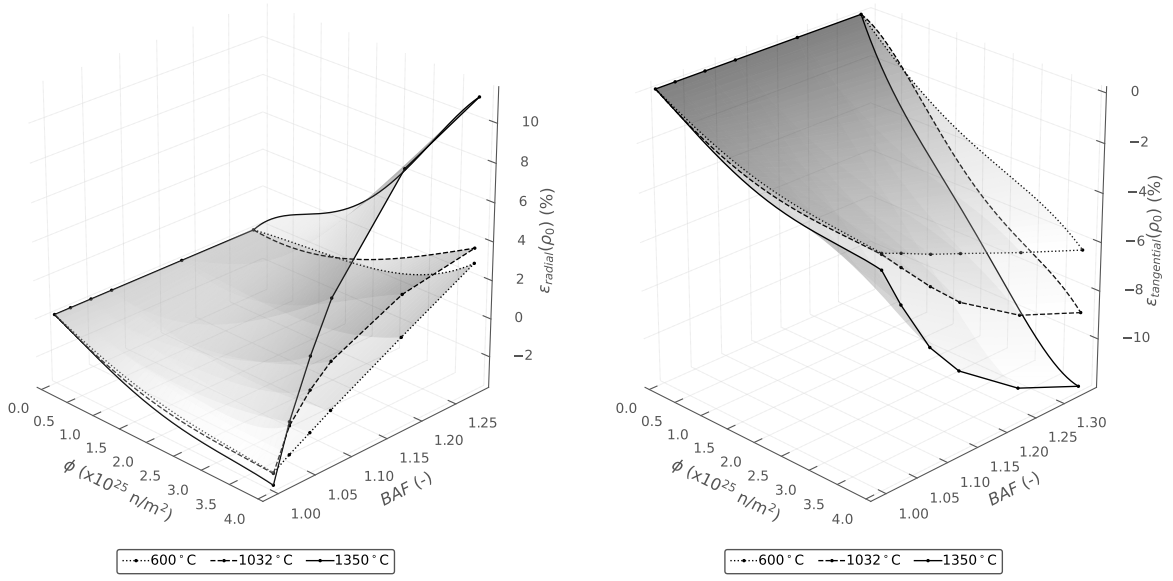

(a) Radial.

(b) Tangential.

Figure 2.4. PyC (a) radial and (b) tangential strain at $\rho_0 = 1.96\,\mathrm{g/cm^3}$ as a function of BAF and fluence for various temperatures.

Adjustments for PyC with other densities are made by applying an anisotropic scaling factor, ν. This factor is defined as the ratio of the difference between the radial and tangential strain components at a given density to the difference between the radial and tangential strain components at $\rho_0 = 1.96\,\mathrm{g/cm^3}$:

$$\nu = \frac{\varepsilon_r(\rho) - \varepsilon_t(\rho)}{\varepsilon_r(\rho_0) - \varepsilon_t(\rho_0)} \tag{2.27}$$

The anisotropic scaling factor is calculated using the values in Table 2.8, which shows the relationship between the difference in the radial and tangential strain components and the density at an irradiation temperature and fast fluence. Thus, the adjusted radial and tangential strains become:

$$\varepsilon_r(\rho) = \mu\varepsilon_{iso}(\rho_0) + \nu\left[\varepsilon_r(\rho_0) - \varepsilon_{iso}(\rho_0)\right] \tag{2.28}$$

$$\varepsilon_t(\rho) = \mu\varepsilon_{iso}(\rho_0) + \nu\left[\varepsilon_t(\rho_0) - \varepsilon_{iso}(\rho_0)\right] \tag{2.29}$$

Table 2.8. Isotropic and anisotropic strain of PyC at an irradiation temperature of 1100°C and a fast fluence of 3.7 x 10^{25} n/m^2 (E >0.18 MeV).

ρ (g/cm^3)	1.00	1.20	1.40	1.50	1.60	1.80	1.90	1.96	2.00
ε_{iso} (%)	-16.15	-13.11	-9.98	-8.93	-6.97	-4.42	-3.41	-2.75	-2.33
ε_r - ε_t (%)	0.000	0.500	1.100	1.650	2.450	6.305	7.900	9.600	11.100

2.1.4 SiC

The thermal conductivity model for SiC is given by Miller et al. (September, 2018):

$$k = \frac{17885}{T_K} + 2.0 \tag{2.30}$$

where k (W/m-K) is the thermal conductivity and T_K (K) is the temperature.

The correlation for specific heat capacity, c_P (J/kg-K), is given by Snead et al. (2007):

$$c_P = 925.65 + 0.3772T - 7.9259 \times 10^{-5}T^2 - \frac{3.1946 \times 10^7}{T^2} \tag{2.31}$$

where T (K) is the temperature.

The thermal expansion coefficient is 4.9×10^{-6} (1/K) (Miller et al., September, 2018; Ho, July, 1993).

The Young's modulus and Poisson's ratio of SiC is given by Miller et al. (September, 2018).

The Young's modulus (E) is temperature-dependent and given according to Table 2.9. For values between the tabulated values, linear interpolation is used. For temperatures below 25.0°C, Young's modulus is taken as 428.0 GPa. For temperatures above 1600°C, a value of 198.0 GPa is used.

Table 2.9. Elastic modulus of SiC as a function of temperature.

T (°C)	25.0	940.0	1215.0	1600.0
E (GPa)	428.0	375.0	340.0	198.0

Poisson's ratio is set to a constant value of 0.13.

2.2 Fission Product Diffusion

Several mechanisms can be involved in the transport of mobile fission products through the kernel and coating layers of TRISO particles. Such mechanisms could include lattice diffusion, grain boundary diffusion, pore diffusion, nano-cracking, or vapor transport (van Rooyen et al., 2014). Furthermore, effects like irradiation-induced trapping and adsorption, thermal decomposition of the coating layers, or chemical attack of the coating layers by other fission products, such as palladium or rare-earth elements, could potentially impact these transport mechanisms. Because of the limited fundamental knowledge of all possible transport

Table 2.10. Mass diffusion coefficients.

		Kernel	PyC	SiC
Ag	$\mathbf{D_1}$ **(m^2/s)**	6.7×10^{-9}	5.3×10^{-9}	3.6×10^{-9}
	$\mathbf{Q_1}$ **(kJ/mol)**	165	154	215
	$\mathbf{D_2}$ **(m^2/s)**	–	–	–
	$\mathbf{Q_2}$ **(kJ/mol)**	–	–	–
Cs[a]	$\mathbf{D_1}$ **(m^2/s)**	5.6×10^{-8}	6.3×10^{-8}	$5.5 \times 10^{-14}\mathrm{e}^{(\Gamma \times 1.1/5)}$
	$\mathbf{Q_1}$ **(kJ/mol)**	209	222	125
	$\mathbf{D_2}$ **(m^2/s)**	5.2×10^{-4}	–	1.6×10^{-2}
	$\mathbf{Q_2}$ **(kJ/mol)**	362	–	514
Sr	$\mathbf{D_1}$ **(m^2/s)**	2.2×10^{-3}	2.3×10^{-6}	1.2×10^{-9}
	$\mathbf{Q_1}$ **(kJ/mol)**	488	197	205
	$\mathbf{D_2}$ **(m^2/s)**	–	–	1.8×10^{6}
	$\mathbf{Q_2}$ **(kJ/mol)**	–	–	791
Kr[b]	$\mathbf{D_1}$ **(m^2/s)**	$s(1.3 \times 10^{-12}, 8.8 \times 10^{-15}, 700)$	2.9×10^{-8}	$s(8.6 \times 10^{-10}, 3.7 \times 10^{1}, 1353)$
	$\mathbf{Q_1}$ **(kJ/mol)**	$s(126, 54, 700)$	291	$s(326, 657, 1353)$
	$\mathbf{D_2}$ **(m^2/s)**	$s(-, 6 \times 10^{-1}, 700)$	2×10^{5}	–
	$\mathbf{Q_2}$ **(kJ/mol)**	$s(-, 480, 700)$	923	–

[a] Γ is fast neutron fluence ($\times$ 10^{25} n/m^2, E >0.18 MeV).
[b] $s(a, b, c)$ gives a if temperature is less than c (°C) and b otherwise.

mechanisms, Fick's laws of diffusion are used with "effective" diffusivities to model fission product transport through TRISO particles.

The effective diffusion coefficient, D (m^2/s), is defined in Arrhenius form as:

$$D = D_1 \exp\left(\frac{-Q_1}{RT}\right) + D_2 \exp\left(\frac{-Q_2}{RT}\right) \tag{2.32}$$

where R is the universal gas constant. Values of D_1, D_2, Q_1, and Q_2 for silver, cesium, and strontium respectively, are given in Table 2.10 (Collin et al., 2015; IAE, 1997). Diffusion coefficients for the kernel are values derived from experimental data on UO_2 fuel. These values are used for the UCO kernel, due to lack of data. Although not used in this report, diffusion coefficients for krypton are included in Table 2.10 for reference.

2.3 Fission Gas

The release of long-lived fission gases from the kernel is modeled as a two-step process: first, the gas atoms are driven through the grain towards the grain boundary; second, the gas atoms migrate from the grain boundary to the free surface of the fuel where they are instantaneously released into the free volume of the TRISO particle. The model includes both direct recoil and diffusion to grain boundaries. The release

fraction FGR (-), which corresponds to the fraction of the fission gas that is released by the kernel, is given by:

$$FGR = \left(RF_{recoil} + [1.0 - RF_{recoil}]RF_{Booth}\right) FGP \tag{2.33}$$

where RF_{recoil} (-) and RF_{Booth} (-) are the release fractions of fission gas in regard to direct recoil and diffusion, respectively, and FGP (mol) is the amount of fission gas produced in the kernel. The model assumes that 100% of the fission gas is released to the void volume.

2.3.1 Direct Recoil

Direct kinetic release of fission gases from the kernel to the buffer is accounted for by geometrical considerations and fission fragment ranges derived from compiled experimental data (Littmark and Ziegler, 1980). The fission gas mixture is essentially composed of krypton and xenon, with relative fractions of 18.5% and 81.5% (Miller et al., September, 2018), respectively. Hence, the recoil fraction is given by:

$$RF_{recoil} = 0.185RF_{recoil,Kr} + 0.815RF_{recoil,Xe} \tag{2.34}$$

where $RF_{recoil,Kr}$ (-) and $RF_{recoil,Xe}$ (-) are the respective release fractions of krypton and xenon due to recoil. They depend on the ranges of krypton and xenon in UCO (i.e., r_i for i = Kr, Xe) and on the radius of the kernel, r_k (m):

$$RF_{recoil,i} = 0.25 \left(\frac{r_k^3 - [r_k - r_i]^3}{r_k^3} \right) \tag{2.35}$$

The ranges of krypton and xenon in UCO (i.e., r_i for i = Kr, Xe) are obtained from their individual ranges in uranium, carbon, and oxygen:

$$r_i = 10.0 \left(\frac{r_{i,U} + OUr_{i,O} + CUr_{i,C}}{\rho_k \left[1.0 + OU + CU\right]} \right) \tag{2.36}$$

where OU (-) and CU (-) are the initial oxygen-to-uranium and carbon-to-uranium ratios, ρ_k (g/cm^3) is the density of the kernel, and the individual ranges are given in Table 2.11.

Table 2.11. Range of Kr and Xe in U, C, and O (Littmark and Ziegler, 1980).

Fission product	krypton	krypton	krypton	xenon	xenon	xenon
Medium	uranium	carbon	oxygen	uranium	carbon	oxygen
Range (mg/cm^2)	11.7	3.3	3.1	8.3	2.3	2.2

2.3.2 Booth Model

Diffusive release through kernel grains to the grain boundaries and subsequent transport through the interconnected porosity is estimated by the Booth equivalent sphere diffusion model (Booth, 1957).

The Booth release fraction for both short-lived ($\lambda \neq 0$) and long-lived ($\lambda \equiv 0$) fission products is given by:

$$RF_{\text{Booth}}^{\text{in-pile}}(\tau) = \begin{cases} \dfrac{3}{\sqrt{\mu}}\left(\coth\left(\sqrt{\mu}\right) - \dfrac{1}{\sqrt{\mu}}\right) - \dfrac{6\mu}{e^{\mu\tau}-1}\displaystyle\sum_{n=1}^{\infty}\dfrac{1-\exp\left[-n^2\pi^2\tau\right]}{n^2\pi^2\left(n^2\pi^2+\mu\right)}, & \text{for } \lambda \neq 0 \\ 1 - \dfrac{6}{\tau}\displaystyle\sum_{n=1}^{\infty}\dfrac{1-\exp\left[-n^2\pi^2\tau\right]}{n^4\pi^4}, & \text{for } \lambda \equiv 0 \end{cases} \tag{2.37}$$

where r_{grain} (m) is the radius of the diffusing sphere (i.e., the average grain radius), D (m^2/s) is the diffusivity of the fission gas in the grain, t (s) is the time, $\tau = D't$, and $\mu = \lambda/D'$.

The release of the fission products from the fuel kernel, during accident condition/isothermal heating tests, is approximated by solving the diffusion equation without source/sink terms (Verfondern, 2012). Thus, the Booth release fraction becomes (Booth, 1957):

$$RF_{\text{Booth}}^{\text{out-of-pile}} = 1.0 - 6.0\sum_{n=1}^{\infty}\frac{\exp\left(-Dt\left[\frac{n\pi}{r_{\text{grain}}}\right]^2\right)}{n^2\pi^2}. \tag{2.38}$$

Note that the adjustment for low flux is an approximation in the code. Once the fast neutron flux is less than or equal to the preset cut-off flux (via 'cutoff_neutron_flux'), the fractional release is computed according to Equation 2.38. The release fraction computations are verified by Toptan et al. (2023) at in-pile and out-of-pile conditions for both short- and long-lived isotopes.

The unperturbed diffusion coefficient, D (m^2/s), formulated for UO_2 fuel by Turnbull et al. (1982), is given as:

$$D_{\text{eff}} = \sum_{i=1}^{3} D_i \tag{2.39}$$

where D_1, D_2, and D_3 are the diffusion coefficients of the mechanisms controlling diffusion at different temperature ranges.

1. At the highest temperatures, diffusion proceeds through the cation lattice by means of thermally activated vacancies:
$$D_1 = 7.6 \times 10^{-10}\exp\left(-\frac{35225}{T_K}\right) \tag{2.40}$$
where T_K (K) is the temperature of the kernel.
2. At intermediate temperatures, diffusion is driven by means of vacancies produced by the irradiation process:
$$D_2 = s^2 j_v \left(\frac{K'}{Z j_v}\right)^{0.5} \tag{2.41}$$
where s (m) is the atomic jump distance, j_v (s^{-1}) is the cation vacancy jump rate, K' (s^{-1}) is the rate of defect production per atom, and Z (-) is the number of sites around a point defect from which

recombination is inevitable. They are given by:

$$j_v = 10^{13} \exp\left(-\frac{27778}{T_K}\right) \tag{2.42}$$

$$K' = \frac{KB_u}{t} \tag{2.43}$$

$$s = 3.0 \times 10^{-10} \quad \text{and} \quad Z = 2 \tag{2.44}$$

where K (10^4 defects/fission) is the damage rate and B_u in %FIMA (fissions per initial metal atom) is the burnup.

3. Finally, at lower temperatures, a term proportional to the fission rate density, f''' (fission/m^3-s), is used to agree with experimental results reported by Turnbull et al. (1982):

$$D_3 = 2.0 \times 10^{-40} f''' \tag{2.45}$$

2.3.3 Fission Gas Production

The amount of fission gas produced by the kernel, FGP (mol), during a time interval, Δt (s), is calculated as:

$$FGP = \frac{\Gamma_{FG} f''' V_k \Delta t}{N_{avo}} \tag{2.46}$$

where Γ_{FG} (-) is the combined fractional fission yield of gaseous fission product atoms (assumed to be krypton and xenon) per fission, V_k (m^3) is the volume of the kernel, and N_{avo} (6.022x10^{23} at/mol) is Avogadro's number.

2.3.4 Fission Yields

Fission yields, Γ (atoms/fission), for silver, cesium, strontium, and the combination of krypton and xenon are given below.

- For silver:

$$\Gamma_{Ag} = \begin{cases} 1.31625 \times 10^{-3} b^{0.55734} & \text{for } e < 17.5 \\ 8.24492 \times 10^{-4} b^{0.53853} & \text{for } e \geq 17.5 \end{cases} \tag{2.47}$$

  with $b = \max(1.0, Bu)$.

- For cesium:

$$\Gamma_{Cs} = \begin{cases} 0.14 & \text{for } e < 17.5 \\ 0.16 & \text{for } e \geq 17.5 \end{cases} \tag{2.48}$$

- For strontium:

$$\Gamma_{Sr} = \begin{cases} 0.11754 b^{-0.21762} & \text{for } e < 17.5 \\ 0.11819 b^{-0.15778} & \text{for } e \geq 17.5 \end{cases} \tag{2.49}$$

  with $b = \max(0.6, Bu)$.

- For krypton and xenon, the elements are assumed to comprise the gaseous fission yield, Γ_{FG}, (taken from the PARFUME code):

$$\Gamma_{Kr+Xe} = \Gamma_{FG} = 0.297 \tag{2.50}$$

where B_u (%FIMA) is the burnup and e (%) is the ^{235}U enrichment.

2.4 Multi-dimensional Mesh

The purpose of this section is to provide a visual of the meshes used in the analyses. Figures 2.5-2.7 respectively show 1-, 2-, and 3-D meshes of TRISO particles and Figure 2.8 shows a mesh of the pebble. This is useful for understanding where the material models are applied, the symmetry of the models, and an example of the mesh denstiy used in calculations.

Figure 2.5. 1-D TRISO particle.

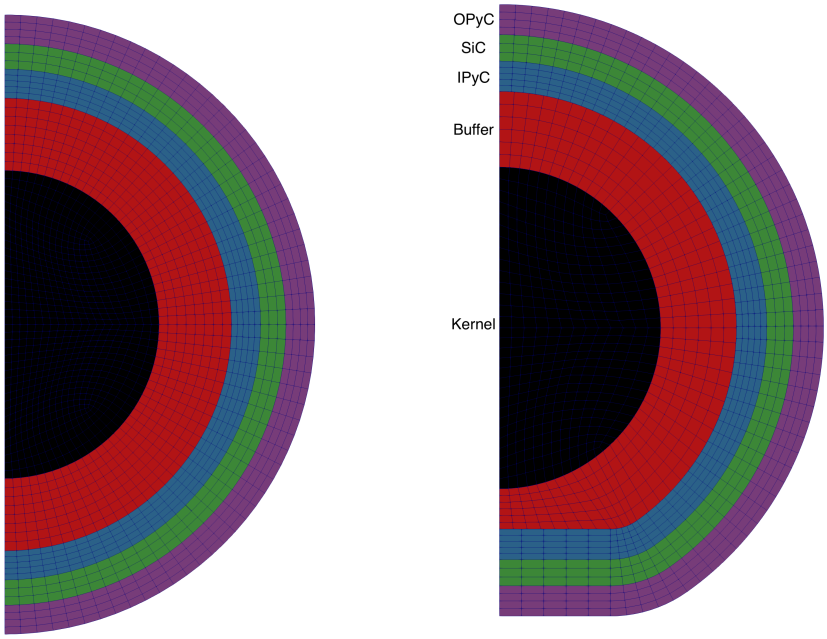

(a) Spherical (b) Aspherical

Figure 2.6. 2-D TRISO particle

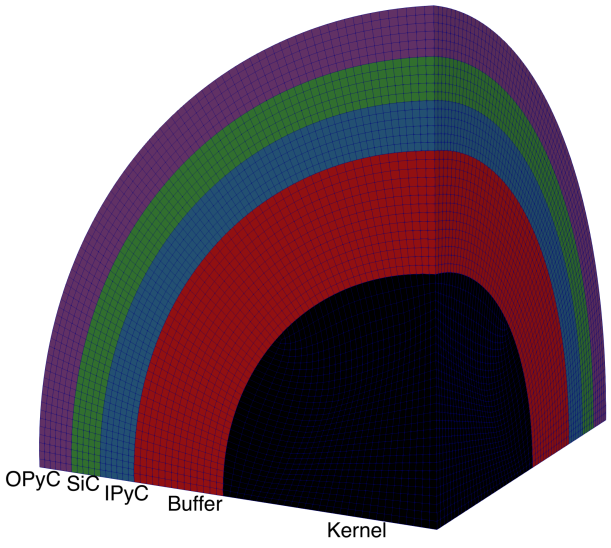

Figure 2.7. 3-D particle.

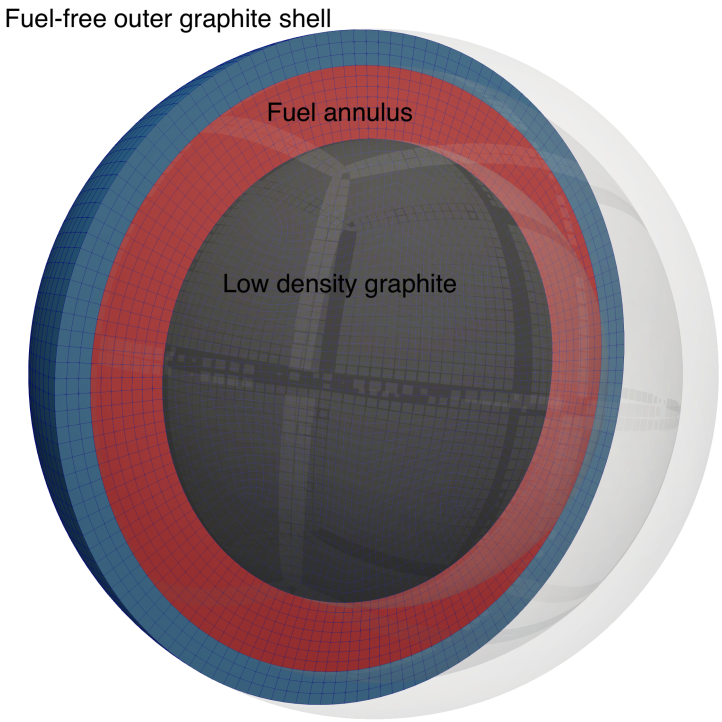

Figure 2.8. Generic pebble mesh.

3. Failure Probability

The ability of the pebble to contain fission products is largely dictated by the quality of the manufacturing process because a significant amount of fission product release is expected to occur due to coating layer failure in a small number of particles at the locations of defects. Note that at high temperature, substantial fission product release can be attributed to dispersed uranium in the matrix in addition to a small amount via diffusion through intact particles. To account for statistical variation in physical dimensions and material properties from particle to particle, a Monte Carlo scheme is utilized to compute failure probability for a statistically sampled batch of particles. This enables realistic calculations of fission product release from the many particles in a TRISO-fueled reactor.

3.1 Failure Modes

Several potential failure mechanisms for TRISO fuel, outlined in the sections below, are considered in the current work. Other failure modes in addition to those discussed here are both possible and potentially important, and techniques to consider them are in active development.

3.1.1 Pressure Vessel Failure

Early on during irradiation, PyC layers shrink, compressing the SiC layer. As irradiation progresses, the creep of the PyC layers tends to relax some of this compressive stress. In addition, the buildup of fission gas pressure tends to put all the coating layers in tension. Figure 3.1 shows the evolution of tangential stress with burnup at the inner surface of the SiC layer under three temperature conditions. This stress value is important, as it is used to determine whether a particle fails. Since carbon monoxide (CO) production in a UCO kernel is relatively small, gas pressure is usually not high enough to make the tangential stress in the SiC layer become tensile. Therefore, pressure vessel failure is not likely to occur for UCO TRISO particles at low and intermediate temperatures.

3.1.2 Cracking of the IPyC

During irradiation, shrinkage of the PyC layers causes significant tensile stress in those layers. If the stress exceeds the tensile strength of the material, a radial crack can form in a PyC layer. Such a crack leads to

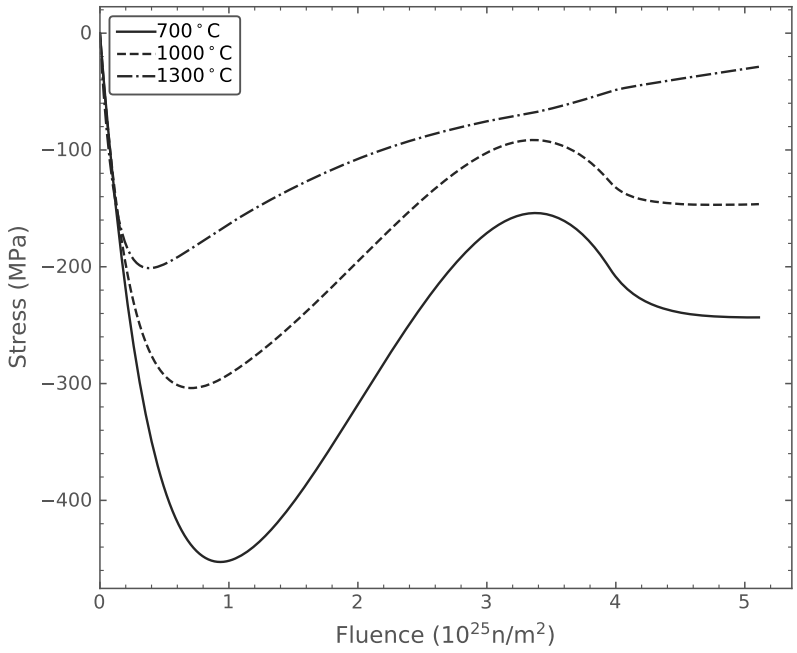

Figure 3.1. Evolution of tangential stress with burnup at the inner surface of the SiC layer.

high local tensile stress in the SiC layer adjacent to that cracked PyC layer, potentially causing failure of the SiC layer and, therefore, of the particle. In Figure 3.2a, a discrete crack in the IPyC layer is represented in the finite element model using the extended finite element method (Jiang et al., 2020). As shown in Figure 3.2b, the stress in the SiC layer near the crack tip is elevated significantly due to the development of cracking in the IPyC layer.

3.1.3 Pressure Vessel Failure of an Aspherical Particle

A single flat facet on one side of the particle created during fabrication is a common cause of aspherical behavior in particle fuel. The degree of asphericity for a particle is measured by the aspect ratio. During irradiation, the faceted portion of the particle acts as a flat plate that retains the internal gas pressure. If the pressure builds up high enough, this results in a local region with elevated tensile stress in the central portion of the plate, potentially contributing to particle failure. In the scenario shown in Figure 3.3b, the tangential stresses in the SiC layer remain compressive through the end of irradiation because the CO production is limited in UCO fuel.

3.1.4 Palladium Penetration

The fission product palladium is known to attack SiC at localized reaction sites. Based on the international historical database, the penetration rate of palladium into SiC, $\dot{P_{\mathrm{Pd}}}$ (μm/day), has been found to have an

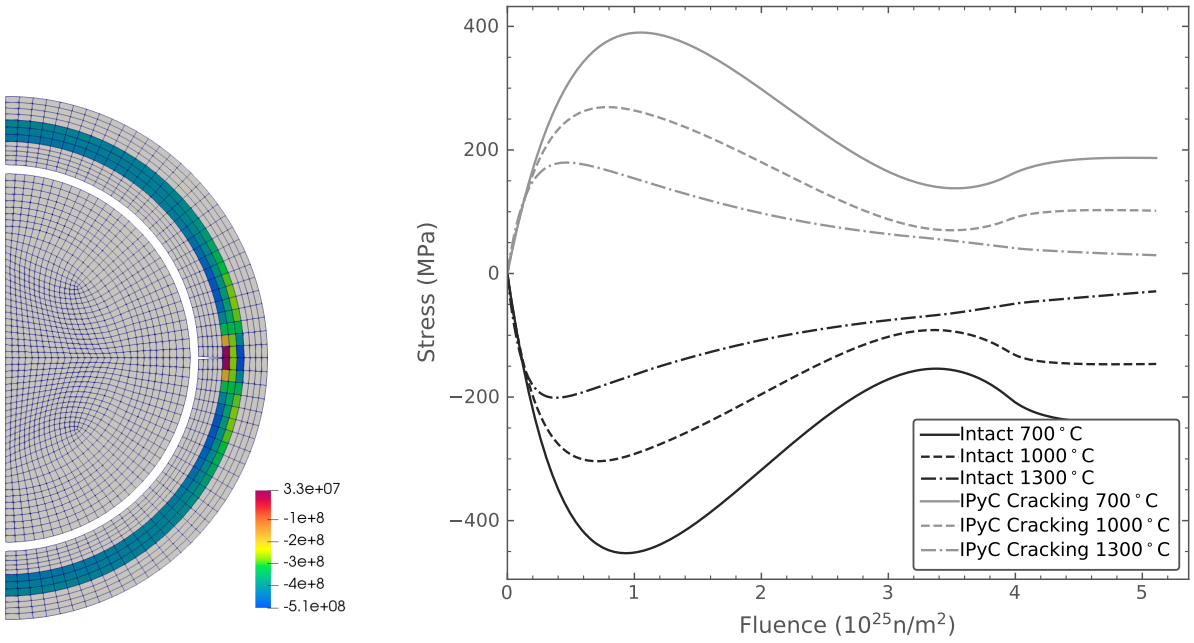

(a) (b)

Figure 3.2. 2-D axisymmetric model of postulated cracking of the IPyC layer, and time-dependent results for that model. (a) Stress contour (Pa) for T = 700°C when maximum tangential stress is reached. For clarity, only stresses in the SiC layer are shown. (b) Time history of peak inner-wall tangential stress in the SiC layer.

Arrhenius temperature dependence given by Miller et al. (September, 2018):

$$\dot{P_{\mathrm{Pd}}} = 38.232 \times \exp\left(-\frac{11342.3}{T}\right) \tag{3.1}$$

where T(K) is the temperature of the SiC. The SiC layer is conservatively considered failed when the penetration reaches 50% of its thickness.

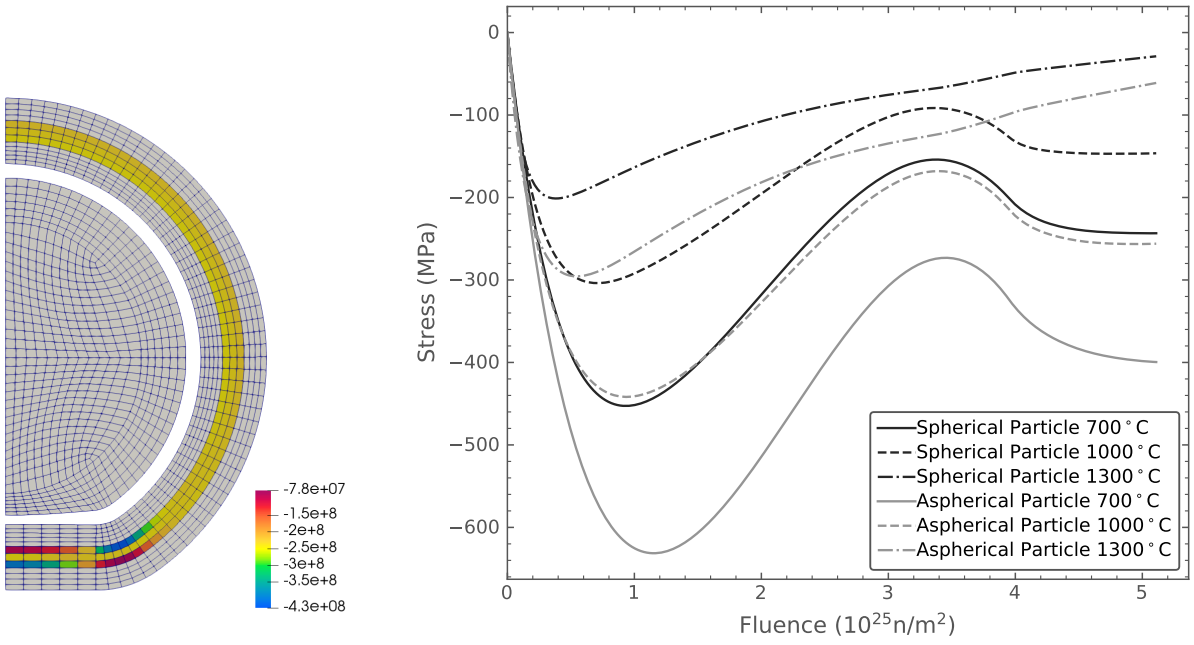

(a) (b)

Figure 3.3. 2-D axisymmetric model of an aspherical particle, and time-dependent results for that model. (a) Stress contour (Pa) for T = 700°C at end of irradiation, with an aspect ratio of 1.04. For clarity, only stresses in the SiC layer are shown. (b) Time history of stress in the faceted portion of the SiC layer. Stresses in comparable locations for a spherical particle are shown for comparison.

3.2 Weibull Failure Theory

A Weibull failure criterion is used to determine vessel failure for the IPyC layer and SiC layer. The maximum stress, σ_c, is compared to a strength sampled from a Weibull distribution having mean strength σ_{ms} and Weibull modulus m. Failure occurs when σ_c exceeds the sampled strength. The cumulative distribution function for the Weibull distribution is given as:

$$P = 1 - \exp\left(-\left(\frac{\sigma_c}{\sigma_{ms}}\right)^m\right) \tag{3.2}$$

The effective mean strength σ_{ms} is given as:

$$\sigma_{ms} = \frac{\sigma_0}{I_n^{\frac{1}{m}}} \tag{3.3}$$

where σ_0 is the characteristic strength. The integral, I_n, is a normalized integration of the stress distribution

using the principle of independent action (PIA) model as follows:

$$I_n = \frac{\int_V (\sigma_1^m + \sigma_2^m + \sigma_3^m) dV}{\sigma_c^m} \tag{3.4}$$

where σ_c is the maximum value calculated for a principal stress anywhere in the volume and σ_1, σ_2, and σ_3 are three principal stresses. Negative principal stresses are not included in this integral because the compressive stresses do not contribute to fracture.

The Weibull modulus (m) and characteristic strength (σ_0) for the SiC are held constant throughout irradiation and are given as:

$$m = 6 \text{ and } \sigma_0 = 9.64 \times 10^6 \text{ Pa-m}^{3/6} \tag{3.5}$$

The Weibull modulus for the PyC is assumed to be 9.5, which corresponds to a density of 1.9 g/cm^3.

The Weibull characteristic strength of the PyC (Miller et al., September, 2018; Ho, July, 1993) is a function of anisotropy and determined from the following equation for room temperature:

$$\sigma_0 = 10^6 \times (154.46X^2 - 141.1X) \tag{3.6}$$

where X is a fitting parameter with a default value of 1.02. The characteristic strength has units of Pa-m$^{3/9.5}$ when the Weibull modulus is 9.5.

To account for other temperatures and non-zero fluence, Equation 3.6 is multiplied by a factor as follows:

$$\text{factor} = [(1 + 0.23\phi)(1 + 0.00015T)]^{1/2} \tag{3.7}$$

where ϕ (10^{25} n/m^2, E >0.18 MeV) is the fast neutron fluence and T (°C) is the temperature.

3.3 High-fidelity Analysis of Stress Concentrations

For computational efficiency, it is important that each Monte Carlo sample is evaluated using a 1-D model. However, stress concentrations due to the presence of phenomena such as cracking must be characterized using a higher-dimensional model. To account for these multi-dimensional phenomena within a 1-D TRISO model, a high-dimensional failure simulation is performed to obtain the mean effective strength and stress correlation function, based on a multi-dimensional stress distribution. Those values are used in the 1-D model to make adjustments to the stress in failure determination.

3.3.1 Stress Correlation for IPyC Cracking

The maximum tangential stress histories in the SiC layer for both a cracked particle (near the crack tip) and an intact particle are shown in Figure 3.4. The maximum SiC stress in a cracked particle is approximated as:

$$\sigma_{\text{IPyC-cracking}} = \frac{\bar{\sigma}_{\text{2D}}}{\bar{\sigma}_{\text{1D}}} \sigma_{\text{1D}} \tag{3.8}$$

where $\bar{\sigma}_{2D}$ and $\bar{\sigma}_{1D}$ are the maximum stress calculated in the 2-D and 1-D analyses at the mean values of the fuel properties (e.g. diameter, thickness, density, etc.) for a specified batch of particles, respectively. Upon varying statistical parameters, the maximum stress in the SiC layer is determined from the 1-D finite element solution for σ_{1D}. The mean strength of the 2-D model, as evaluated at the maximum tangential stress state, will be used for 1-D analysis.

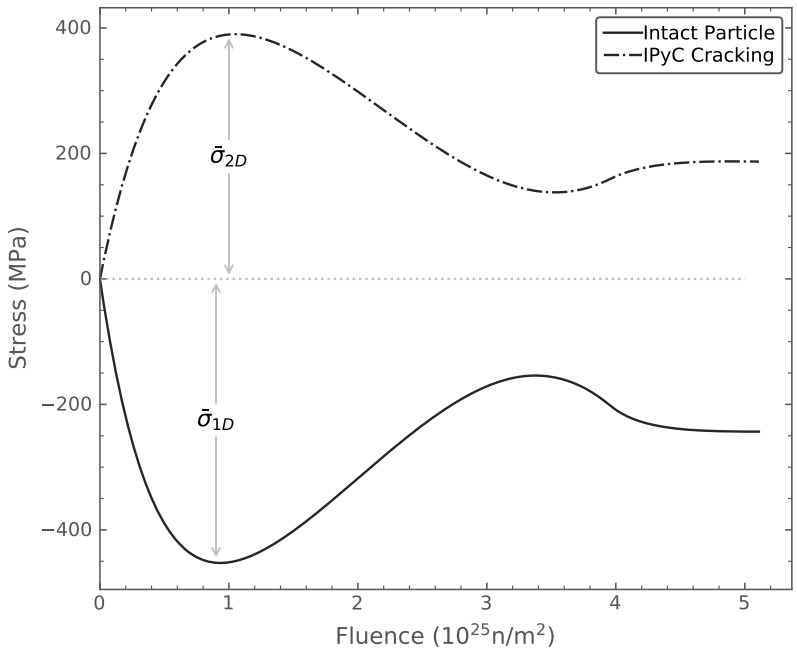

Figure 3.4. Time histories of maximum tangential stress in the SiC layer for a 2-D model of a particle with a cracked IPyC layer, compared with a 1-D model of an intact particle. These are used to develop the stress correlation for IPyC cracking.

3.3.2 Stress Correlation for an Aspherical Particle

The tangential stress histories for representative faceted and spherical fuel particles are shown in Figure 3.5. In evaluating the effect of asphericity, a second term is added to correctly estimate the maximum stress, σ_c, for an aspherical particle:

$$\sigma_{\text{aspherical-particle}} = \frac{\bar{\sigma}_{2D}}{\bar{\sigma}_{1D}}\sigma_{1D\text{-min}} + \frac{\Delta\bar{\sigma}_{2D}}{\Delta\bar{\sigma}_{1D}}\Delta\sigma_{1D} \tag{3.9}$$

where $\Delta\bar{\sigma}_{2D}$, $\Delta\bar{\sigma}_{1D}$, and $\Delta\sigma_{1D\text{-min}}$ are changes in the stresses $\bar{\sigma}_{2D}$, $\bar{\sigma}_{1D}$, and $\sigma_{1D\text{-min}}$, going from the minimum to the end of irradiation. If a second extremum (or maximum) occurs before the end of irradiation, $\Delta\bar{\sigma}_{2D}$, $\Delta\bar{\sigma}_{1D}$, and $\Delta\sigma_{1D}$ are taken as changes in these stresses, going from minimum to maximum. The additional term is needed because pressure vessel failure of aspherical particles typically occurs after the minimum stress is reached, when shrinkage effects from the PyC are decreasing and the inner pressure keeps accumulating.

The mean effective strength of the 2-D model evaluated at the end of irradiation will be used in 1-D analysis.

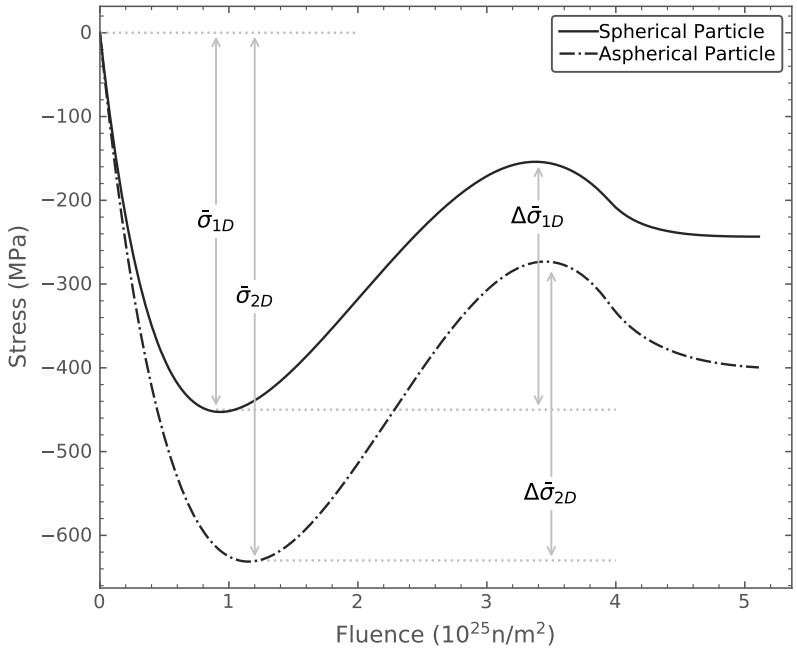

Figure 3.5. Time histories of the maximum tangential stress in the SiC layer for a 2-D model of an aspherical particle with an aspect ratio of 1.04, compared to a 1-D model of a spherical particle. These are used to develop the stress correlation for an aspherical particle.

3.3.3 Higher Order Stress Correlation Functions

BISON can consider a statistical variation of the IPyC, SiC and OPyC layer thickness because they strongly affect particle failure. To obtain each $h(\Delta v)$ function, we typically sample seven points where $\Delta v = -3s, -2s, -s, 0, s, 1s, 2s$ and $3s$, and s is the standard deviation. At the midpoint, $h(\Delta v)$ has a value of 1 because $\Delta v = 0$. At other data points, we perform both multi-dimension and one-dimension analysis to determine the value of $h(\Delta v)$ function. A polynomial curve fit is finally performed on the data points to generate the quadratic $h(\Delta v)$ function.

The maximum SiC stress in a cracked particle is approximated as:

$$\sigma_{\text{IPyC-cracking}} = \frac{\bar{\sigma}_{2\text{D}}}{\bar{\sigma}_{1\text{D}}} \sigma_{1\text{D}}(v_{\text{IPyC}}, v_{\text{SiC}}, v_{\text{OPyC}}) h_{\text{IPyC}}(\Delta v_{\text{IPyC}}) h_{\text{SiC}}(\Delta v_{\text{SiC}}) h_{\text{OPyC}}(\Delta v_{\text{OPyC}}). \tag{3.10}$$

where $\bar{\sigma}_{2\text{D}}$ and $\bar{\sigma}_{1\text{D}}$ are the maximum stress calculated in the 2-D and 1-D analyses at the mean values for a specified batch of particles, respectively. Representative plots of the h functions for IPyC cracking are shown in Figure 3.6.

The maximum SiC stress in an aspherical particle is approximated as:

$$\begin{aligned}\sigma_{\text{aspherical-particle}} = &\frac{\bar{\sigma}_{\text{2D}}}{\bar{\sigma}_{\text{1D}}}\sigma_{\text{1D-min}}(v_{\text{IPyC}}, v_{\text{SiC}}, v_{\text{OPyC}})h_{\text{IPyC}}(\Delta v_{\text{IPyC}})h_{\text{SiC}}(\Delta v_{\text{SiC}})h_{\text{OPyC}}(\Delta v_{\text{OPyC}}) \\ &+ \frac{\Delta\bar{\sigma}_{\text{2D}}}{\Delta\bar{\sigma}_{\text{1D}}}\Delta\sigma_{\text{1D}}(v_{\text{IPyC}}, v_{\text{SiC}}, v_{\text{OPyC}})h_{\text{IPyC-}\Delta}(\Delta v_{\text{IPyC}})h_{\text{SiC-}\Delta}(\Delta v_{\text{SiC}})h_{\text{OPyC-}\Delta}(\Delta v_{\text{OPyC}})\end{aligned} \tag{3.11}$$

where $\Delta\bar{\sigma}_{\text{2D}}$, $\Delta\bar{\sigma}_{\text{1D}}$, and $\Delta\sigma_{\text{1D-min}}$ are changes in the stresses $\bar{\sigma}_{\text{2D}}$, $\bar{\sigma}_{\text{1D}}$, and $\sigma_{\text{1D-min}}$, going from the minimum to the end of irradiation. Representative plots of the h functions for an aspherical particle are shown in Figure 3.6.

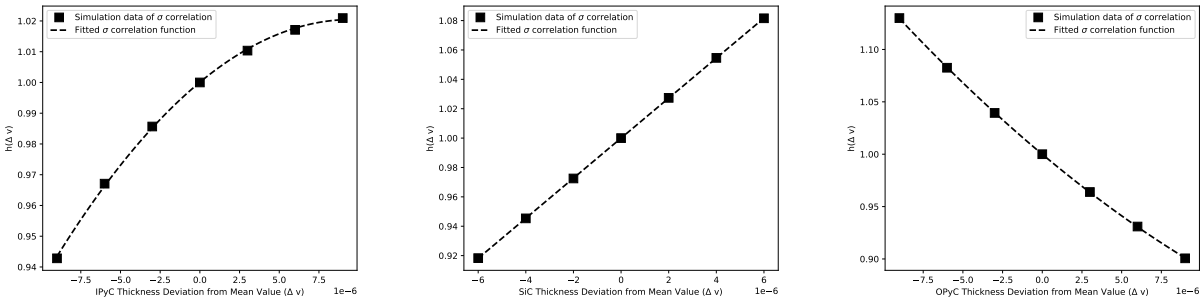

(a) (b) (c)

Figure 3.6. Higher order stress correlation functions for IPyC cracking. (a) Stress correlation function of IPyC layer thickness for IPyC cracking. (b) Stress correlation function of SiC layer thickness for IPyC cracking. (c) Stress correlation function of OPyC layer thickness for IPyC cracking.

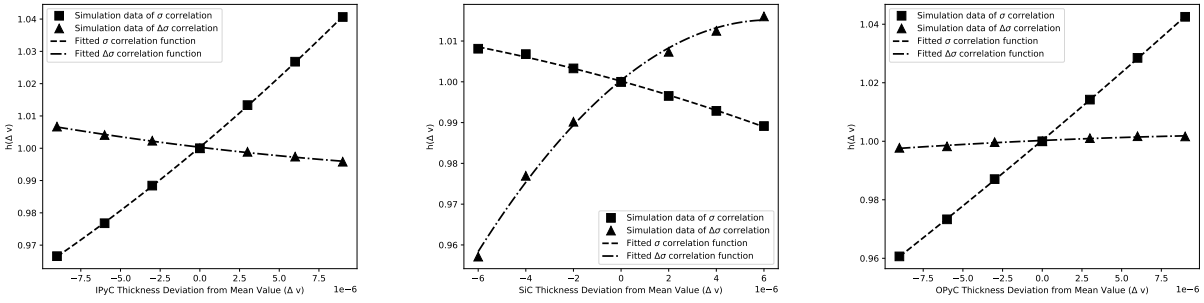

(a) (b) (c)

Figure 3.7. Higher order stress correlation functions for an aspherical particle. (a) Stress correlation function of IPyC layer thickness for an aspherical particle.(b) Stress correlation function of SiC layer thickness for an aspherical particle.(c) Stress correlation function of OPyC layer thickness for an aspherical particle.

3.4 Monte Carlo Scheme

3.4.1 Methodology

Figure 3.8 depicts the methodology used to calculate the failure probability of a population of TRISO particles. This methodology relies on a Monte Carlo scheme in which each particle analyzed is a realization of a set of statistically sampled parameters from the distributions of as-fabricated fuel characteristics (dimensions, densities, etc.) that can be found among the particles in a fuel element. For each sample, BISON runs a 1-D model of a TRISO particle over the irradiation history. For particles with localized flaws (i.e., aspherical particles and particles with cracked IPyC), an adjustment of the maximum stress and effective mean strength will be made, as described in Section 3.3.

At each time step, the following failure mechanisms are checked:

- Pressure vessel failure of a spherical or aspherical particle: Failure occurs when the maximum tangential tensile stress of the SiC layer due to internal gas pressure is greater than the strength of the SiC.
- SiC failure due to IPyC cracking: Cracking of the IPyC occurs when the maximum tangential tensile stress in the IPyC layer is greater than its strength. A cracked IPyC changes stress from compression to tensile in the SiC layer. SiC failure occurs when the maximum tangential tensile stress of the SiC layer due to IPyC cracking is greater than its strength.
- Palladium penetration: Failure is assumed when Palladium penetration exceeds half the thickness of the SiC layer. In this case, the SiC layer loses its structural integrity and leak-tightness to fission products and is assigned a non-retentive diffusivity.

3.4.2 Effective Diffusion Coefficients for Failed Particles

The methodology laid out in Figure 3.8 can also be used to simulate fission product diffusion for a collection of fuel particles. The fission product diffusion calculations combine the release fractions (release normalized to calculated inventory) of all TRISO particles in the Monte Carlo sample. Release is calculated via Fickian diffusion, while inventory is obtained from fission rate density and fission yields. In PARFUME, coating layers determined to be failed are assigned a large diffusivity (e.g., 10^{-6} m^2/s) to model the loss of retention power of that layer. In this task, a high-dimensional BISON model will be used to quantitatively determine the diffusivity for particles containing cracks in the SiC layer. As shown in Figure 3.9, a damage zone with finite width is represented in a 2-D axisymmetric model. It is hypothesized that the fission product will diffuse quickly through the damage zone, so a higher diffusivity of 10^{-6} m^2/s is assigned to the damage zone. Fission release fractions for silver, cesium, and strontium were computed by the 2-D local damage zone model under representative irradiation conditions at 700°C, 1000°C, and 1300°C. The same irradiation conditions were applied to the TRISO 1D model with different diffusion coefficients (e.g., 10^{-6}, 10^{-12}, 10^{-14}, 10^{-16}, 10^{-18} and 10^{-20} m^2/s). As shown in Figure 3.10, Figure 3.11, and Figure 3.12, the diffusion coefficient of

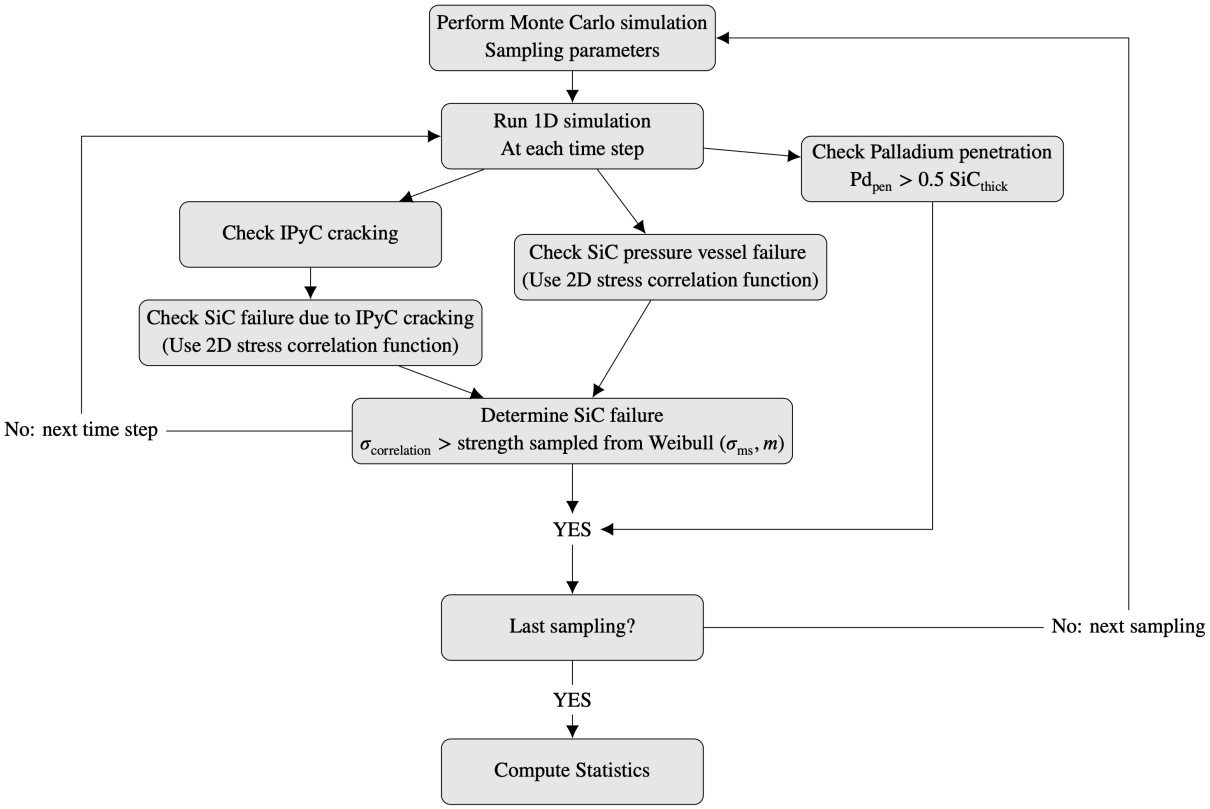

Figure 3.8. Monte Carlo scheme employed by BISON for calculating the failure probability of TRISO particles.

10^{-6} m^2/s used by PARFUME overestimates the release fractions while the diffusion coefficient of 10^{-16} m^2/s seems to give the best agreement with the 2-D result.

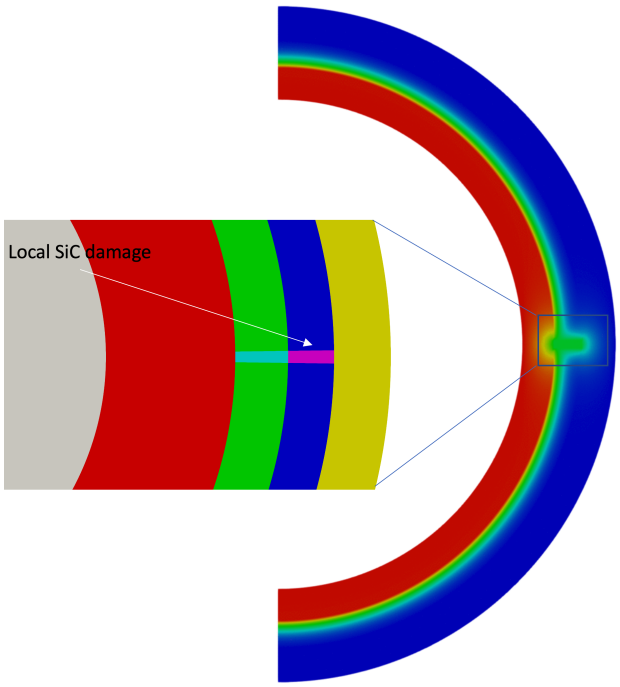

Figure 3.9. BISON 2-D axisymmetric model with local SiC damage zone.

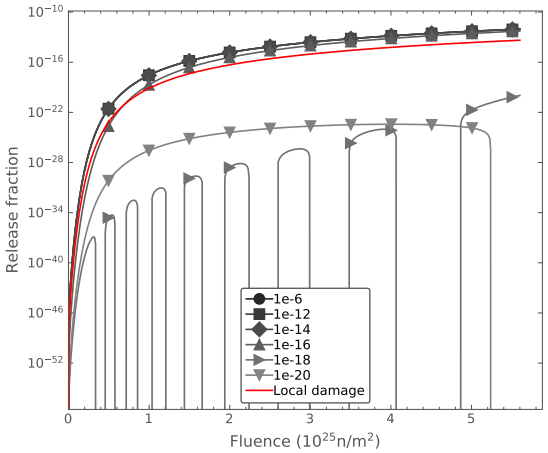

(a) Silver.

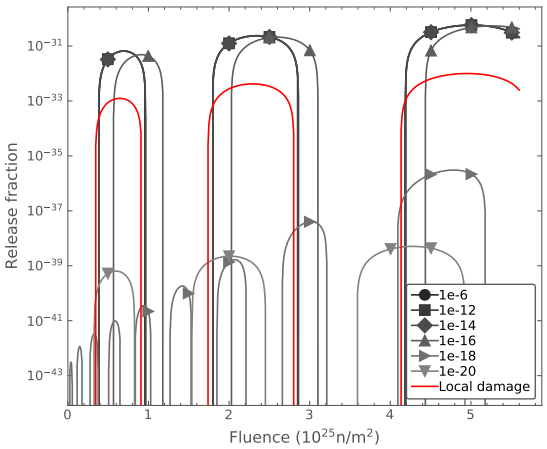

(b) Cesium.

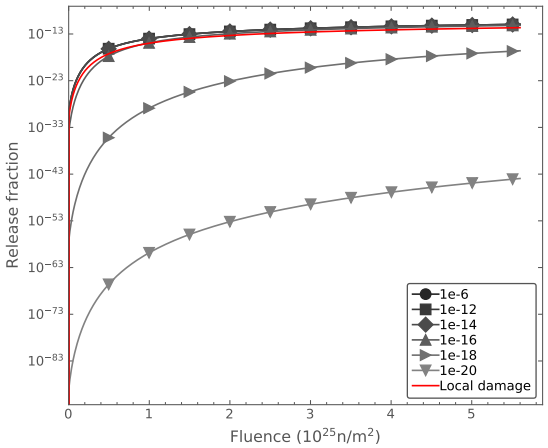

(c) Strontium.

Figure 3.10. Fission product release fractions at 700°C. The local damage 2-D model is shown in red. Different effective diffusion coefficients are simulated with the 1-D model.

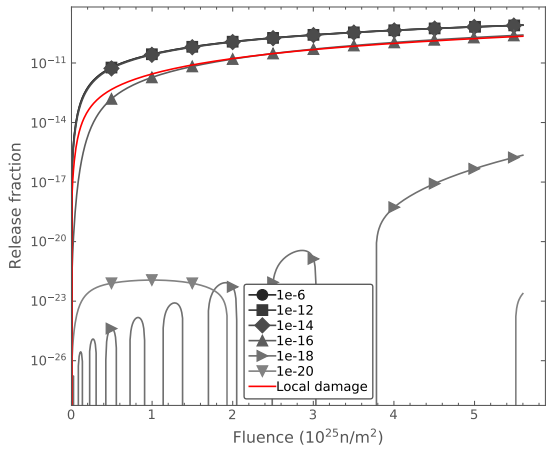

(a) Silver.

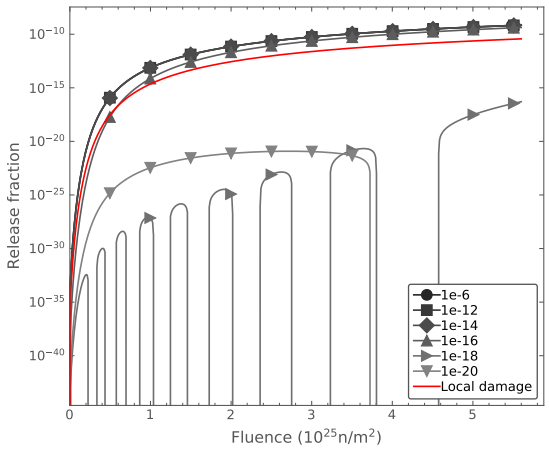

(b) Cesium.

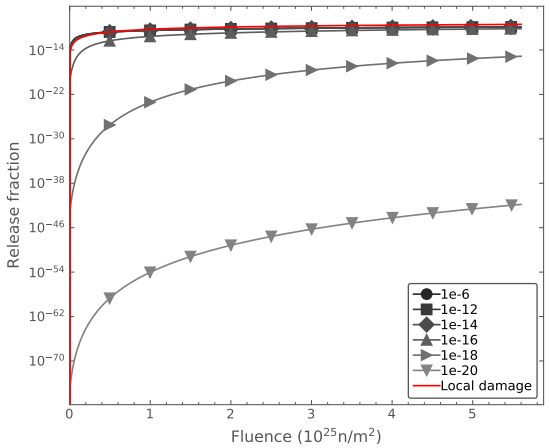

(c) Strontium.

Figure 3.11. Fission product release fractions at 1000°C. The local damage 2-D model is shown in red. Different effective diffusion coefficients are simulated with the 1-D model.

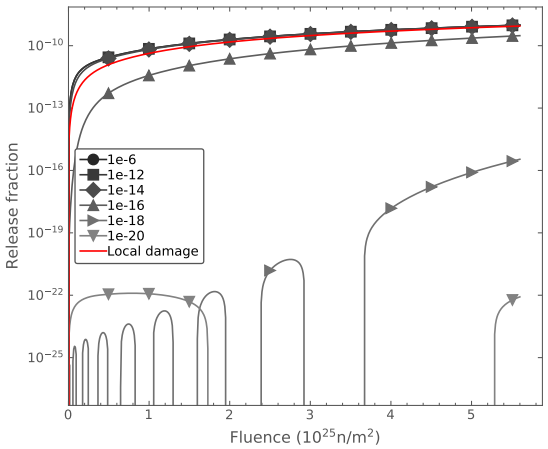

(a) Silver.

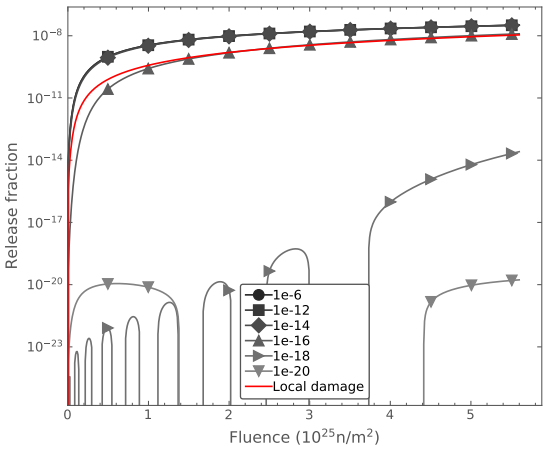

(b) Cesium.

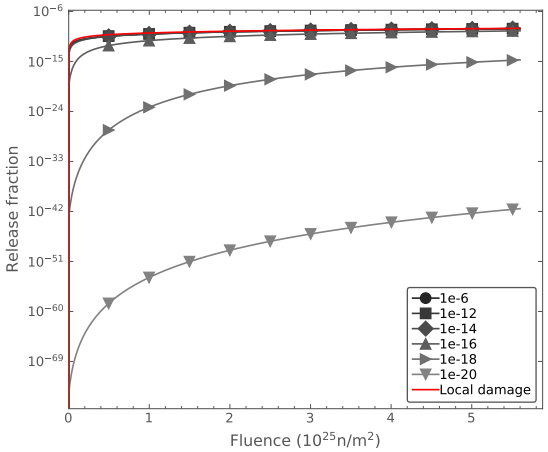

(c) Strontium.

Figure 3.12. Fission product release fractions at 1300°C. The local damage 2-D model is shown in red. Different effective diffusion coefficients are simulated with the 1-D model.

3.5 Monte Carlo vs. Direct Integration

While Monte Carlo can use 2D simulations, spherical 1D simulations are used to decrease the computational burden although this does cause multidimensional effects to be lost. To account to for the lost effects, multiple, problem dependent simulations must be run to create 2D stress functions that are then applied to the Monte Carlo simulations. Direct integration does not require the 2D stress functions as the simulations that feed the failure probability calculations are already multidimension, thus eliminating the need for hours of pre-processing. The simulations can also be run on a small number of processors instead of the 500-1000 processors needed for timely results of a Monte Carlo simulation.

The direct integration approach in BISON uses a sparse grid integration scheme to directly integrate Weibull failure probability function associated with statistically varying parameters. For more details on the direct integration approach, refer to Jiang et al. (2022). The initial development of direct integration as a method of predicting TRISO failure probability was funded by NEAMS. This new method showed the promise of enhanced failure prediction and a greatly reduced computational cost, both are of interest to Kairos Power.

It was proposed to add the option for a truncated normal distribution to the MOOSE sampler to match what is available for the Monte Carlo sampler. During initial comparisons of Monte Carlo failure probability results to that of the direct integration, it was noted that direct integration was predicting more failures for the same cases. Efforts were then redirected to an investigation into more results and the possible causes of the differences. The AGR1 capsules C122, C323, and C511 were chosen for comparisons. The normal sampler type was selected for both methods of simulation for this study. Results are presented as failure fractions and can be seen in the table below.

Table 3.1. Failure Calculations: Monte Carlo vs. Direct Integration 2D

	Monte Carlo			Direct Integration 2D		
Compact	IPyC cracking	SiC failure due to IPyC	SiC failure	IPyC cracking	SiC failure due to IPyC	SiC failure
C-1-2-2	0.1899	0.00411	0	1	0.02180722	0
C-3-2-3	0.2495	0.004811	0	1	0.02035335	0
C-5-1-1	0.3211	0.011941	0	1	0.03884009	0

This comparison shows the direct integration method to overpredict the TRISO failure fraction by almost an order of magnitude. The Monte Carlo simulations for C122, for example, predict IPyC cracking of 19% and a SiC failure due to the IPyC cracking of 0.411% of the TRISO particles. The direct integration predictions for the same compact show 100% IPyC cracking and 2.2% SiC failure, which is a vast difference.

This difference in the IPyC cracking result was attributed to the different manner that the IPyC cracking is calculated in the respective methods. For the Monte Carlo method, a 1D spherical model is used with 2D stress functions that attempt to correct the stress calculations for multidimensional effects. The direct integration method calculates the stresses directly from an aspherical model, a TRISO with a flattened side,

and then uses the stress to calculate the failure probability. To investigate this model difference as the cause of the TRISO failure difference, another simulation method of direct integration was used.

In the initial direct integration study two models, one with a cracked IPyC and an aspherical TRISO, were used to calculate the TRISO failure probabilities. This method is commonly referred to as DI-2D. As shown above, DI-2D over predicts the IPyC cracking versus the Monte Carlo method. The direct integration calculation can also be run using a 1D spherical model along with the two 2D models previously mentioned, this method is commonly referred to as DI-1D2D. In DI-1D2D the 1D spherical model is used for the IPyC cracking calculations, the 2D cracked IPyC model calculates the SiC failure due to IPyC cracking and the 2D aspherical model calculates the TRISO failure due to overpressure. Results from the DI-1D2D calculations are more in-line with the Monte Carlo calculations and can be seen in the table below. It is also interesting to note that DI-1D2D calculates a non-zero, although very small, overpressure probability that weas not seen in the other methods.

Table 3.2. Direct Integration 1D2D

Compact	IPyC cracking	SiC failure due to IPyC	SiC failure
C-1-2-2	0.19003962	0.00438798	3.98E-05
C-3-2-3	0.249657256	0.005350735	3.15E-05
C-5-1-1	0.3212427	0.0131355	1.28E-04

Comparisons of the failure probability predictions to experiment data from the AGR-1 Post Irradiation Examination report can be seen in the table below. They show that while all methods are overpredicting TRISO failures for these compacts, the Monte Carlo and the direct integration 1D2D results agree while the direct integration 2D results are an average of four times higher. Comparison of failure predictions will be continued beyond the three compacts presented here as the validation progresses. Future work plans include adding linear fracture mechanics capabilities, which should result in more accurate failure calculations.

Table 3.3. Failure Calculations: Monte Carlo vs. Direct Integration 2D vs. Direct Integration 1D2D

	Monte Carlo		Direct Integration 2D		Direct Integration 1D2D		
Compact	SiC failure due to IPyC	# of failed TRISO	SiC fail due to IPyC	# of failed TRISO	SiC failure due to IPyC	# of failed TRISO	# PIE Failures
C-1-2-2	0.00411	17	0.02180722	90	0.00438798	18	0
C-3-2-3	0.004811	20	0.02035335	85	0.005350735	22	11
C-5-1-1	0.0011941	49	0.03884009	161	0.0131355	54	3

4. Homogenization

For multiple applications in nuclear energy, the ability to accurately represent material behavior with a simplified model is important to facilitate practical engineering-scale simulations. In this work, we focus on the homogenized thermal response of a medium containing spherical inclusions, similar to a fuel form (compact or pebble) containing TRISO particles. In Section 4.1, a review on effective thermal conductivity (ETC) modeling is performed considering a random distribution of mono-sized spherical inclusions in a continuous matrix, with a primary focus on the analytical models. In Section 4.2, finite element simulations are performed to evaluate each analytical model in varying material conditions. The model predictions are compared with the expected results obtained from the finite element predictions in addition to the Wiener and Hashin–Shtrikman bounds. Section 4.3 covers a practical discussion of how these analytical homogenization models are applied and used in nuclear applications, with a primary focus on TRISO fuel pebble homogenization. *The material presented here is a subset of the information found in Toptan et al. (2021).* Lastly, Section 4.4 covers a discussion on the analytical homogenization methods to obtain the ETC as used to obtain the effective diffusivity coefficient (EDC) by considering heat conduction to be analogous with simplified Fickian diffusion (or fission product species conservation or mass diffusion). *The material presented here is a subset of the information found in Toptan et al. (2022a).*

4.1 Analytical ETC Models

In this study, we focus on analytical methods to obtain the ETC. We provide a selection of widely used theoretical and semi-theoretical models to predict the ETC of binary media in which the spherical inclusions are embedded in a continuous matrix. We also cover the analytical models used to obtain the upper and lower bounds of ETC. The mathematical formulations of the models are tabulated in Table 4.3. Based on the selected application, different notations can be applied, such as $\upsilon_2 = p$ for the thermal conductivity correction with the porosity, p, or $\upsilon_2 = PF$ for the packing fraction, PF, of the TRISO particles within the matrix (Miller et al., September, 2018; Gontard and Nabielek, July, 1990; Hales et al., 2020; Folsom et al., 2015; Jiang et al., 2021; Hales et al., 2021). More discussions on the homogenization in the TRISO applications are available in Section 4.3.

The conduction of heat through a stationary random distribution of spheres is the current focus. However, the governing equations of elasticity, thermal conduction, and electrical conduction problems in the steady

Table 4.1. A brief summary of the analytical models surveyed in Toptan et al. (2021). The nomenclature: k_e is the ETC, k_1 and v_1 are the thermal conductivity and volume fraction of continuous phase, k_2 and v_2 are the thermal conductivity and volume fraction of dispersed phase, and $\alpha = k_2/k_1$ is the ratio of the thermal conductivities of dispersed phase to continuous phase.

Model	**Mathematical Expression**	**Model**	**Mathematical Expression**
Series (or harmonic mean)	$\frac{k_e}{k_1} = \frac{1}{1 + v_2\left(\frac{1}{\alpha} - 1\right)}$	Parallel (or volume averaged)	$\frac{k_e}{k_1} = 1 + v_2\,(\alpha - 1)$
Maxwell	$\frac{k_e}{k_1} = 1 + \frac{3v_2}{\left(\frac{\alpha+2}{\alpha-1}\right) - v_2}$	Rayleigh	$\frac{k_e}{k_1} = 1 + \frac{3v_2}{\left(\frac{\alpha+2}{\alpha-1}\right) - v_2 - 1.65\left(\frac{\alpha-1}{\alpha+4/3}\right)v_2^{10/3}} + \dots$
Ratcliffe	$k_e = k_1^{v_1} k_2^{v_2}$	Kämpf	$\frac{k_e}{k_1} = 1 - a v_2^{2/3}\left(1 - \frac{1}{1 + \frac{1}{a} v_2^{1/3}\left[\frac{1}{\alpha} - 1\right]}\right)$
EMT (Bruggeman)	$\frac{k_e}{k_1} = \alpha A + \sqrt{\alpha^2 A^2 + \frac{\alpha}{2}}$ $A = \frac{1}{4}\left(3v_2 - 1 + \frac{1}{\alpha}\left[2 - 3v_2\right]\right)$	Hamilton–Crosser	$\frac{k_e}{k_1} = \frac{\alpha + (n-1) - (n-1)(1-\alpha)v_2}{\alpha + (n-1) + (1-\alpha)v_2}$ for $n = 3$ (spheres)
Lewis–Nielsen	$k_e = \frac{1 + A\left(\frac{\alpha-1}{\alpha+A}\right)v_2}{1 - \left[1 + \left(\frac{1 - v_{2,max}}{v_{2,max}^2}\right)\right]\left(\frac{\alpha-1}{\alpha+A}\right)v_2^2}$ see Table 4.2	Levy	$\frac{k_e}{k_1} = \frac{2k_1 + k_2 - 2(k_1 - k_2)F}{2k_1 + k_2 + (k_1 - k_2)F}$ with $F = \frac{1}{2}\left(\frac{2}{G} - 1 + 2v_2 - \sqrt{\left(\frac{2}{G} - 1 + 2v_2\right)^2 - \frac{8v_2}{G}}\right)$ $G = \frac{(k_1 - k_2)^2}{(k_1 + k_2)^2 + k_1 k_2/2}$
Chiew–Glandt	$\frac{k_e}{k_1} = \frac{\left(1 + 2\beta v_2 + v_2^2\beta\left[2\beta^2 - 0.1\right] + 0.05 v_2^3 \exp\left(4.5\beta\right)\right)}{1 - \beta v_2}$	Davis	$\frac{k_e}{k_1} = 1 + \frac{3(\alpha-1)}{\alpha + 2 - (\alpha-1)v_2}\left[v_2 + f(\alpha)v_2^2 + O(v_2^3)\right]$ $f(\alpha) = \sum_{p=6}^{\infty} \frac{(B_p - 3A_p)}{(p-3)2^{p-3}}$ in terms of A_p and B_p, which are known functions of α.
D-EMT[a]	$\left(\frac{k_e - k_2}{k_1 - k_2}\right)^3 \frac{k_1}{k_e} = (1 - v_2)^3$	Peterson–Hermans	$\frac{k_e}{k_1} = 1 + 3\beta v_2 + 3\beta^2\left(1 + \frac{\beta}{4} + \frac{\beta^3}{256} + \dots\right)v_2^2$
Ideal insulating limit	$\frac{k_e}{k_1} \equiv \frac{1 - v_2}{1 + 0.5 v_2}$		
Upper and lower bounds of ETC			
Wiener bounds		Hashin-Shtrikman bounds	
$\frac{1}{1 + v_2\,(1/\alpha - 1)} < \frac{k_e}{k_1} < 1 + v_2\,(\alpha - 1)$		$\frac{3\alpha + 2\alpha v_2(\alpha-1)}{3\alpha - v_2(\alpha-1)} > \frac{k_e}{k_1} > \frac{\alpha + 2 + 2v_2(\alpha-1)}{\alpha + 2 - v_2(\alpha-1)}$ for $\alpha > 1$ and $\frac{3\alpha + 2\alpha v_2(\alpha-1)}{3\alpha - v_2(\alpha-1)} < \frac{k_e}{k_1} < \frac{\alpha + 2 + 2v_2(\alpha-1)}{\alpha + 2 - v_2(\alpha-1)}$ for $\alpha < 1$.	

[a] The differential effective medium theory (D-EMT) is a cubic equation and has a holomorphic behavior. The cubic equation can be solved analytically (Weisstein; Toptan et al., 2020a). For this cubic equation, three possible solutions exist: (1) a single real root; (2) three real roots; or (3) one real and two complex roots. Roots of the third-order polynomial are computed accordingly and the largest real root of the cubic equation is assigned to the ETC (Toptan et al., 2019).

Table 4.2. Maximum packing fractions for different arrangements, taken from Nielsen (1974).

Type of packing	$v_{2,max}$	Type of packing	$v_{2,max}$
Spheres		***Rods/fibers***	
Face-centered cubic	0.7405	Uniaxial hexagonal close	0.907
Hexagonal close	0.7405	Uniaxial simple cubic	0.785
Body-centered cubic	0.680†	Uniaxial random	0.820
Simple cubic	0.524	3D random	0.520
Random close	0.637		
Random loose	0.601		

† Typo in Nielsen (1974) is corrected here.

state have similar mathematical forms (see Table 4.3) (Deng and Zheng, 2009). Most approaches developed for conductive problems can be extended to corresponding elastic problems or vice versa. Similarly, these methods can be applied to the Fickian diffusion for estimation of the effective diffusivity coefficient.

Table 4.3. Correspondence between elastic and conductive problems, taken from (Deng and Zheng, 2009, Table 1).

Problem	**Elasticity**	**Thermal Conductance**	**Electric Conductance**
Corresponding quantities	Stress $\boldsymbol{\tau}$	Heat flux $\boldsymbol{q}$	Current $\boldsymbol{J}$
	Displacement $\boldsymbol{u}$	Temperature T	Electrical potential ϕ
	Strain $\boldsymbol{\epsilon} = \frac{1}{2}(\nabla \boldsymbol{u} + (\nabla \boldsymbol{u})^{\intercal})$	Thermal gradient $\boldsymbol{g} = -\nabla T$	Electric field intensity $\boldsymbol{E} = -\nabla \phi$
	Elasticity tensor $\mathbb{C}$	Thermal conductivity tensor $\boldsymbol{K}$	Electric conductivity tensor $\boldsymbol{\sigma}$
Equilibrium eq.	$\nabla \cdot \boldsymbol{\tau} = 0$	$\nabla \cdot \boldsymbol{q} = 0$	$\nabla \cdot \boldsymbol{J} = 0$
Physical eq.	$\boldsymbol{\tau} = \mathbb{C} : \epsilon$	$\boldsymbol{q} = \boldsymbol{K} \cdot \boldsymbol{g}$	$\boldsymbol{J} = \boldsymbol{\sigma} \cdot \boldsymbol{E}$

4.2 Numerical Experiments

In this section, several numerical experiments using finite element analysis (FEA) are performed to assess and validate the aforementioned analytical models provided in Section 4.1. These are conducted for a domain with randomly dispersed, mono-sized spherical particles with varying material properties. Section 4.2.1 describes the methodology to obtain the ETC from the FEAs and the problem settings in each numerical experiment. Section 4.2.2 presents a parametric study to examine the effects of computational domain and sphere sizes. Section 4.2.3 provides and discusses the results.

4.2.1 Finite Element Methodology

The computational determination of ETC consists of three main steps (Floury et al., 2008): (1) realization of the composite structure; (2) solution of the steady state heat conduction; and (3) calculation of the ETC from the converged temperature profile. Details of these three steps are as follows:

Step 1 We create a computational domain of a representative volume element of material with randomly dispersed, mono-sized spheres in this study (see Figure 4.1.a). Then, adaptive meshing is utilized to resolve the phase interface by using two levels of refinement in the regions on the periphery of each sphere (Figure 4.1.b). The spheres are described by a field variable in a diffuse manner. This field variable equals 1 within the spheres and varies continuously, but steeply, to 0 within the second phase. The diffusive interface width, ϵ, is a user-controlled parameter, and is set to 10% of the sphere diameter here. In this study, the distance between centers of two adjacent spheres, d, is required to be at least one sphere diameter, D, so that there is no overlap between the spheres in the ETC calculation. Two numerical values of $d \geq d_{\min}$ are considered in the numerical experiments:

1. $d \geq D$, the spheres may come into contact and interact.
2. $d \geq 1.05D$, the spheres may be close to one another, but not interact.

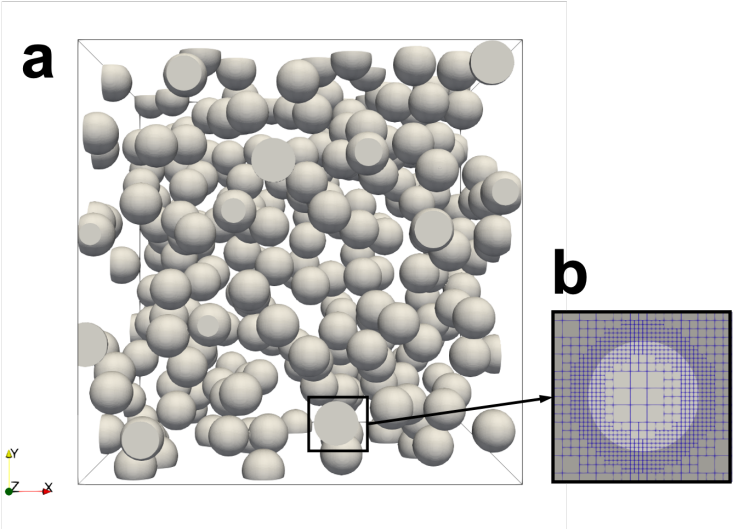

Figure 4.1. Computational domain and meshing. **(a)** Random packing of the mono-sized spheres embedded within a three-dimensional (3D) cubic domain, with $L/R = 20$. **(b)** A closer look at the mesh in the vicinity of the sphere periphery.

Step 2 The FEA simulations are performed for different volume fractions in each numerical experiment. Different volume fractions are obtained via varying the number of spheres in the computational domain. In this study, we consider the evaluation of ETC; therefore, only the heat conduction equation is solved. The thermal conductivities of both the host matrix and the spherical inclusions are chosen based on the analyses of interest. The thermal conductivity is weighted based on the volume fraction of each phase for a cell, including both phases.

Step 3 To obtain FEA results for a domain with spherical heterogeneities that is exposed to a predefined temperature gradient (hot and cold temperatures), the ETC is calculated from the converged temperature

field using the relation—obtained from Fourier's law—below:

$$k_{e,i} = -\frac{\dot{q}_i}{A}\frac{L}{(T_{hot} - T_{cold})} \tag{4.1}$$

where L and A are respectively the length and the cross-section of the cubic domain shown in Figure 4.1, $\dot{q}_i$ is the overall heat flow in the i-th direction, and $(T_{hot} - T_{cold})$ is the predefined temperature difference. The analytical ETC models are developed for three-dimensional (3D) geometries; therefore, 3D domains are considered here. Three FEA simulations are performed for each realization of the randomized material structure by applying the same temperature gradient in each principal direction. While the Dirichlet boundary conditions are applied to the faces associated with the imposed temperature gradient, the other faces are considered insulated. To obtain a single value for ETC from the set of simulations, an arithmetic mean of the thermal conductivities in the principal directions is computed.

4.2.2 Parametric Study

Performing the simulations in the full domain is computationally inefficient. To improve the computational efficiency and reduce the computational time, we performed a parametric study to investigate the effects of the domain edge length to the radius (i.e., L/R) on the effective thermal conductivity (k_e) calculations. To isolate other effects, the simulations are performed with randomly distributed, mono-sized particles in which we assigned constant thermal conductivity for each phase: 1.0 W/m-K for the spherical particles and 10.0 W/m-K for the continuous matrix (i.e., α =1/10). We consider a cubic domain with an edge length L and embedded spheres with a radius R. We keep the particle radius, volume fractions, and mesh densities identical while changing the domain dimensions. The minimum particle-to-particle distance, $d_{\min}$ is specified to avoid overlapping and interaction of spheres in this study.

Figure 4.2 shows the numerical results for the k_e/k_1 ratio with respect to the L/R ratio. Although the volume fraction cannot be directly defined by the user, the volume fraction is adjusted to keep $\upsilon_2 \cong 0.215$ by varying the number of spheres in the domains of the varying dimensions considered. From the computational results in Figure 4.2, the expected k_e/k_1 is found as ∼0.73 for all cases considered. The error bar around the expected k_e/k_1 estimates increases as the L/R ratio decreases. The overall error on the k_e/k_1 is found to be less than 1% for all considered L/R conditions in this study. L/R is set to 6 for the rest of the numerical experiments performed in Section 4.2.3. The computational result for the ETC, k_e, is the arithmetic mean of the thermal conductivities estimated in each principal direction. Therefore, the error bar represents the directional variations in k_e for a case with non-interacting spheres.

4.2.3 Results & Discussion

The FEAs are performed for the computational domain at various volume fractions. The ETC is evaluated for randomly dispersed mono-sized spherical inclusions embedded in a continuous matrix considering two cases: *Case I.* Thermal conductivity of the particles is less than the matrix ($\alpha < 1$; e.g., gas-filled spheres in a

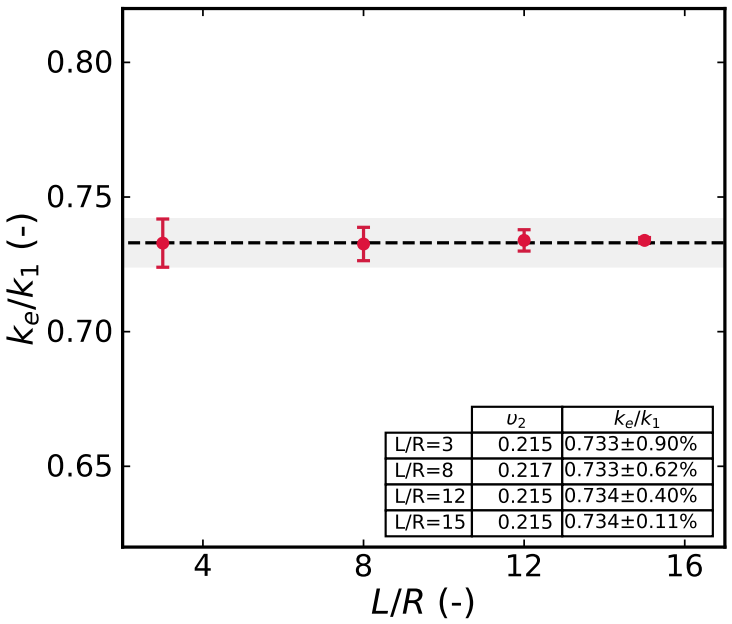

Figure 4.2. Effect of the characteristic domain length-to-particle radius, L/R, on k_e/k_1 at an approximately constant particle volume fraction of υ_2.

solid matrix). *Case II.* Thermal conductivity of the particles are greater than the continuous matrix ($\alpha > 1$). The details of the results are provided and discussed. As mentioned previously, $\alpha = 1$ corresponds to the homogeneous material; therefore, it is not evaluated here. The simulation results and model predictions are provided in terms of the thermal conductivity ratio of the effective-to-host matrix, k_e/k_1, to understand the impact of spherical inclusions with varying thermal conductivities. We use a common legend as tabulated in Table 4.4 for Figure 4.3–4.8.

Table 4.4. Common legend for Figure 4.3–4.8.

Tag	**Model**	**Tag**	**Model**	**Tag**	**Model**	**Tag**	**Model**
1	Maxwell	**5**	Bruggeman (EMT)	**9**	Chiew–Glandt	**13**	Parallel
2	Rayleigh	**6**	Hamilton–Crosser	**10**	Davis	**14**	D-EMT
3	Ratcliffe	**7**	Lewis-Nielsen	**11**	Peterson–Hermans	**15**	Ideal insulating
4	Kämpf	**8**	Levy	**12**	Series		

Case I ($\alpha < 1$)

The k_e/k_1 ratios are plotted with respect to the volume fraction of the continuous matrix υ_1 for arbitrarily chosen α =1/5 in Figure 4.3, α =1/10 in Figure 4.4, and α =1/20 in Figure 4.5. These scenarios are representative of poorly conducting spheres that are included in a more conductive medium. The inclusion of the

poorly conducting spheres degrades the heat transfer across the overall media. The parallel model overestimates the expected k_e/k_1 values from the FEAs, while the Kämpf, Levy, and series models underestimate those values. The numerical results from the analytical methods, such as Maxwell, Bruggeman (or effective medium theory (EMT)), Chiew-Glandt, Hamilton–Crosser, Davis, and D-EMT, lay within the error bars of the FEA-predictions; however, the best agreement is obtained from the D-EMT. The Chiew–Glandt model also results in similar predictions, but slightly overpredicts. Folsom et al. (2015) analyzed four models—the Maxwell, reduced form of Maxwell, Bruggeman (or EMT), and Chiew–Glandt models—for their TRISO analyses, assuming that the particle thermal conductivity is smaller than that of the continuous graphite matrix. They concluded that the Chiew–Glandt model is the best out of the four models they considered, which agrees with our analyses here.

Additionally, the ideal insulating limit is included on the plots to observe the validity of that assumption. Based on the results in Figure 4.5, this assumption is valid for $\alpha < 1/10$, where the expected behavior is captured as the thermal conductivity of the dispersed phase is significantly smaller than that of the host matrix.

Note that some of the models considered were not included in the plots because their predictions differed enough from those of the other models that they fell outside the plot limits. These include the Ratcliffe model, which significantly overestimated the expected behavior, and the Rayleigh, Lewis–Nielsen, and Peterson–Hermans models, which significantly underestimated the expected behavior for $\alpha < 1$. As mentioned previously, the numerical simulations are performed for two cases: $d \geq D$ and $d \geq 1.05D$ (non-interacting spheres). For the first case, the spheres may come into contact. In the presence of thermal contact between the spheres, a larger variability is observed on the estimated ETC results unless the thermal contacts are similar/symmetrical in each principal direction. The distribution of spheres is a random process; therefore, the occurrence of the solid contacts is also randomized. For the second case, the error bar is in the similar order of magnitude, which is primarily due to the selected L/R in the analysis (see Figure 4.2).

Case II ($\alpha > 1$)

The k_e/k_1 ratios are plotted with respect to the volume fraction of the continuous matrix v_1 for arbitrarily chosen α =5/1 in Figure 4.6, α =10/1 in Figure 4.7, and α =20/1 in Figure 4.8. These scenarios are representative of highly conductive spheres that are included in a less-conductive medium. The inclusion of conducting spheres enhances the ETC of the continuous medium. Two models lay within the error bars of the expected behavior, the Bruggeman (or EMT) and Levy models, for all three α values. The best agreement is obtained from the Bruggeman (or EMT) model. The Levy model is within the error bars of the expected values of the ETC for α =5 (see Figure 4.6); however, the predictions using this model are impaired for α=10, 20 (see Figure 4.7 and Figure 4.8, respectively). Similar to the previous case, a larger variability is observed on the estimated ETC results when the spheres come into contact non-symmetrically in each principal direction for the case with $d \geq D$.

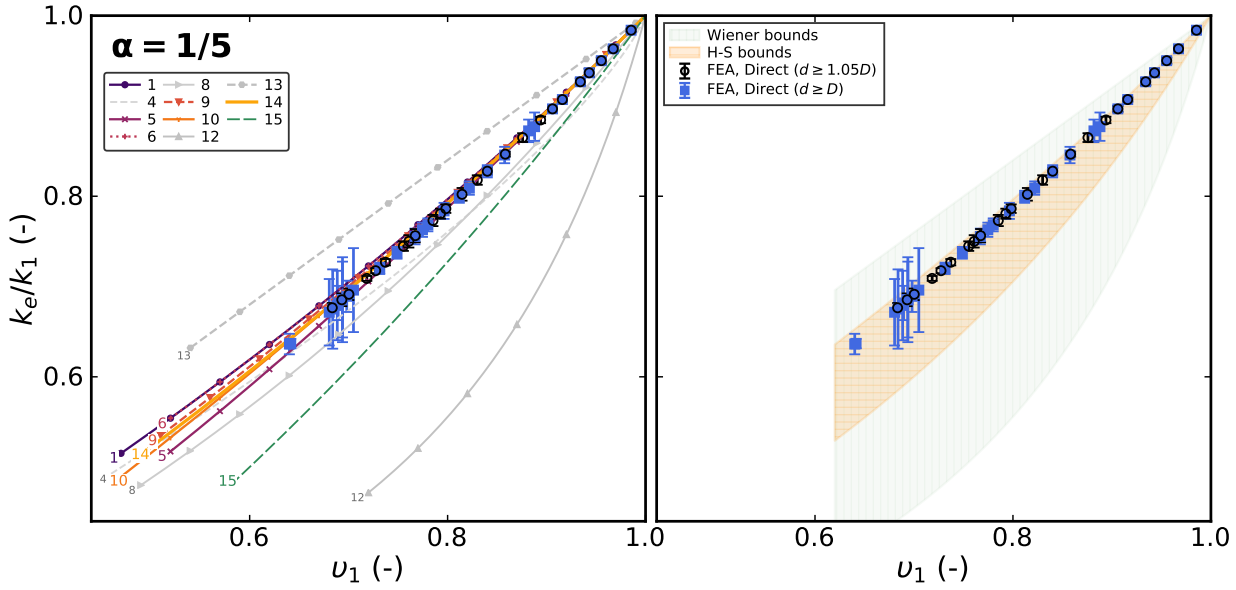

Figure 4.3. k_e/k_1 predictions with respect to υ_1 at α =1/5. The model predictions (*left plot*) and regions determined by upper and lower bounds of the k_e/k_1 predictions (*right plot*) are plotted against the expected FEA predictions.

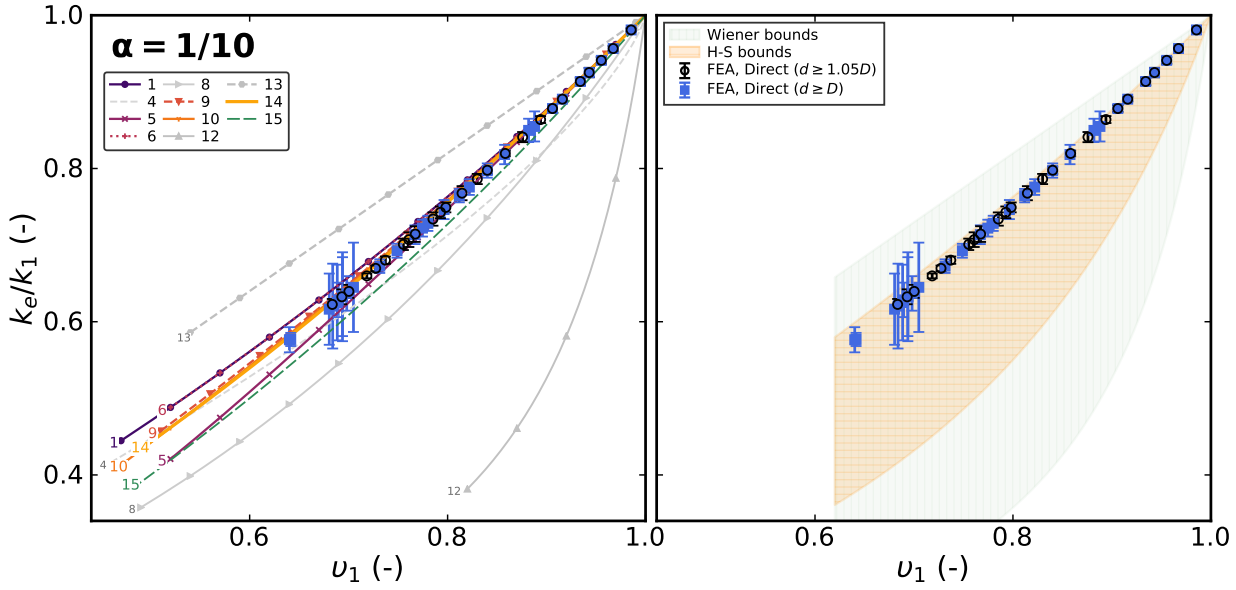

Figure 4.4. k_e/k_1 predictions with respect to υ_1 at α =1/10. The model predictions (*left plot*) and regions determined by upper and lower bounds of the k_e/k_1 predictions (*right plot*) are plotted against the expected FEA predictions.

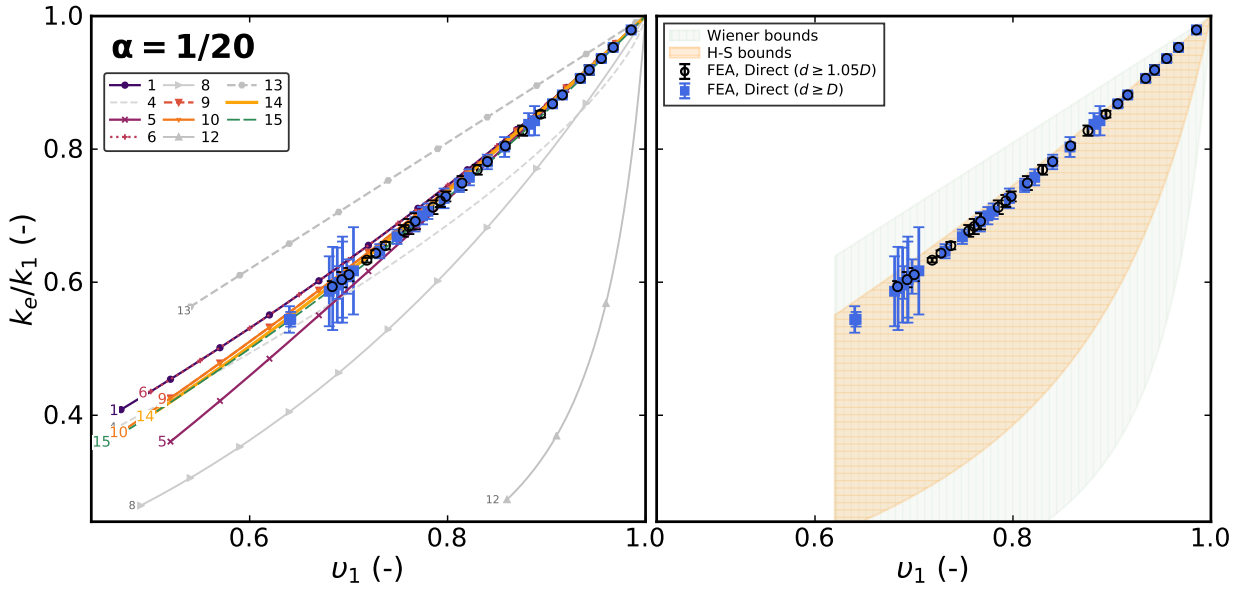

Figure 4.5. k_e/k_1 predictions with respect to υ_1 at α =1/20. The model predictions (*left plot*) and regions determined by upper and lower bounds of the k_e/k_1 predictions (*right plot*) are plotted against the expected FEA predictions.

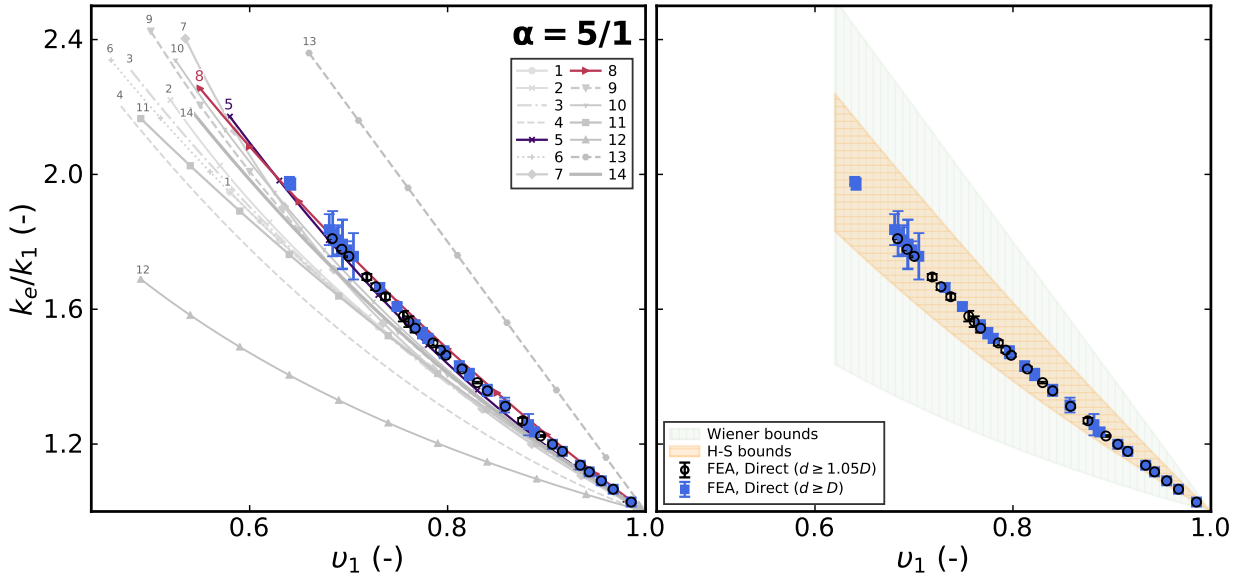

Figure 4.6. k_e/k_1 predictions with respect to υ_1 at α =5/1. The model predictions (*left plot*) and regions determined by upper and lower bounds of the k_e/k_1 predictions (*right plot*) are plotted against the expected FEA predictions.

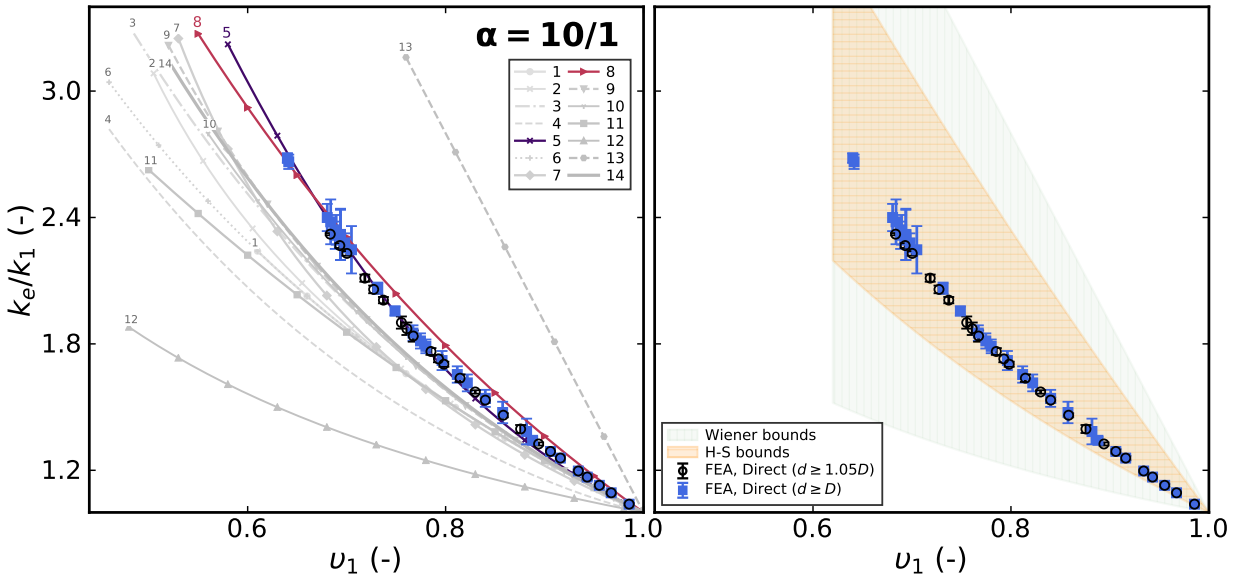

Figure 4.7. k_e/k_1 predictions with respect to υ_1 at α =10/1. The model predictions (*left plot*) and regions determined by upper and lower bounds of the k_e/k_1 predictions (*right plot*) are plotted against the expected FEA predictions.

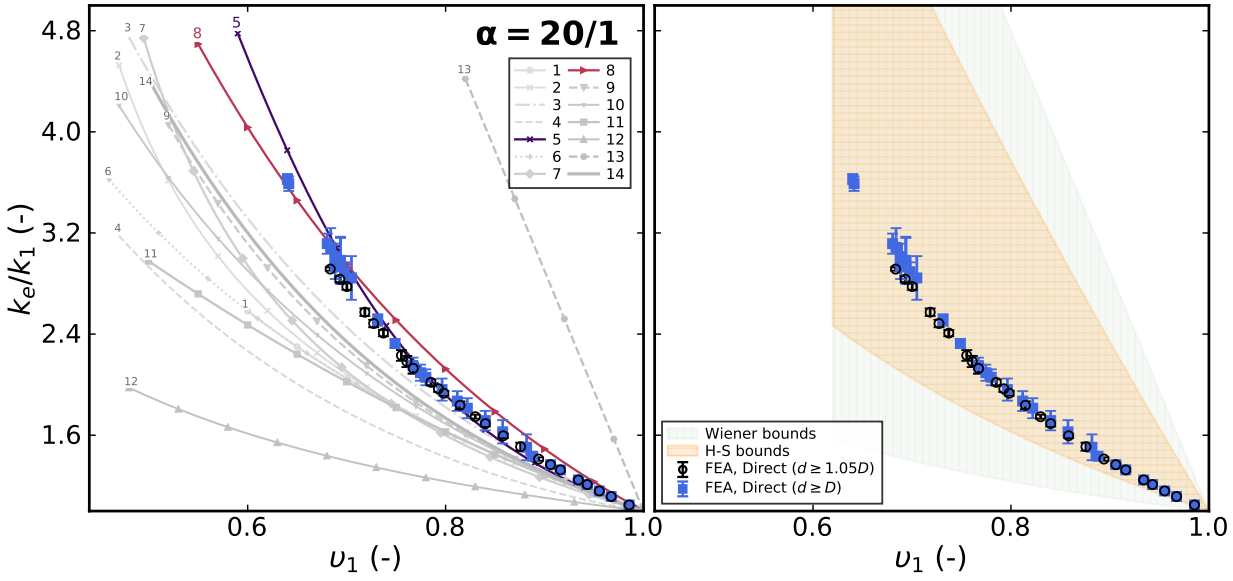

Figure 4.8. k_e/k_1 predictions with respect to υ_1 at α =20/1. The model predictions (*left plot*) and regions determined by upper and lower bounds of the k_e/k_1 predictions (*right plot*) are plotted against the expected FEA predictions.

4.3 TRISO Applications

An important application for these homogenization methods is in the analysis of fuel forms (e.g., pebble or compact), which can each contain over 10,000 TRISO particles. Each TRISO particle (see Figure 4.9) has a fuel kernel, which is surrounded by a buffer and three coating layers: (1) an inner layer of high strength PyC, referred to as IPyC; (2) a layer of SiC; and (3) an outer layer of PyC, referred to as OPyC. These TRISO particles are embedded in a host matrix within the fuel form. The homogenization process for the fuel pebble is schematically illustrated in Figure 4.9, and is performed in two stages: (1) particle-level; and (2) pebble-level. Details of the models are described and discussed in Section 4.3.1 and Section 4.3.2, respectively.

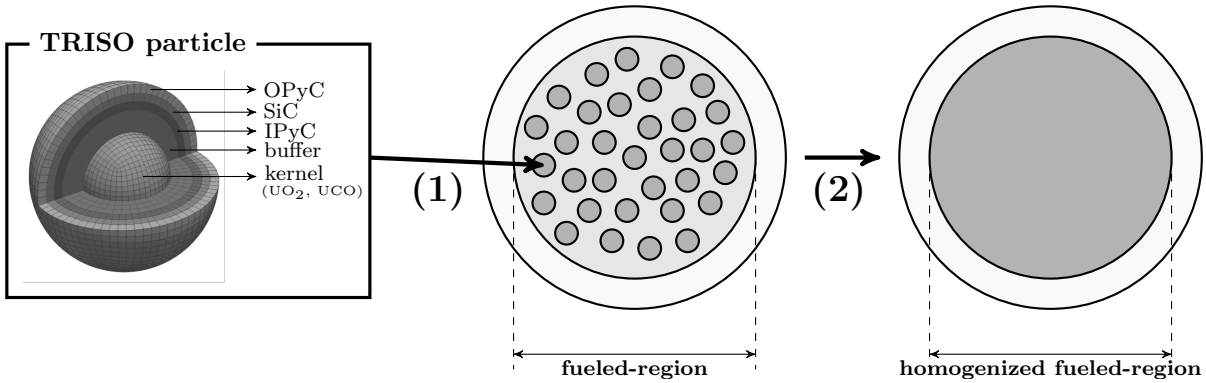

Figure 4.9. Schematic illustration of a two-stage homogenization applied to the standard fuel pebble (not to scale). (1) At the particle level, a representative thermal conductivity is computed for the five-layer TRISO particle and assigned to the homogeneous/smeared particle. (2) At the pebble level, two regions exist (fueled and fuel-free regions). The fueled region containing the TRISO particles is homogenized and a representative thermal conductivity is computed for this region.

4.3.1 Homogenization at the Particle Level

At the particle level, a representative thermal conductivity is computed for the five-layer TRISO particle and assigned to the homogeneous/smeared particle. We employ the same methodology as described in Section 4.2 to obtain the ETC for the given material condition. In the previous section, we confirmed that the D-EMT method most accurately predicts the expected behavior for $\alpha < 1.0$ and the Bruggeman (or EMT) model for $\alpha > 1.0$. In this application, α is computed as k_p/k_{graphite} where k_p is the particle thermal conductivity and k_{graphite} is the thermal conductivity of graphite matrix. In this case, k_p is significantly smaller than k_{graphite} (see Figure 4.11); therefore, $\alpha < 1.0$ and it is reasonable to use the D-EMT method (see Table 4.1). Using

the terminology for TRISO applications, the D-EMT method is rewritten as follows:

$$\left(\frac{k_{fr}-k_p}{k_{\text{graphite}}-k_p}\right)^3 \frac{k_{\text{graphite}}}{k_{fr}} = (1-PF)^3 \tag{4.2}$$

where k_{fr} is the thermal conductivity of homogenized fueled-region that contains TRISO fuel particles, k_p is the thermal conductivity of the smeared TRISO particle that is estimated based on its geometry and the thermal conductivities of all its constituent layers, and PF is the packing fraction of TRISO particles (i.e., $PF = \upsilon_2$). PF is defined as the ratio of the volume of the TRISO particles to the volume of the embedding matrix as:

$$PF = \frac{1}{V_{fr}} \left(\sum_{i=1}^{N_p} V_{p,i}\right) \tag{4.3}$$

where N_p is the number of TRISO particles embedded in the matrix's fueled region, V_p is the average volume of a TRISO particle, and V_{fr} is the volume of the matrix's fueled region (i.e., the volume containing TRISO particles, as shown in Figure 4.9).

The above homogenization method (or other mentioned methods in Section 4.1) has been developed for a continuous medium with embedded homogeneous spheres. Here, we attempt to obtain a rough estimate of the thermal conductivity for a five-layer TRISO particle. That is typically computed from the numerical simulations in a given set of material setting, where k_p is estimated from its impact on the ETC of overall domain due to its presence in the structure or, in other words, determined from the perturbation to the far-field temperature profile caused by the particle (Folsom et al., 2015). The exact value of k_{fr} is determined from the FEAs and inserted into the following relation to calculate the particle thermal conductivity. This relation is obtained from Equation 4.2—basically rewritten for k_p for known PF, k_{fr}, and k_{graphite}—as:

$$k_p = \frac{1}{1-\eta}\left(k_{fr} - \eta k_{\text{graphite}}\right) \tag{4.4}$$

with $\eta = (1-PF)\sqrt[3]{k_{fr}/k_{\text{graphite}}}$.

Considering the representative values of nominal thermal conductivity of each particle layer (see Table 4.5), the particle thermal conductivity has been estimated as 4.13 W/m-K by other researchers in the literature (Stainsby et al., 2009; Folsom et al., 2015). This value was obtained by back-calculating the thermal conductivity using the Maxwell model. In their studies, the graphite thermal conductivity of 15.0 W/m-K was considered for a particle packing fraction of ∼10%. Herein, we repeat the same numerical experiment using a simple cubic configuration for the particle packing in a box domain. The particle thermal conductivity is determined to be 4.08 W/m-K (within 1% error of 4.13 W/m-K) for the same set of nominal conditions (Stainsby et al., 2009; Folsom et al., 2015) and 2.53 W/m-K for the new set of conditions examined in this study. It is important to note that we use the D-EMT method instead of the Maxwell model as used in the prior studies.

We extended our analysis to perform a parametric study where we varied the packing fraction (PF =0.15, 0.25, and 0.35, as shown in Figure 4.10) and the graphite matrix thermal conductivity (k_{graphite} =15.0, 30.0,

Table 4.5. Nominal values used for dimensions and thermal conductivity of each layer.

Layer	**O.D. (µm)**	**k (W/m-K)**	
		Prior (Folsom et al. (2015)) Stainsby et al. (2009))	**Present**
Fuel kernel (UO_2, UCO)	500	3.7	3.8[†]
Buffer	690	0.5	0.5
Inner pyrolytic carbon (IPyC)	770	4.0	4.0
Silicon carbide (SiC)	840	16.0	21.9[‡]
Outer pyrolytic carbon (OPyC)	920	4.0	4.0

[†] The thermal conductivity of UO_2 and UCO at 900 K is approximately 3.8 W/m-K (e.g., 3.75 for UO_2 and 3.80 W/m-K for UCO).
[‡] Monolithic SiC value at 900 K according to the Miller model (Miller et al., September, 2018).

45.0, and 60.0 W/m-K) for the two cases tabulated in Table 4.5. Figure 4.12 shows the computational results of the parametric study. From these analyses, influence of particle's presence increases on the overall homogenized thermal conductivity as the graphite thermal conductivity increases. The average particle thermal conductivity is estimated as 4.57±0.55 W/m-K for the first case and 5.26±0.52 W/m-K for the second case. These values are closer to the corresponding volume-averaged values of particle thermal conductivity, 4.62 W/m-K for the first case and 5.48 W/m-K for the second case, given material conditions. The volume-averaged k_p values are independent of the packing fraction and the thermal interactions between particles.

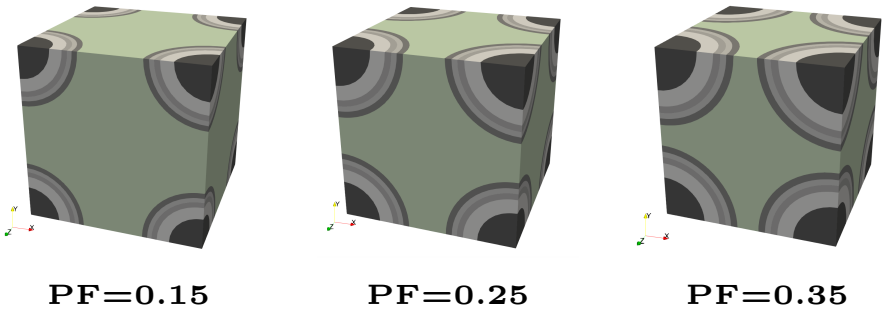

Figure 4.10. The computational domain containing five-layer TRISO particles in a simple cubic configuration. The packing fraction of the particles is adjusted by changing the dimensions of the computational domain. Note that the arrangement of the particles within a matrix will affect thermal interactions between the particles and maximum packing of the particles within the matrix for the thermal analyses.

4.3.2 Homogenization at the Fuel Pebble Level

Two regions exist at the pebble level: fueled and fuel-free regions. The fueled region containing the TRISO particles is homogenized, and a representative thermal conductivity is computed for this region. The thermal

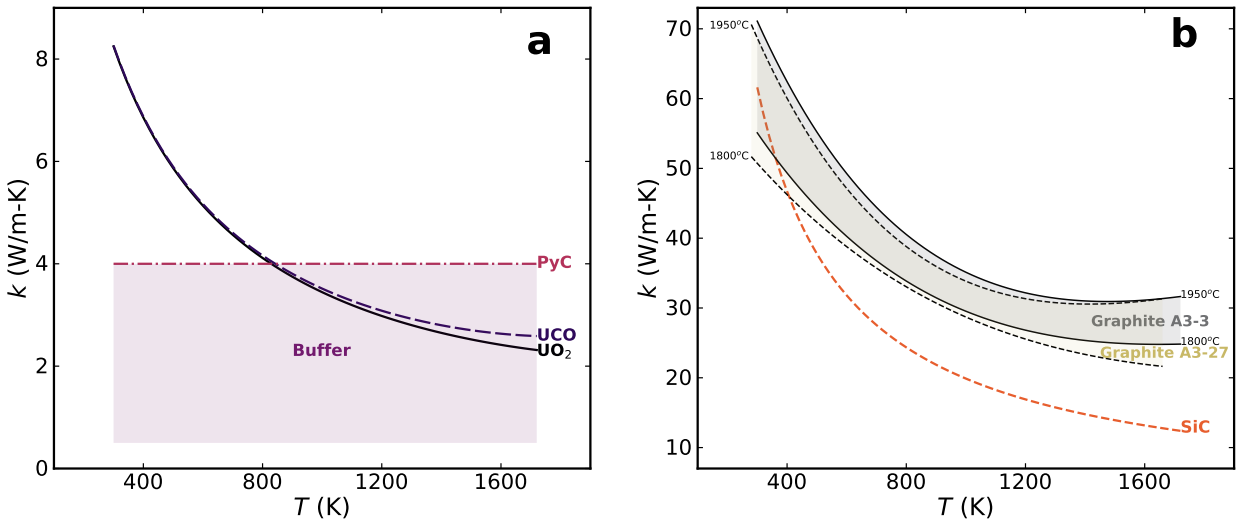

Figure 4.11. Thermal conductivity of: **(a)** each TRISO particle layer; and **(b)** unirradiated graphite matrix over the arbitrarily chosen temperature range. The Halden model is used for UO_2 and the PARFUME model for UCO to compute thermal conductivity of the fuel kernel. The buffer thermal conductivity is interpolated between 0.5 and 4.0 W/m-K based upon the buffer density (Ho, July, 1993). The PyC thermal conductivity is set to a constant value of 4.0 W/m-K (Nabielek et al., March, 1992). The SiC thermal conductivity is computed according to the Miller model (Miller et al., September, 2018) (see Hales et al. (2020); Jiang et al. (2021) for the mathematical expressions of all mentioned models). The thermal conductivity of the graphite matrix (A3-3 and A3-27, heat-treated at 1800°C and 1950°C during fabrication) is computed according to Miller et al. (September, 2018); Gontard and Nabielek (July, 1990) (see Equation 4.6). Thermal conductivities of the materials within the TRISO particle is significantly less than that of the graphite matrix. Herein, we do not encounter the effects of irradiation on the thermal conductivity. There will be additional degradation on the fuel thermal conductivity, which will further decrease the thermal conductivity.

conductivity of the matrix material is given by Miller et al. (September, 2018); Gontard and Nabielek (July, 1990). The correlation is given as a function of fast fluence with a neutron energy threshold of E > 0.18 MeV. The thermal conductivity k_{graphite} (W/m-K) of the graphite matrix is:

$$k_{\text{graphite}} = k_{\text{unirr}} \kappa_\phi \kappa_\rho \tag{4.5}$$

where k_{unirr} (W/m-K) is the temperature-dependent thermal conductivity of the unirradiated matrix material, κ_ϕ (-) is a correction for irradiation damage, and κ_ρ (-) is a correction factor for densities other than that of the reference material.

The thermal conductivity k_{unirr} (W/m-K) of the unirradiated matrix depends on the nature of the matrix material (A3-3 or A3-27) and temperature of the final heat treatment during fabrication (1800°C or 1950°C) (Gontard and Nabielek, July, 1990):

$$k_{\text{unirr}} = k_{100} \left[1 - \alpha(T - 100)e^{-\delta T}\right] \tag{4.6}$$

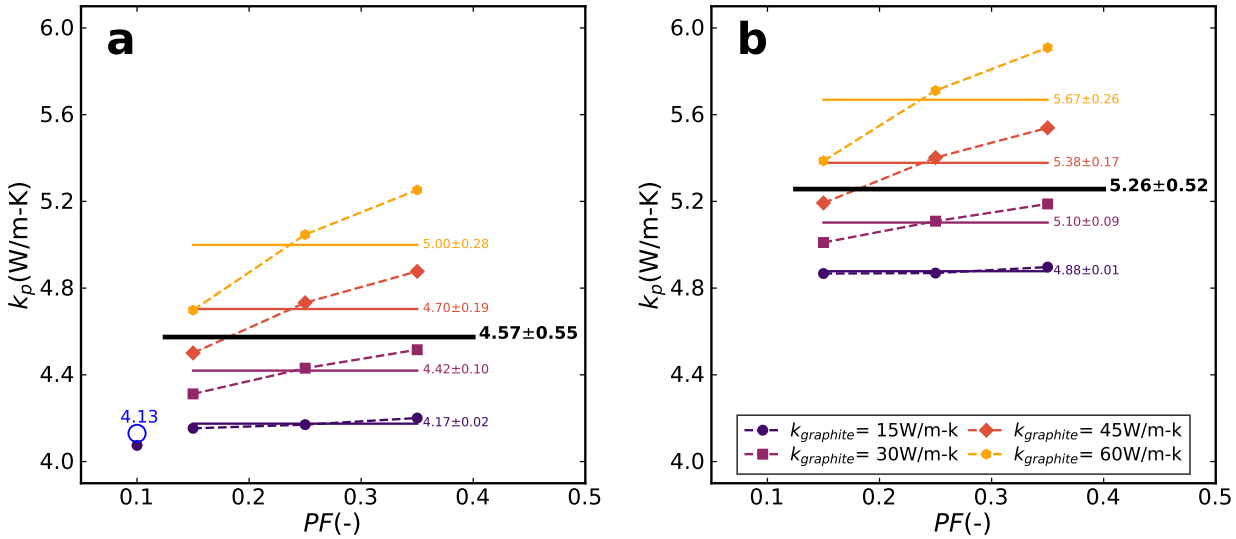

Figure 4.12. The particle thermal conductivity, k_p, determined for the two material conditions tabulated in Table 4.5: **(a)** with thermal conductivities given by Stainsby et al. (2009); Folsom et al. (2015); and **(b)** with thermal conductivities that are computed at 900 K (according to the models plotted in Figure 4.11). The black solid lines represent the average particle thermal conductivity that is computed considering all computational results.

where k_{100} (W/m-K) is the thermal conductivity of non-porous material at 100°C. The empirical coefficients, α and δ, are tabulated in Table 4.6, and T (°C) is the temperature of the matrix.

Table 4.6. Coefficients for unirradiated thermal conductivity (Gontard and Nabielek, July, 1990).

Material	**Heat treatment**	k_{100} **(W/m-K)**	α**(-)**	δ**(-)**
A3-3	1800°C	50.8	1.1810×10^{-3}	7.8453×10^{-4}
	1950°C	64.6	1.4079×10^{-3}	9.0739×10^{-4}
A3-27	1800°C	47.4	9.7556×10^{-4}	6.0360×10^{-4}
	1950°C	62.2	1.4621×10^{-3}	9.6050×10^{-4}

Neutron fluence degrades the thermal conductivity of the matrix. A correction factor, κ_ϕ (-), based on experimental data is applied to take the effect of irradiation damage into account (Gontard and Nabielek, July, 1990), given by:

$$\kappa_\phi = 1.0 - (0.94 - 0.604t_C)\left(1 - e^{\left[-(2.96-1.955t_C)\frac{\phi}{1.52}\right]}\right) - \left(0.043t_C - 0.008t_C^8\right)\frac{\phi}{1.52} \tag{4.7}$$

where $t_C = T/1000$ is the reduced temperature (°C), T is temperature (°C), and ϕ (10^{25} n/m^2, E > 0.18 MeV) is the fast neutron fluence.

The correction factor, κ_ρ (-), is applied for densities other than the reference material ($\rho_0 = 1700\,\text{kg/m}^3$)

used to obtain the experimental data on unirradiated material. It is given by Miller et al. (September, 2018) as:

$$\kappa_\rho = \frac{\rho}{\rho_0} \tag{4.8}$$

where ρ is the density of the matrix.

Finally, the presence of TRISO particles in the matrix modifies its thermal conductivity. The packing fraction, PF (i.e., $PF = \upsilon_2$), is defined as the ratio of the volume of the TRISO particles to the volume of the embedding matrix as in Equation 4.3. If the fuel form (e.g., compact or pebble) contains a fuel-free region, the volume of that region is not included in the calculation of the packing fraction (a fuel specification). The thermal conductivity of the fueled zone is based on the homogenization of TRISO particles and the matrix to produce an effective (or homogenized) thermal conductivity. The homogenization method differs from the factor presented in Gontard and Nabielek (July, 1990), which corresponds to the ideal insulating limit, and is valid for the moderate ranges of the packing fraction and $\alpha \ll 1$. In this study, we examined a variety of analytical ETC methods (see Section 4.1). However, the best agreement is obtained by the D-EMT method for $\alpha = k_p/k_{\text{graphite}} < 1.0$ (see Figure 4.11). Using the terminology for the TRISO applications, the model is rewritten as in Equation 4.2 to determine the thermal conductivity of the homogenized fueled region, k_{fr}. The particle thermal conductivity is often set to a constant value that is determined from the analyses in Section 4.3.1. The assumption of a constant particle thermal conductivity is a valid assumption in the pebble homogenization for $\alpha < 1$ (i.e., when the particles are less conductive than the host matrix). To illustrate this, we arbitrarily varied the thermal conductivity ratio α for packing fractions varying between 0.0 and 0.40. From the results shown in Figure 4.13 for the $k_{fr}/k_{\text{graphite}}$ ratio, the homogenized thermal conductivity for the fueled-region will be located in a 10% estimation band where the graphite matrix thermal conductivity is five times or greater than the particle thermal conductivity, a 4% estimation band where the graphite matrix thermal conductivity is ten times or greater than the particle thermal conductivity, and so on. It is evident that this estimation band for $k_{fr}/k_{\text{graphite}}$ narrows as the $\alpha = k_p/k_{\text{graphite}}$ ratio decreases. Therefore, we conclude that the homogenized thermal conductivity of the fueled region becomes insensitive to the particle thermal conductivity once the matrix thermal conductivity becomes significantly larger than the thermal conductivity of the particle and its constituent layers.

In the present case study, the TRISO particles were embedded in a graphite matrix. The above discussions are valid for this specific case because α is significantly smaller than one due to the significantly higher thermal conductivity of the graphite relative to the TRISO particles. However, for cases with a matrix composed of other materials (e.g., a SiC matrix whose thermal conductivity is similar to that of the particle layers as shown in Figure 4.11), the homogenization will be highly sensitive to the computed particle thermal conductivity, and α can even be greater than one. Therefore, the accurate computation of the particle thermal conductivity can be critical for some cases, even though that is not the case with the graphite matrix under unirradiated conditions considered in this analysis.

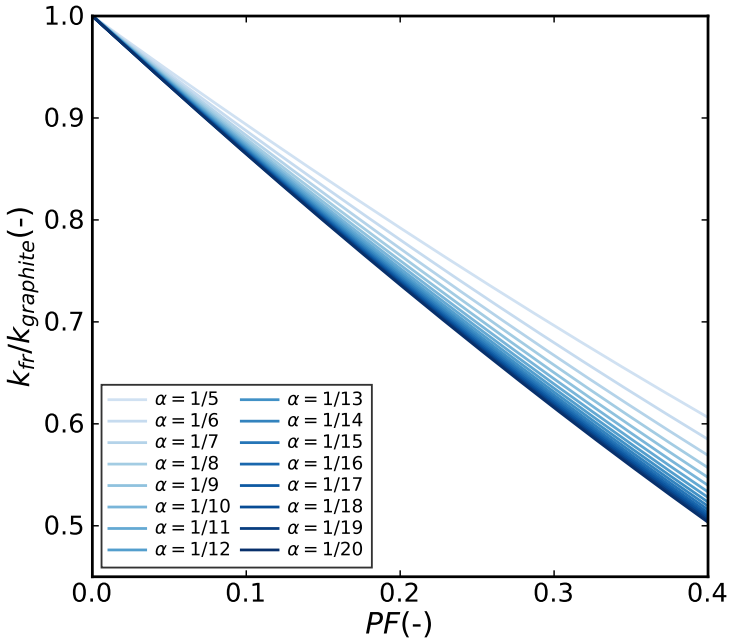

Figure 4.13. The homogenized thermal conductivity of the fueled-region to the graphite matrix thermal conductivity versus the packing fraction for various $\alpha = k_p/k_{\text{graphite}}$ ratios.

4.4 Effective Diffusivity Coefficient

The material presented here is a subset of the information found in Toptan et al. (2022a). The governing steady-state equations of the elasticity, thermal conduction, and electrical conduction problems take similar mathematical forms (Table 4.3). Most approaches developed for solving conductive problems can also be extended to corresponding elastic problems, as well as to the simplified Fickian diffusion widely used for calculations in engineering applications. By considering heat conduction to be analogous with simplified Fickian diffusion (or fission product species conservation or mass diffusion), we can apply the same analytical homogenization methods to obtain the EDC as used to obtain the ETC.

Based on our ETC-related work in previous sections, the EMT showed the best agreement for $\alpha > 1$ while D-EMT for $\alpha < 1$, where α is defined as the ratio of thermal conductivities of particles to continuous medium for the ETC calculations. In this study, we selected only the two recommended ETC models (see Table 4.1) to determine whether our hypothesis was valid for EDC calculations.

Fission product species conservation is given by Equation 5.10, where the mass flux is expressed as $\boldsymbol{J} = -D\nabla C$, using the diffusion coefficient, D (m^2/s), which is defined in a temperature-dependent Arrhenius form as:

$$D = \sum_i D_{0,i} \exp\left(-\frac{Q_i}{RT}\right), \tag{4.9}$$

where Q is the activation energy, R is the universal gas constant, and T is the temperature.

We performed several numerical experiments using the finite-element-based code BISON (Williamson et al., 2021), and assessed the recommended analytical models for EDC. These numerical experiments were conducted for a domain with randomly dispersed, mono-sized spherical particles featuring varying material properties.

4.4.1 Methods

Here, we describe the methodology for obtaining, in three main steps, the EDC from the FEAs, along with the problem settings in each, based on the converged concentration profile for the EDC.

Step 1. We create a 3D cubic computational domain for a representative volume element of material with randomly dispersed, mono-sized spheres (see Figure 4.14). The spheres are described in a diffuse manner by a field variable. This field variable equals one within the spheres, and varies continuously—but steeply—to zero within the secondary phase. The diffusive interface width is a user-controlled parameter, here set to 10% of the sphere diameter. Adaptive meshing is utilized to resolve the phase interface by using two levels of refinement in the periphery regions of each sphere. The distance between the centers of two adjacent spheres, d, is required to be at least one sphere diameter, D, in order to avoid overlap between the spheres (i.e., $d \geq d_{\min} = 1.05D$).

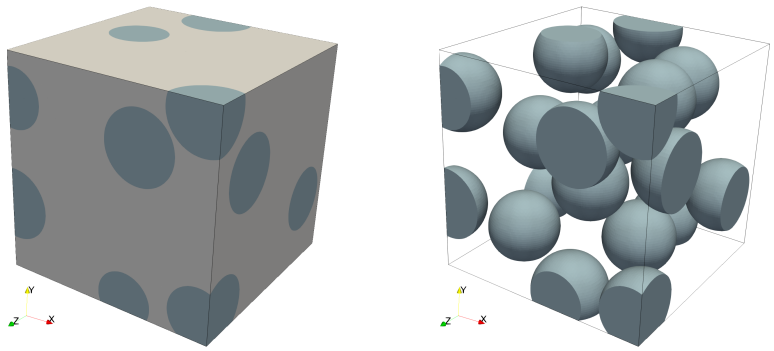

(a) (b)

Figure 4.14. 3D constructed computational domain: (a) matrix with embedded spheres; (b) random distribution of mono-sized spheres (the matrix is hidden for ease of visibility). The characteristic domain length-to-particle radius, L/R, is 6. The volume fraction of the continuous matrix, v_1, is 0.726. The minimum distance between the centers of two adjacent spheres is set to one sphere diameter, D (i.e., $d_{\min} = D$).

Step 2. FEA simulations are performed for different volume fractions in each numerical experiment. Different volume fractions are obtained by varying the number of spheres in the computational domain. The present study includes evaluation of EDC; therefore, only Equation 5.10 is solved. The diffusivity coefficients of both the host matrix and the spherical inclusions are chosen based on the analyses of interest. The diffusivity coefficient is weighted based on the volume fraction of each phase for a cell including both

phases. The numerical simulations are performed under a packing fraction of up to approximately 40%.

Step 3. The EDC is calculated from the converged concentration field, using the relation from Mu et al. (2007):

$$D_{e,x} = \frac{\int_A \int D_b \left(\frac{\partial C}{\partial x}\right)_{x=L} dydz}{\frac{(C_2 - C_1)}{L} A}, \tag{4.10}$$

where D_b is the bulk diffusivity coefficient (or matrix diffusivity coefficient), C_1 and C_2 are the concentration values applied to each opposing surface in the unidirectional diffusion process, and A is the surface area. To obtain a single value for EDC from the set of simulations, an arithmetic mean of the diffusivity coefficients in the principal directions is employed:

$$D_e = \frac{1}{n}\left(\sum_{i=1}^{n} D_{e,i}\right), \tag{4.11}$$

where $D_{e,i}$ represents the diffusivity coefficient in each principal direction (via Equation 4.10), and n is the number of principal directions (i.e., $n = 3$ for 3D).

4.4.2 Results & Discussion

The FEAs were performed for the computational domain at various volume fractions. The EDC was evaluated for randomly dispersed mono-sized spherical inclusions embedded in a continuous matrix, considering two cases: (1) the diffusivity coefficient of the particles is less than the continuous matrix ($\alpha = D_2/D_1 < 1$), and (2) the diffusivity coefficient of the particles exceeds the continuous matrix ($\alpha > 1$). The detailed results are provided and discussed. Note that $\alpha = 1$ corresponds to the homogeneous material; thus, it is not evaluated here.

The simulation results and model predictions are provided in terms of the diffusivity coefficients ratio of the effective to host matrix, D_e/D_1, to understand the impact of spherical inclusions (with varying diffusivity coefficients) as a function of the volume fraction of the matrix, υ_1. For the computational considerations, the characteristic domain length-to-particle ratio, L/R, was set to 6 in these analyses—a value found sufficient in the parametric study performed in Toptan et al. (2021). Only the uncertainty around the mean FEA results varies with the chosen L/R ratio, which is indicated by the error bars around the FEA predictions.

4.4.2.1 Case I. The diffusivity coefficient of the particles is less than the continuous matrix ($\alpha < 1$).

Figure 4.15 shows the concentration profiles for the case featuring $\alpha < 1$ in each unidirectional diffusion process in the principal direction at a fixed volume fraction (i.e., 0.726) of the continuous matrix, υ_1, for the arbitrarily chosen α =1×10^{-4}, 0.1, and 0.5. See Figure 4.14 for the actual particle locations with υ_1 =0.726. The FEA-predicted D_e was estimated based on the average values of realizations performed in all three principal directions (plotted in Figure 4.17a), as well as on the model predictions from both EMT and D-EMT. In this case, the diffusion gradient across the domain is relatively smooth at $\alpha = 0.5$ (see

Figure 4.15c). The presence of the particles within the domain becomes more pronounced on the diffusion process as α approaches zero (see Figures 4.15a and 4.15b).

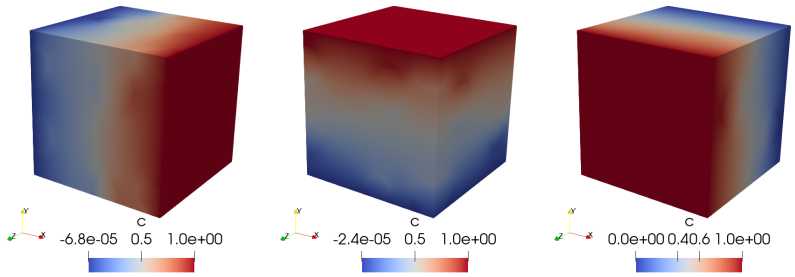

(a) α =1×10^{-4}

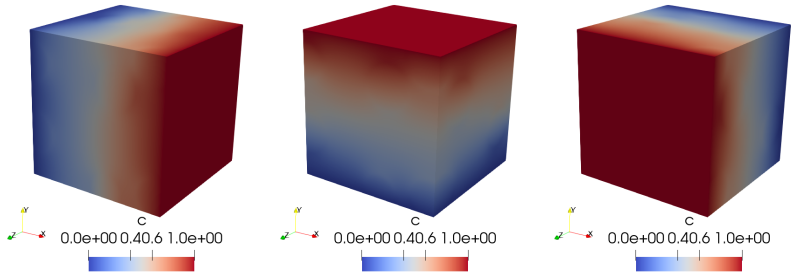

(b) α =0.1

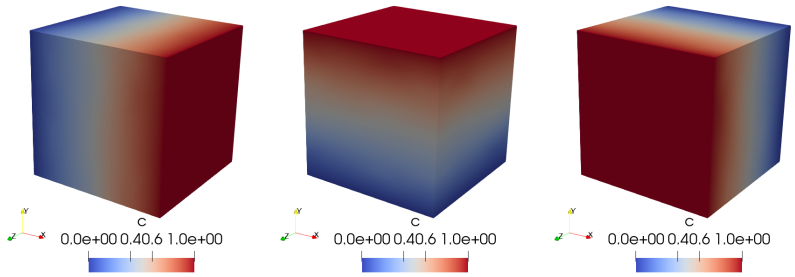

(c) α =0.5

Figure 4.15. Concentration profile contours, obtained via the unidirectional diffusion process, in the x-, y-, and z-directions at a fixed v_1 of 0.726 (see Figure 4.14 for the actual particle locations) for (a) $\alpha = 1\times10^{-4}$, (b) $\alpha = 0.1$, and (c) $\alpha = 0.5$. The FEA-predicted D_e was estimated from the average of three realizations performed in each principal direction.

Figure 4.17a shows the model and FEA predictions for D_e/D_1 as a function of v_1 for the arbitrarily chosen $\alpha = 1\times10^{-4}$, 0.1, and 0.5. Unsurprisingly, introducing fewer diffusive particles into the system degrades its overall diffusivity coefficient. As expected, the material behaves homogeneously at $v_1 = 1$. The models behave similarly in regard to $\alpha = 0.5$, but significantly differ from each other as α becomes smaller. As suggested in Toptan et al. (2021), the D-EMT accurately represents the expected behavior for $\alpha < 1$ in estimating EDC. The numerical simulations were performed under a packing fraction of up to approximately

40%. The maximum packing fraction for different arrangements (e.g., face-centered cubic (FCC), hexagonal close (HC), random close/loose, and simple cubic (SC)) are indicated in Figure 4.17a (Nielsen, 1974).

4.4.2.2 Case II. The diffusivity coefficient of the particles is greater than the continuous matrix ($\alpha > 1$).

Figure 4.16 shows the concentration profiles for the case with $\alpha > 1$. Similarly, the unidirectional diffusion process is illustrated in each principal direction at a fixed v_1 of 0.726 for the arbitrarily chosen $\alpha = 2.0$, 10.0, and 100.0. See Figure 4.14 for the actual particle locations at $v_1 = 0.726$.

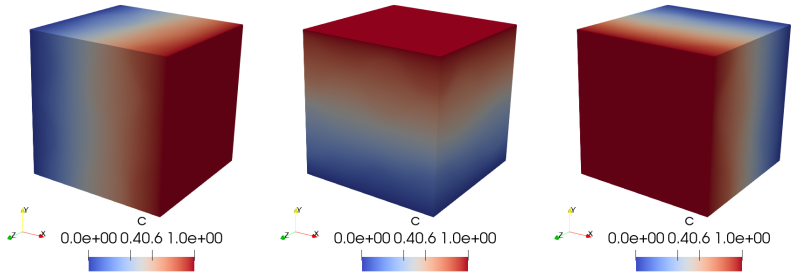

(a) α =2.0

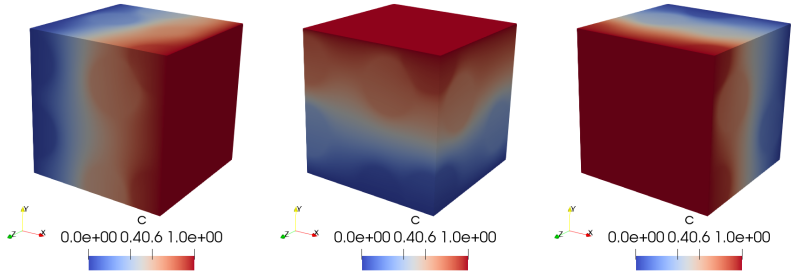

(b) α =10.0

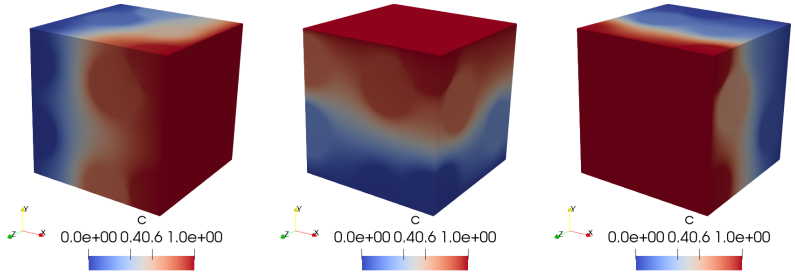

(c) α =100.0

Figure 4.16. Concentration profile contours, obtained via the unidirectional diffusion process, in the x-, y-, and z-direction at a fixed v_1 of 0.726 (see Figure 4.14 for the actual particle locations) for (a) $\alpha = 2.0$, (b) $\alpha = 10.0$, and (c) $\alpha = 100.0$. The FEA-predicted D_e was estimated from the average of three realizations performed in each principal direction.

The FEA and model predictions for D_e/D_1 are plotted in Figure 4.17b as a function of v_1 at the selected α values. The inclusion of more diffusive particles into the medium increases the system's overall diffusivity coefficient. The models only behave similarly at a packing fraction of up to 10% (i.e., $v_2 = 1 - v_1 = 0.10$), and significantly vary from each other when more particles are present in the system at higher α values. As suggested in Toptan et al. (2021) for the ETC, the EMT represents the expected behavior comparatively better for $\alpha > 1$ in estimating the EDC.

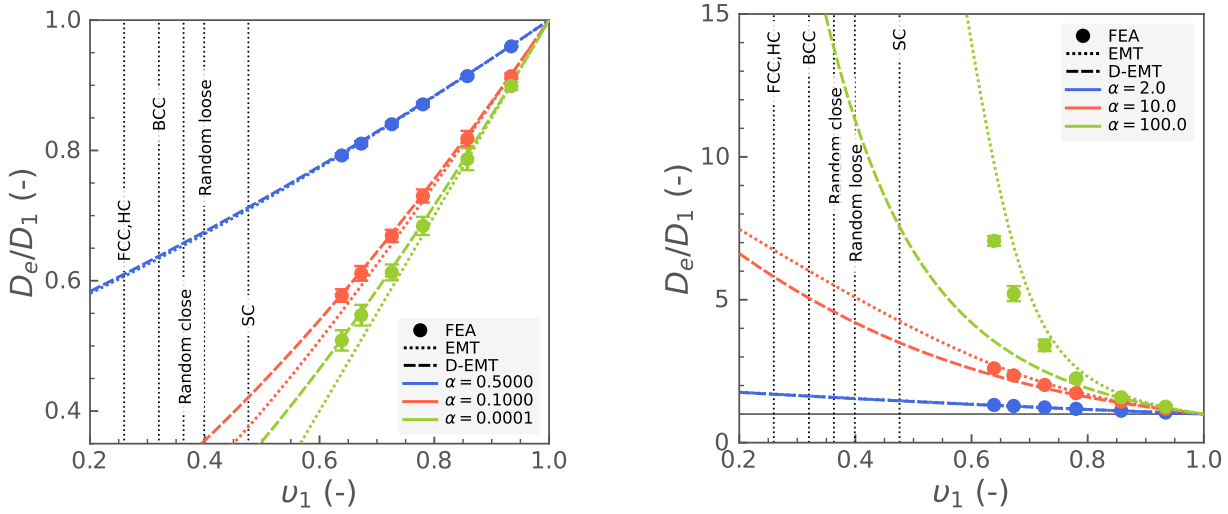

(a) $\alpha < 1$

(b) $\alpha > 1$

Figure 4.17. D_e/D_1 predictions with respect to v_1 for (a) $\alpha < 1$ and (b) $\alpha > 1$. The model predictions and regions determined by the upper and lower bounds of the D_e/D_1 predictions are plotted against the expected FEA predictions. The packing fraction, v_2, can be obtained from $1 - v_1$ in a binary system. The dashed vertical lines represent the maximum packing fractions for different arrangements (e.g., FCC, HC, random close/loose, and SC).

4.4.3 Summary

Analytical methods for application to the ETC of a medium with spherical inclusions were investigated in Toptan et al. (2021). Although the focus of that previous study was on the macroscopic description of thermal conductivity, the discussions and conclusions are similarly valid for diffusivity coefficients, due to their similar mathematical forms. In this study, we extended our research to examine the validity of models for the effective diffusivity calculations, obtained from the Fickian diffusion. Only the models we examined in our earlier study (Toptan et al., 2021) (i.e., D-EMT for $\alpha < 1$ and EMT for $\alpha < 1$) were considered in the present study. Each analytical model was evaluated with respect to the expected EDC obtained from the FEA simulations under a variety of conditions. In our analyses, the FEA simulations were performed under a packing fraction of up to approximately 40%. We observed similar behavior from each model in

regard to estimating the EDC of a binary system: D-EMT for $\alpha < 1$ and EMT for $\alpha > 1$, where α is defined as the ratio of the diffusivity coefficient of spheres over that of the host matrix. These numerical results establish the regimes in which these analytical formulations can be used with a high degree of confidence for the applications of interest, particularly for Fickian-diffusion-based EDC estimation for TRISO modeling applications. Both the EMT and D-EMT approaches, among many others detailed in Toptan et al. (2021), are available in the BISON code.

5. Verification

Since computational modeling and simulation tools are used to inform high-consequence decisions, it is important to verify that the computational results are reliable and predictive. Verification is a process to ensure that the code functions correctly and is reliable. Verification of BISON's solution with an exhaustive number of exercises can be found in previous studies by Hales et al. (81–90); Toptan et al. (2020c,b, 2022b, 2023). In this chapter, we exercise two types of verification exercises to verify BISON's computed solution: code and solution verification exercises. The *code verification* is a type of verification in which we focus on the correctness of the implemented numerical algorithm and the underlying mathematical model including partial differential or integral equations, initial and boundary conditions, etc. The *solution verification* is a type of verification in which we focus on the assessment of sources of numerical uncertainty, including round-off, statistical variation, iterative tolerances, and truncation error (Toptan et al., 2020c).

5.1 Convergence

The theoretical rate of convergence (or the formal order of accuracy) can be determined through an analysis of the linear truncation error (LTE). After we select the method to obtain solutions, the theoretical convergence rate of the numerical algorithm is established. Then, for the code verification exercise, a numerical representation of the mathematical model is formulated and solved on at least three consecutive meshes. Global errors between the numerical solutions and the reference solution are calculated using error norms. For example, the L_2-norm (or Euclidean norm) of the error over the solution domain Ω is defined as:

$$||u - \tilde{u}||_{L_2(\Omega)} = \left[\int_\Omega (u - \tilde{u})^2 d\Omega\right]^{1/2} \tag{5.1}$$

where the reference solution is represented by the primary variable u (temperature for heat conduction, concentration for mass diffusion solution, etc.) and the numerical approximation is $\tilde{u}$.

For the solution verification, the L_2-norm of the error over the solution domain between successive iterations is calculated using the following relation:

$$||\tilde{u}_{\text{refined}} - \tilde{u}_{\text{coarse}}||_{L_2(\Omega)} = \left[\int_\Omega (\tilde{u}_{\text{refined}} - \tilde{u}_{\text{coarse}})^2 d\Omega\right]^{1/2} \tag{5.2}$$

The local LTE converges at some rate; therefore, the global error will converge at the same rate if the mesh size is (1) small enough to eliminate higher-order LTE terms and (2) large enough to avoid numerical round-off error. To relate the error to the characteristic element size h, we use the following:

$$||u - \tilde{u}||_{L_2(\Omega)} = Ch^{\hat{p}} \tag{5.3a}$$

or

$$||\tilde{u}_{\text{refined}} - \tilde{u}_{\text{coarse}}||_{L_2(\Omega)} = Ch^{\hat{p}} \tag{5.3b}$$

where C is a problem-dependent constant, $||\cdot||$ indicates a norm, and $\hat{p}$ is the observed spatial order of accuracy. Using the L_2-norm, the expected order is $\hat{p}$ where $\hat{p}$ is two for the first-order or linear and three for the second-order or quadratic finite elements (FEs). Equation 5.3 is in a power law form; therefore, the slope on a log-log plot is:

$$\hat{p} = \frac{\log\left(||u||_{r_x h}\right) - \log\left(||u||_h\right)}{\log\left(r_x h\right) - \log\left(h\right)} \tag{5.4}$$

where $||q||_h$ is the norm of q at some mesh size (h) and r_x is the spatial mesh refinement factor ($r_x \geq 2$). Similarly, for the temporal observed order of accuracy, the slope on a log-log plot is computed according to:

$$\hat{q} = \frac{\log\left(||u||_{r_t \Delta t}\right) - \log\left(||u||_{\Delta t}\right)}{\log\left(r_t \Delta t\right) - \log\left(\Delta t\right)} \tag{5.5}$$

where $||u||_{\Delta t}$ is the norm of u at some time step (Δt) and r_t is the temporal mesh refinement factor ($r_t \geq 2$) and Δt is the time-step. Using the L_2-norm, the expected order is $\hat{q}$ where $\hat{q}$ is one for the first order (e.g., explicit/implicit Euler, explicit midpoint) and two for the second order (e.g., Crank-Nicolson, Newmark-beta) time integration schemes (Toptan et al., 2020c).

Figure 5.1 shows a pictorial representation of expected convergence behavior, which is characterized by three regions in practical applications (Toptan et al., 2020b): *Region I* represents coarse meshes, *Region II* is the asymptotic region, and *Region III* is caused by numerical error. The desirable region for the numerical solutions is the asymptotic region. Here, the convergence behavior is illustrated for the spatial refinement analysis where the error norm is plotted with respect to the mesh size and the slope is the spatial order p. Similarly, the convergence behavior can be obtained for the temporal refinement analysis where the error norm is plotted with respect to the time-step instead and the slope is the temporal order q.

The formal order of accuracy is derived in Toptan et al. (2020c) for both spatial and the temporal orders. To establish the spatial formal order of accuracy of an FE solution algorithm, we provide a heuristic derivation and point the reader to more mathematically rigorous analyses with the same result. In this work, the convergence of the computed solution to the analytical solution is analyzed as the size of the FE approaches zero (e.g., h-convergence). No effort is made to quantify p-convergence, in which convergence is analyzed as the order of the basis functions is increased.

After formulating the required mesh and input, a numerical representation of the problem is solved on at least three meshes. In this work, many meshes are evaluated to examine the behavior outside the

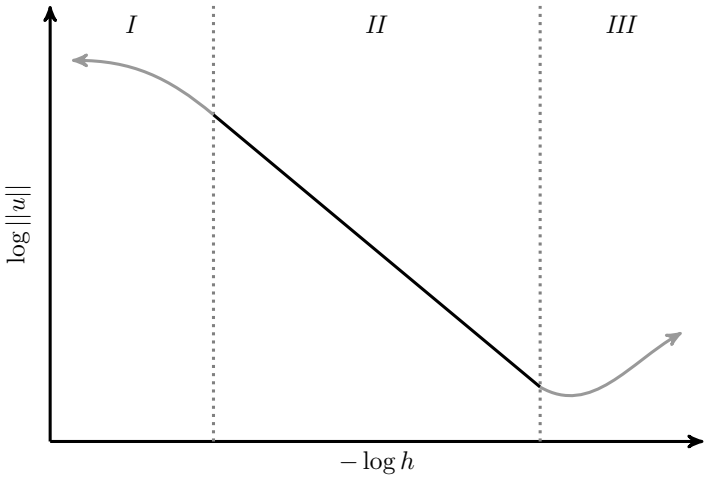

Figure 5.1. A pictorial representation of expected convergence behavior (Toptan et al., 2020c). *Region I* represents coarse meshes, *Region II* is the asymptotic region, and *Region III* is caused by numerical error.

asymptotic region. For steady state problems, only the spatial mesh is refined; both spatial and temporal refinement is employed simultaneously for transient problems. Such combined order analysis methodology has been introduced by Kamm et al. (2003-4041). In this analysis of the combined spatial and temporal convergence, we investigate both spatial and temporal aspects together. The main advantage of this method to cover issues related to the interaction between the spatial and temporal discretization (Oberkampf and Roy, 2010). Given the p-th order accurate in space and q-th order accurate in time, the temporal refinement factor can be selected—to obtain the corresponding expected reduction in error—according to:

$$r_t = (r_x)^{(p/q)} \tag{5.6}$$

for $p \neq q$ (Oberkampf and Roy, 2010). For example, we refine the time steps with $r_t = 4$ while refining the spatial mesh with $r_x = 2$, for a case using first-order FEs for the spatial mesh ($p = 2$) and the first-order time integration schemes ($q = 1$). Note that the above derivations make use of constant (or uniform) grid refinement.

Both code and solution verification exercises are successful if the observed order of accuracy matches the formal order of accuracy. This verification exercise provides confidence in the implemented numerical algorithm because it is supporting evidence that the numerical solution of this particular combination of physics, discretization, boundary/initial conditions, and geometry is mathematically correct.

5.2 Verification of BISON's Transient Heat Conduction Solution

The heat conduction equation is solved for $x \in [r_i, r_o]$ and $t \in (0, t_{\text{end}}]$ where r_i is the inner radius of the sphere, r_o is the outer radius of the sphere and t_{end} is the simulation end time. The Dirichlet boundary conditions of $u(r_i, t)$, $u(r_o, t)$ for $t \in (0, t_{\text{end}}]$ and the initial condition of $u(x, 0) = u_0$. A solid sphere has a spatially dependent internal heating:

$$q''' = q'''_o \frac{r_o}{r} \sin\left(\frac{\pi r}{r_o}\right) \tag{5.7}$$

and the resulting analytical solution for the temperature distribution is (Carslaw and Jaeger, 1959):

$$u(x,t) = u_0 + \frac{q'''_o r_o^3}{\pi^2 r k}\left[1 - \exp\left(-\frac{\pi^2 \alpha t}{r_o^2}\right)\right] \sin\left(\frac{\pi r}{r_o}\right) \tag{5.8}$$

where u_0 is the initial temperature, k is the thermal conductivity, and α is the thermal diffusivity.

The solution is solved with unity thermal properties and r_i, r_o are set to 0.1 and 1.0 in this analysis, respectively. Figure 5.2 shows the comparison of analytical and code predicted solutions for Equation 5.8 at various times, where second-order FEs are used. The top row shows the exact and computed solution for three different times. The second row indicates the difference between the computed solution and the exact solution. Finally, the results of a combined order analysis are shown in Figure 5.3, which was conducted with a spatial refinement factor of two ($r_x = 2$) that yields a temporal refinement factor of four ($r_t = 4$) for the linear elements and eight ($r_t = 8$) for the quadratic elements. The explicit Euler is chosen as the time integration scheme, which is a first-order scheme ($q = 1$). All results match with the expected behavior discussed previously. Norms are shown in the difference between the computed and exact solution for temperature. The formal orders of accuracy for all cases are derived in Toptan et al. (2020c). For linear FE, the formal spatial order is two. For quadratic FE, the formal spatial order is three. For first-order time-integration scheme, explicit Euler, the formal temporal order is one. In the asymptotic regions, all errors converge to the exact solution with the correct order of accuracy.

More verification exercises on the BISON steady-state/transient heat conduction solution can be found in Toptan et al. (2020c,b, 2022b).

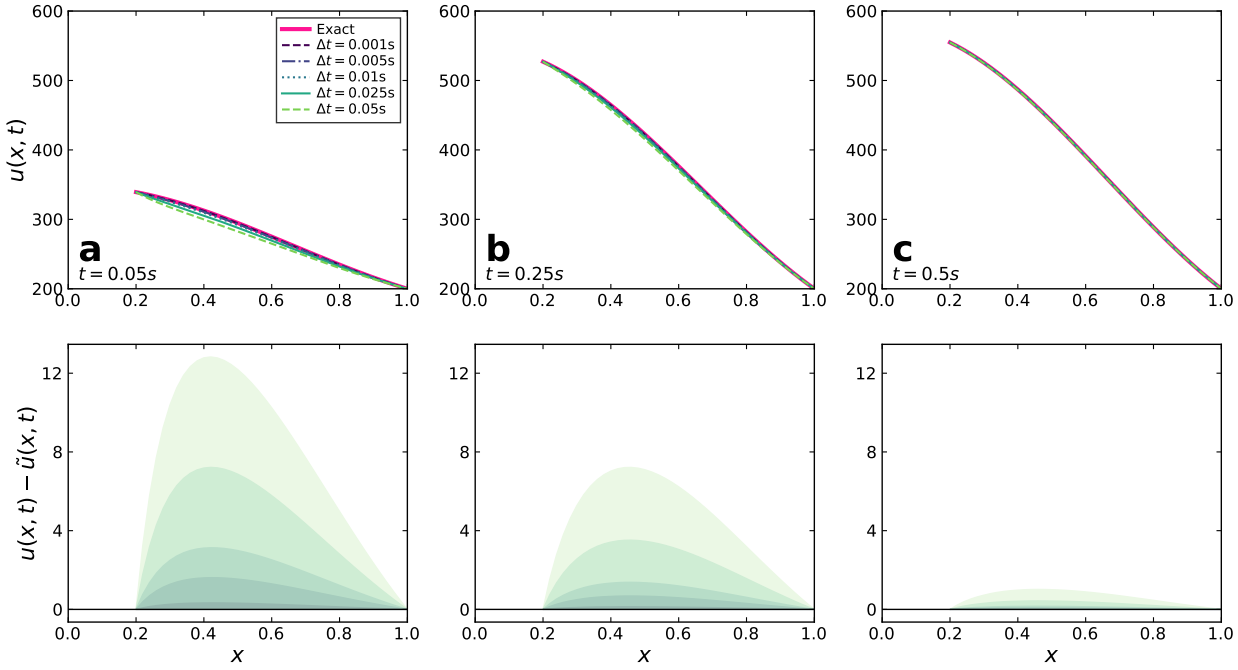

Figure 5.2. Exact and computed solutions for Equation 5.8 at **(a)** $t = 0.05$ s, **(b)** at $t = 0.25$ s, and **(c)** $t = 0.50$ s. *First row:* temperature distribution at a fixed spatial mesh ($N_{elem} = 64$) for various time-steps using quadratic one-dimensional FEs. *Second row:* difference between the exact and computed solutions.

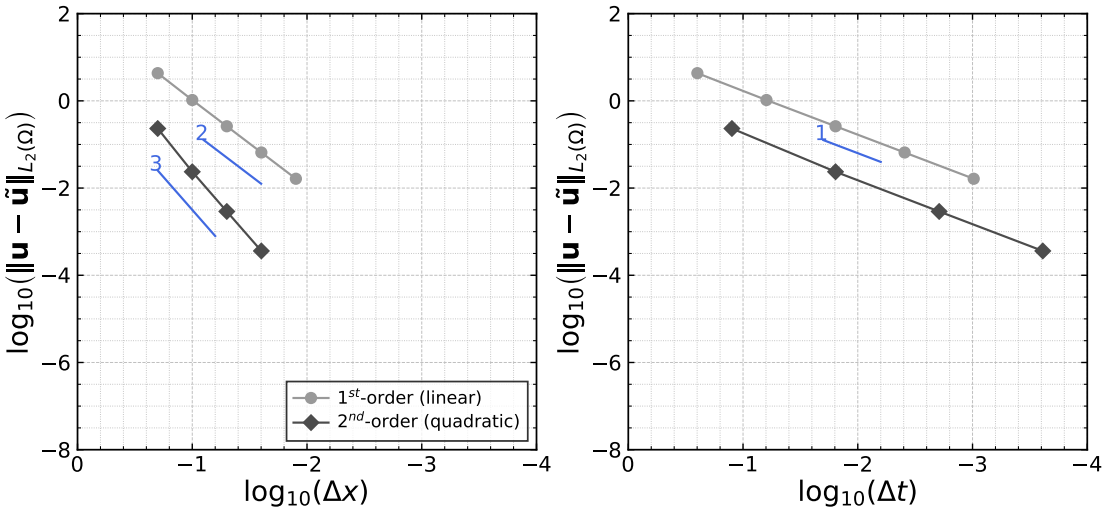

Figure 5.3. Combined spatial and temporal convergence plot for Equation 5.8. The L_2-norm quantifies convergence of temperature distribution which is evaluated at $t = 1.0$ s. Slopes of first-, second-, and third-order convergence are indicated.

5.3 Verification of BISON's Transient Mass Diffusion Solution

The mass diffusion equation is in the form of $u_t = u_{xx}$ for this specific analytical problem and is solved for $x \in [0, 1]$ and $t \in (0, t_{\text{end}}]$. The Dirichlet boundary conditions of $u(0, t) = u(1, t) = 0$ for $t \in (0, T]$ and the initial condition of $u(x, 0) = \sin(\pi x) + 0.1 \sin(100\pi x)$. The analytical solution for the problem is given by (mit):

$$u(x, t) = e^{-\pi^2 t} \sin(\pi x) + 0.1 e^{-\pi^2 10^4 t} \sin(100\pi x) \tag{5.9}$$

The solution is solved with unity diffusivity coefficient. Figure 5.4 shows the comparison of analytical and code predicted solutions for Equation 5.9 at various times, where second-order FEs are used. Similar to the previous study, the top row shows the exact and computed solution for three different time. The second row indicates the difference between the computed solution and the exact solution. The computed solution undergoes rapid oscillations (or damping) in space due to $\sin(100\pi x)$ in Equation 5.9. The amplitude of rapid oscillations disappear as time increases, becomes invisible around 0.5 seconds. Finally, Figure 5.3 shows results from the conducted combined spatial and temporal analysis in which a temporal refinement factor of four ($r_t = 2$) for the linear elements and eight ($r_t = \sqrt{8}$) for the quadratic elements for a spatial refinement factor of two ($r_x = 2$) and a second-order time integration scheme of diagonally implicit Runge-Kutta (DIRK) ($q = 2$). All results match with the expected behavior discussed previously. Norms are shown in the difference between the computed and exact solution for temperature. For linear FE, the formal spatial order is two. For quadratic FE, the formal spatial order is three. For second-order time-integration scheme, DIRK, the formal temporal order is two. In the asymptotic regions, all errors converge to the exact solution with the correct order of accuracy.

More verification exercises on the BISON steady-state/transient mass diffusion solution can be found in Toptan et al. (2023).

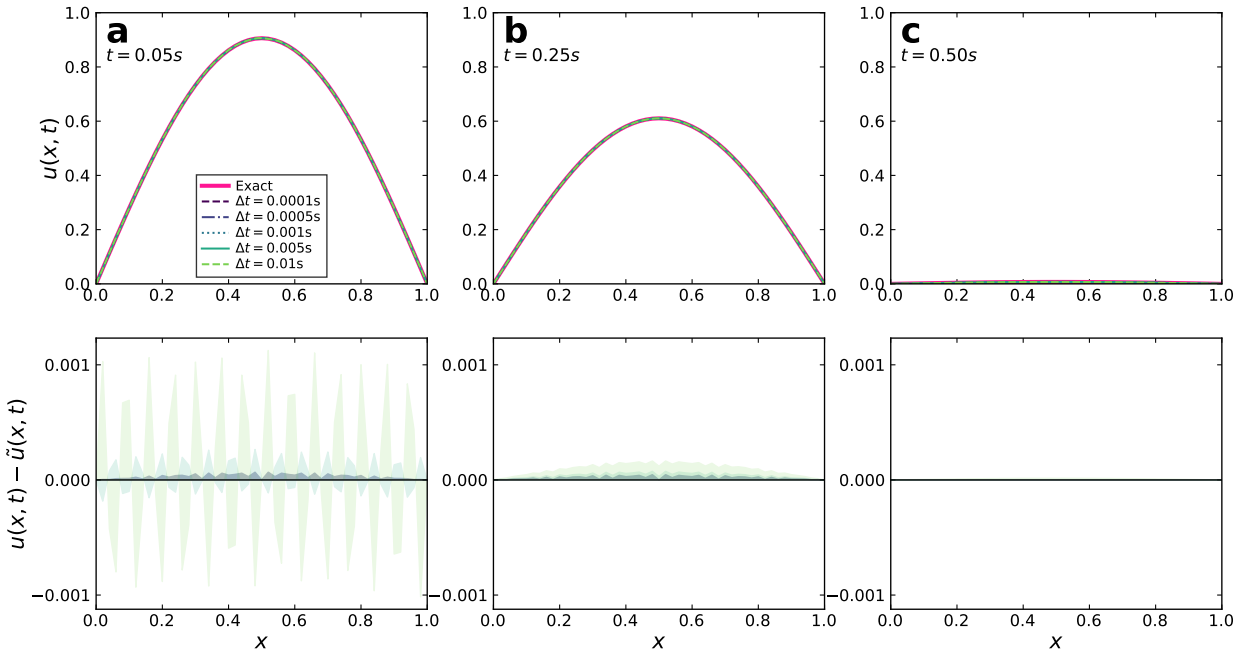

Figure 5.4. Exact and computed solutions for Equation 5.9 at **(a)** $t = 0.05$ s, **(b)** at $t = 0.25$ s, and **(c)** $t = 0.50$ s. *First row:* concentration distribution at a fixed spatial mesh ($N_{elem} = 64$) for various time-steps using quadratic one-dimensional FEs. *Second row:* difference between the exact and computed solutions.

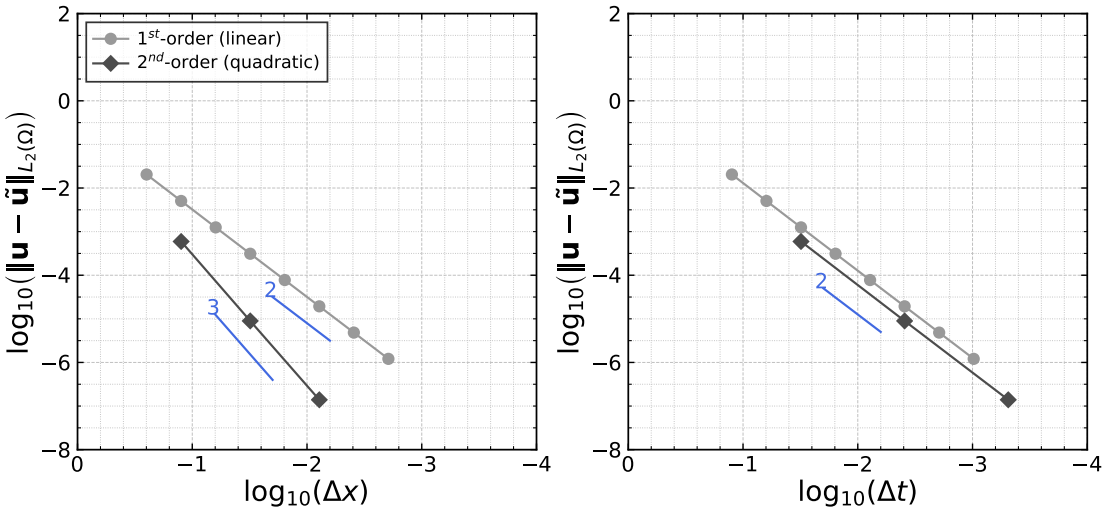

Figure 5.5. Combined spatial and temporal convergence plot for Equation 5.8. The L_2-norm quantifies convergence of concentration distribution which is evaluated at $t = 0.25$ s. Slopes of second-, and third-order convergence are indicated.

5.4 Verification of BISON's Fission Product Species Conservation Under TRISO Reactor Conditions

Recent work has focused on verification of the partial differential equation (PDE) governing the conservation of fission product species (i.e., Equation 5.10), particularly its predictions under spatiotemporal reactor conditions for a TRISO particle. This study covers a set of numerical experiments examining BISON's predictive capability concerning the conservation of fission product species (or the mass diffusion solution) under various in-pile and out-of-pile conditions. The verification exercises were chosen for their relevance to spherical TRISO particles for both short- and long-lived (i.e., stable) fission product species. *The material presented here is a subset of the information found in Toptan et al. (2023).*

5.4.1 Background

Fission product species conservation (i.e., mass diffusion or Fick's second law) is given by:

$$\frac{\partial C}{\partial t} + \nabla \cdot \mathbf{J} + \lambda C - p = 0, \tag{5.10}$$

where C is the concentration, λ is the decay constant ($\lambda = \frac{\ln(2)}{T_{1/2}}$ in terms of the half-life $T_{1/2}$), p is the source rate of a given species, and $\mathbf{J}$ is the mass flux. With neglected radioactive decay, heat conduction and Equation 5.10 become similar PDEs.

The PDE concerning the conservation of fission product species, Equation 5.10 is composed of terms for transient effects, diffusion, decay, and the volumetric source rate. We use the same convention throughout this study, with the additional following symbols and dimensionless numbers:

- a is the radius of the sphere,
- $\rho = r/a$ is the dimensionless normalized radius ($0 \leq \rho \leq 1$),
- $\tau = D't$ is the dimensionless diffusion time (-),
- $D' = D/a^2$ is the reduced diffusion coefficient (s^{-1}), and
- $\mu = \lambda/D'$ is the ratio of the decay rate to its diffusion rate (-).

For short-lived isotopes, $\mu \gg 1$; for long-lived isotopes, $\mu \ll 1$; and for a stable isotope, $\mu = 0$.

In all cases, the sphere of radius a is subject to similar boundary and initial conditions. Radial symmetry is considered at the origin ($r = 0$) for all $t \geq 0$. The concentration is set to zero at the outer surface ($r = a$), and at $r = a$ for all $t \geq 0$, a Dirichlet boundary condition is applied as $C = \hat{C}$ on Γ_C, where $\hat{C}$ is a prescribed value for concentration ($\hat{C} = 0$ to remain concentration-free, or for the ideal sink in this study) and Γ_C is the boundary on which it is applied. A constant (or flat) profile is applied as the initial concentration profile: $C(\mathbf{x}, t) = \hat{C}_0$ at $t = 0$ for $0 \leq r \leq a$, where $\hat{C}_0$ is the prescribed initial concentration.

In this study, the following three main verification exercises concerning the reactor conditions for spherical TRISO particles were selected:

1. In-pile production, transport, and decay of short-lived isotopes ($\lambda \neq 0$), where the spherical particle is initially concentration-free ($\hat{C}_0 = 0$) and a non-zero source term is applied ($p \neq 0$). See Section 5.4.2.
2. In-pile production, transport, and decay of long-lived (or stable) isotopes ($\lambda \equiv 0$), where the spherical particle is initially free of concentration-free ($\hat{C}_0 = 0$) and a non-zero source term is applied ($p \neq 0$; see Section 5.4.3.)
3. Out-of-pile conditions for transport and decay of pre-existing isotopes ($\lambda \neq 0$), where the spherical particle is initially at a non-zero concentration ($C_0 \neq 0$), and no production ($p = 0$) occurs within the particle, see Section 5.4.4.

The analytical solutions to this PDE under these conditions were taken from Nabielek et al. (1974). In an attempt to better understand the physics by applying a reduced number of variables, these expressions are nondimensionalized in this study. The BISON-computed results were compared against the expected results obtained from the analytical expressions in terms of the following QoIs:

1. The *concentration*, $C(r,t)$, was obtained from Equation 5.10, based on the problem settings (e.g., initial/boundary conditions and geometry). For constant D and p, Equation 5.10 in spherical coordinates reduces to:
$$\frac{\partial C}{\partial t} = \frac{1}{r}\frac{\partial^2}{\partial r^2}(rC) - \lambda C + p. \tag{5.11}$$
2. The *release rate*, $R(t)$, is given as the product of the flux to the outside and the surface area of the sphere ($4\pi a^2$):
$$R(t) = -4\pi a^2 D \left.\frac{\partial C}{\partial r}\right|_{r=a}. \tag{5.12}$$
The ratio of the release rate to the production rate over the whole volume of the sphere ($\frac{4}{3}\pi a^3$) is referred to as the *release-rate over birth-rate (R/B)* (-), and is expressed as:
$$(R/B) = \frac{R(t)}{\frac{4}{3}\pi a^3 p(t)}. \tag{5.13}$$
The R/B ratio can also be thought of as the fractional release rate. This ratio is the non-dimensional correspondence of the release rate and is only meaningful for in-pile conditions.
3. The *fractional release (i.e., release fraction)*, $F(t)$ (-) is defined as the ratio of the number of undecayed atoms outside the sphere to the number of undecayed atoms in the whole system. For a constant production rate (i.e., $p(t) = p$), the above relation reduces to:
$$F(t) = \frac{\int_0^t R(t')e^{\lambda t}dt'}{\frac{4}{3}\pi a^3\left\{C_0 + \frac{p}{\lambda}\left[e^{\lambda t} - 1\right]\right\}}. \tag{5.14}$$

5.4.2 Exercise 1: In-pile production, transport, and decay of short-lived isotopes ($C_0 = 0$, $p \neq 0$, and $\lambda \neq 0$)

The in-pile conditions for a decaying fission product ($\lambda \neq 0$) are considered in terms of the following settings: an initial concentration of zero in the sphere ($C_0 = 0$ for $0 \leq r \leq a$), and a non-zero source ($p \neq 0$). In this study, we assume constant source generation, $p(t) = p$. Equation 5.10 is solved in the spherical coordinates. For the in-pile production, transport, and decay of short-lived isotopes, the resulting analytical expressions for the concentration, R/B, and fractional release are as follows:

1. The concentration profile, $C(\rho, \tau)$, is expressed as:

$$\frac{C(\rho,\tau)}{p/\lambda} = \frac{2\mu}{\pi\rho}\sum_{n=1}^{\infty}(-1)^{n+1}\frac{1-e^{-(n^2\pi^2+\mu)\tau}}{n\left(n^2\pi^2+\mu\right)}\sin\left(n\pi\rho\right), \tag{5.15a}$$

   and as $\tau \to \infty$, Equation 5.15a reduces to:

$$\frac{C_\infty}{p/\lambda} = 1 - \frac{\sinh\left(\rho\sqrt{\mu}\right)}{\rho\sinh\left(\sqrt{\mu}\right)}. \tag{5.15b}$$

2. The R/B ratio is expressed as:

$$(R/B) = \frac{3}{\sqrt{\mu}}\left(\coth\left(\sqrt{\mu}\right) - \frac{1}{\sqrt{\mu}}\right) - 6\sum_{n=1}^{\infty}\frac{e^{-(n^2\pi^2+\mu)\tau}}{n^2\pi^2+\mu}. \tag{5.16}$$

   Equation 5.16 reduces to the first term on the right-hand side (RHS) of this relation as $\tau \to \infty$.

3. The fractional release, $F(\tau)$, is expressed as:

$$F(\tau) = \frac{3}{\sqrt{\mu}}\left(\coth\left(\sqrt{\mu}\right) - \frac{1}{\sqrt{\mu}}\right) - \frac{6\mu}{e^{\mu\tau}-1}\sum_{n=1}^{\infty}\frac{1-e^{-n^2\pi^2\tau}}{n^2\pi^2\left(n^2\pi^2+\mu\right)}. \tag{5.17}$$

Figure 5.6 compares the analytical and the computed concentration, $C/(p/\lambda)$, at four different radial locations (ρ = 0.25, 0.50, 0.75, and 0.95); R/B; and $F(\tau)$ as a function of dimensionless diffusion time, τ (with arbitrarily chosen $\mu = 0.1$). In this exercise, the first 100,000 terms in the infinite summation are considered sufficient to prevent any artificial oscillations in the analytical solution. The BISON predictions agree well with the analytical results for the concentration profiles, R/B ratio, and fractional release from a solid sphere under in-pile conditions for a decaying fission product.

5.4.3 Exercise 2: In-pile production and transport of a stable fission product ($C_0 = 0$, $p \neq 0$, and $\lambda = 0$)

The in-pile conditions for a stable fission product ($\lambda = 0$) are considered in terms of the following settings: an initial concentration of zero in the sphere ($C_0 = 0$ for $0 \leq r \leq a$), and a non-zero source ($p \neq 0$). In this study, we assume constant source generation, $p(t) = p$. Equation 5.10 is solved in the spherical coordinates.

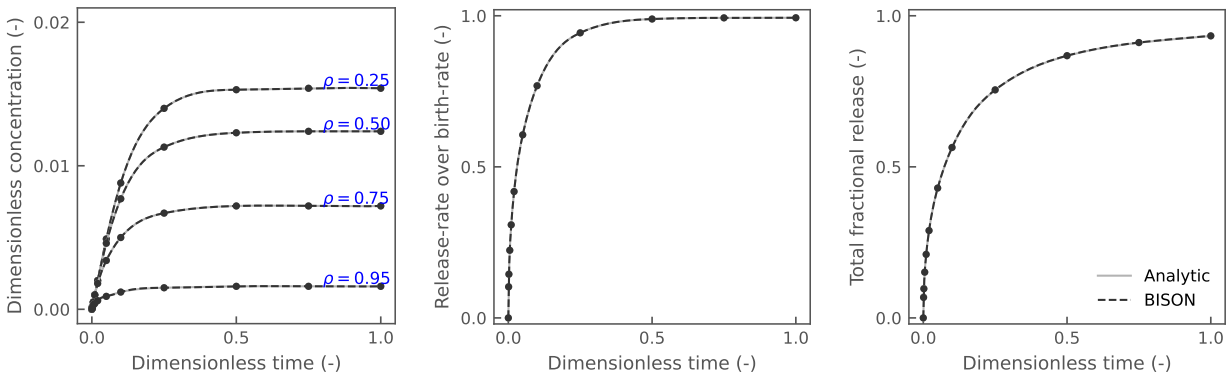

(a) $C/(p/\lambda)$ vs. τ (b) (R/B) vs. τ (c) $F(\tau)$ vs. τ

Figure 5.6. Comparison of the analytical and the computed (a) concentration, $C/(p/\lambda)$, at four different radial locations ($\rho = 0.25$, 0.50, 0.75, and 0.95); (b) the release rate over the birth rate, (R/B); and the (c) fractional release, $F(\tau)$, as a function of dimensionless diffusion time, τ (with arbitrarily chosen $\mu = 0.1$), for in-pile production, transport, and decay of short-lived isotopes ($C_0 = 0$, $p \neq 0$, and $\lambda \neq 0$).

For the in-pile production and transport of a stable fission product, the resulting analytical expressions for the concentration, R/B, and fractional release are as follows:

1. The concentration profile, $C(\rho, \tau)$ is expressed as:

$$\frac{C(\rho,\tau)}{p/6D'} = (1-\rho^2) - \frac{12}{\rho}\sum_{n=1}^{\infty}(-1)^{n+1}\frac{e^{-n^2\pi^2\tau}}{n^3\pi^3}\sin(n\pi\rho). \tag{5.18}$$

   The steady-state ($\tau \to \infty$) solution for the concentration reduces to the first term on the RHS of Equation 5.18.

2. The R/B ratio is expressed as:

$$(R/B) = 1 - 6\sum_{n=1}^{\infty}\frac{e^{-n^2\pi^2\tau}}{n^2\pi^2}. \tag{5.19}$$

3. The fractional release, $F(t)$, is expressed as:

$$F(\tau) = 1 - \frac{6}{\tau}\sum_{n=1}^{\infty}\frac{1-e^{-n^2\pi^2\tau}}{n^4\pi^4}. \tag{5.20}$$

Figure 5.7 compares the analytical and the computed concentration, $C(\rho,\tau)/\left[p/(6D')\right]$, at four different radial locations ($\rho = 0.25$, 0.50, 0.75, and 0.95); R/B; and $F(\tau)$ as a function of τ (with arbitrarily chosen $\mu = 0.1$; however, the concentration solution is independent of μ). In this exercise, the first 100,000 terms in the infinite summation are considered sufficient to prevent any artificial oscillations in the analytical solution. The BISON predictions agree well with the analytical results for the concentration profiles, R/B ratio, and fractional release from a solid sphere under in-pile conditions for a stable fission product.

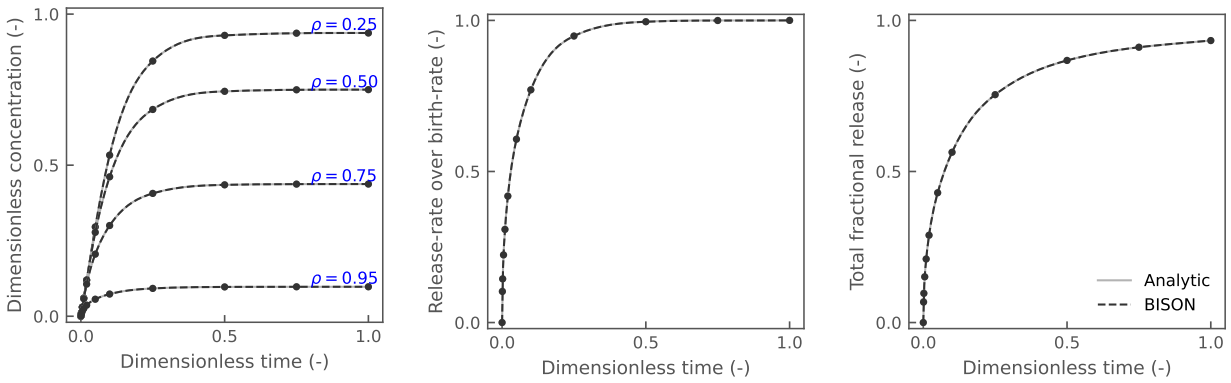

(a) $\frac{C(\rho,\tau)}{p/6D'}$ vs. τ (b) (R/B) vs. τ (c) $F(\tau)$ vs. τ

Figure 5.7. Comparison of the analytical and the computed (a) concentration, $C(\rho,\tau)/\left[p/(6D')\right]$, at four different radial locations ($\rho = 0.25$, 0.50, 0.75, and 0.95); (b) release rate over birth rate, (R/B); and (c) fractional release, $F(\tau)$, as a function of dimensionless diffusion time, τ (with arbitrarily chosen $\mu = 0.1$; however, the concentration solution is independent of μ) for in-pile production and transport of a stable fission product ($C_0 = 0$, $p \neq 0$, and $\lambda = 0$).

5.4.4 Exercise 3: Out-of-pile conditions for the transport and decay of preexisting isotopes ($C_0 \neq 0$, $p = 0$, and $\lambda \neq 0$)

The out-of-pile conditions for a decaying fission product ($\lambda \neq 0$) are considered in terms of the following settings: an initial concentration of non-zero in the sphere ($C_0 \neq 0$ for $0 \leq r \leq a$), and a zero source ($p = 0$). Equation 5.10 is solved in the spherical coordinates. For out-of-pile conditions for the transport and decay of preexisting isotopes, the resulting analytical expressions for the concentration, release rate, and fractional release are as follows:

1. The concentration profile, $C(\rho,\tau)$, is expressed as:

$$\frac{C(\rho,\tau)}{C_0} = \frac{2}{\rho}\sum_{n=1}^{\infty}(-1)^{n+1}\frac{e^{-\left(n^2\pi^2+\mu\right)\tau}}{n\pi}\sin\left(n\pi\rho\right). \tag{5.21}$$

2. The out-of-pile release rate, $R(\tau)$, is expressed as:

$$R(\tau) = 8\pi a^3\frac{C_0\lambda}{\mu}\sum_{n=1}^{\infty}e^{-\left(n^2\pi^2+\mu\right)\tau}. \tag{5.22}$$

3. The fractional release, $F(\tau)$, is expressed as:

$$F(\tau) = 1 - 6\sum_{n=1}^{\infty}\frac{e^{-n^2\pi^2\tau}}{n^2\pi^2}. \tag{5.23}$$

Figure 5.8 compares the analytical and the computed concentration, C/C_0, at four different radial locations ($\rho = 0.25$, 0.50, 0.75, and 0.95); $R(\tau)$; and $F(\tau)$ as a function of τ (with arbitrarily chosen $\mu = 0.1$). Note that, as the R/B definition is not meaningful in regard to out-of-pile conditions, we use the out-of-pile release rate $R(\tau)$. As $\tau \to \infty$, the dimensionless concentration approaches zero. In this exercise, the first 100,000 terms in the infinite summation are considered sufficient to prevent any artificial oscillations in the analytical solution. The BISON predictions agree well with the analytical results for concentration profiles, release rate, and fractional release from a solid sphere under out-of-pile conditions for the transport and decay of preexisting isotopes.

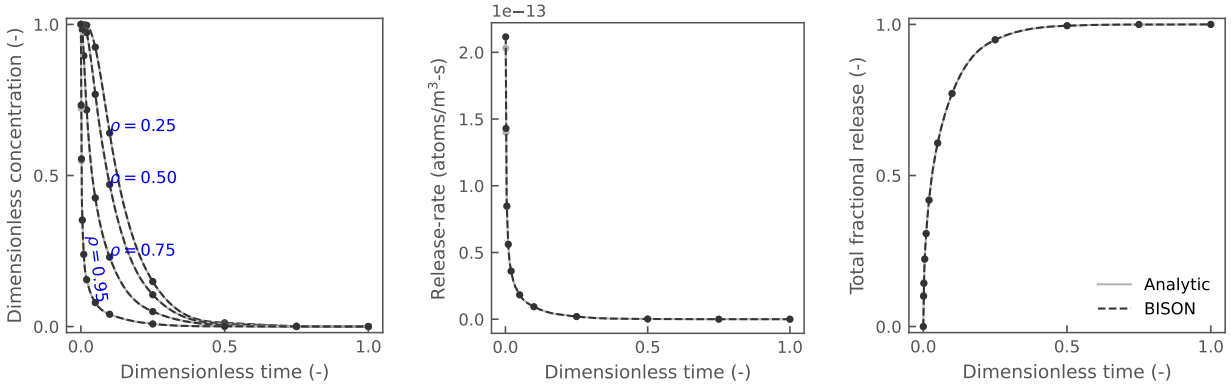

(a) $C/(p/\lambda)$ vs. τ (b) $R(\tau)$ vs. τ (c) $F(\tau)$ vs. τ

Figure 5.8. Comparison of the analytical and the computed (a) concentration, C/C_0, at four different radial locations ($\rho = 0.25$, 0.50, 0.75, and 0.95); (b) release rate, $R(\tau)$; and (c) fractional release, $F(\tau)$, as a function of dimensionless diffusion time, τ (with arbitrarily chosen $\mu = 0.1$) for out-of-pile conditions for the transport and decay of preexisting isotopes ($C_0 \neq 0$, $p = 0$, and $\lambda \neq 0$).

5.5 Verification of BISON's Mechanics Solution

This code verification problem is from Toptan et al. (2020c) where a thick-walled cylinder is subjected to a uniform radial internal pressure, q and a traction-free external pressure Young and Budynas (2002); Zienkiewicz et al. (2013). For the axisymmetric one-dimensional problem in which no rigid body modes exist. No essential displacement boundary conditions are necessary. Ignored temperature and inertia effects. The normal stresses in the longitudinal, circumferential, and radial directions are respectively denoted as σ_1, σ_2, and σ_3:

$$\sigma_1 = \frac{-qb^2\left(a^2 - r^2\right)}{r^2\left(a^2 - b^2\right)}, \qquad \sigma_2 = 0, \qquad \sigma_3 = \frac{qb^2\left(a^2 + r^2\right)}{r^2\left(a^2 - b^2\right)} \tag{5.24}$$

where a is the outer radius and b is the inner radius ($a < b$), r is the radius, q is the force per unit area.

The axisymmetric elasticity problem. Let us consider an infinitely long cylinder in which the displacement field is given by $u(r, z) = u(r)$ and $v(r, z) = 0$ (Zienkiewicz et al., 2013, pp.73–74). The non-zero strains are $\boldsymbol{\varepsilon} = \{\varepsilon_r, \varepsilon_\theta\} = \left\{\frac{\partial u}{\partial r}, \frac{u}{r}\right\}$. The equilibrium equation simplifies to the following form:

$$\frac{\partial \sigma_r}{\partial r} + \frac{\sigma_r - \sigma_\theta}{r} + b_r = \rho \frac{\partial^2 u}{\partial t^2}. \tag{5.25}$$

For an isotropic material, stress-strain relations—including temperature effects—are given by:

$$\begin{pmatrix} \sigma_r \\ \sigma_\theta \end{pmatrix} = \frac{E}{(1+\nu)(1-2\nu)} \begin{bmatrix} (1-\nu) & \nu \\ \nu & (1-\nu) \end{bmatrix} \begin{pmatrix} \varepsilon_r - \alpha\Delta T \\ \varepsilon_\theta - \alpha\Delta T \end{pmatrix} \tag{5.26}$$

and:

$$\sigma_z = \nu(\sigma_r + \sigma_\theta) - E\alpha\Delta T \tag{5.27}$$

where E is Young's modulus and ν is Poisson's ratio.

The problem domain is defined in $\boldsymbol{X} \in [0.5, 1.0]$. A Dirichlet boundary conditions is applied to the bottom boundary and the left boundary is a pressure boundary. Young's modulus is $E = 10\,000\,\mathrm{N/m^2}$ and Poisson's ratio is $\nu = 0.3$. Figure 5.9 shows the exact solution and FE solutions of the axisymmetric problem. The results are shown with 32 x 32 elements for each 2-D element type.

The analytical solution exists for the stresses; however, the primary variable is displacement. Therefore, the expected convergence behavior of the displacement cannot be captured through the use of a code verification study. Instead, *solution verification* is performed and the results are shown in Figure 5.10. Norms are calculated by comparing successively refined solutions at the inner surface of the cylinder.

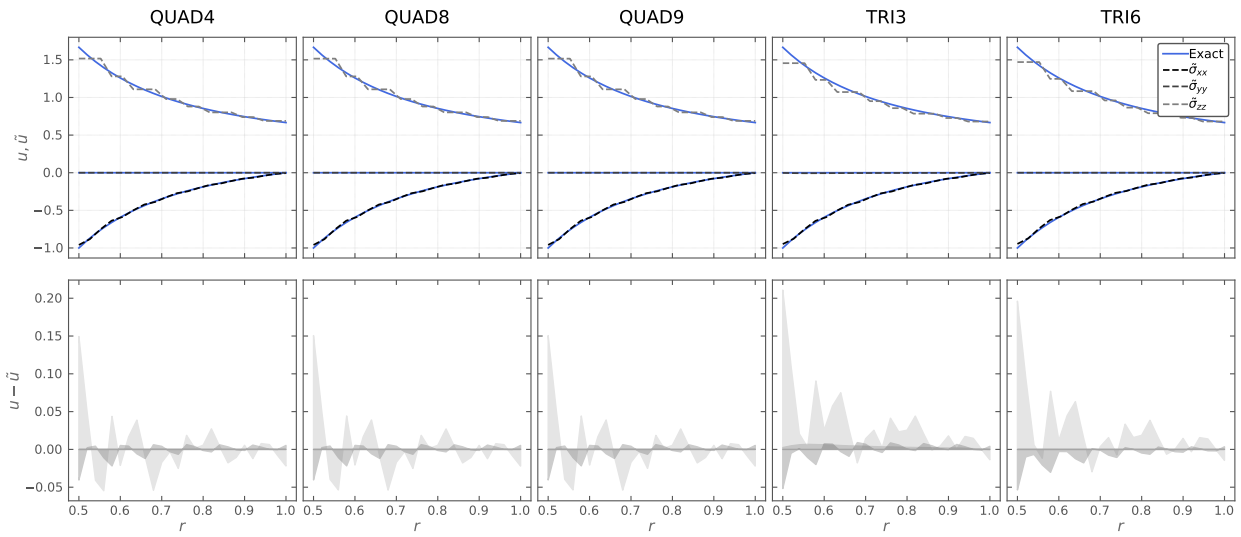

Figure 5.9. Exact and FE solutions for Equation 5.24. Results are shown for a single a 32 x 32 mesh for five different types of FE. *First row*: exact and FE solutions using 2-D elements for one-dimensional FE solution of stresses. *Second row*: residuals between the exact solution and the FE solutions.

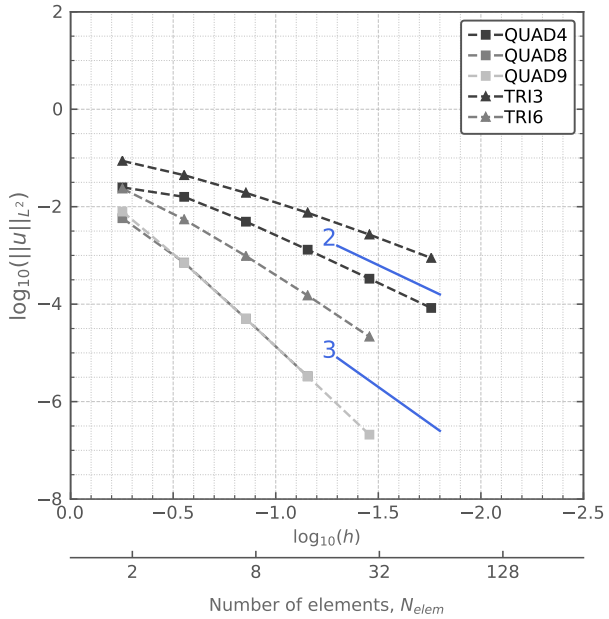

Figure 5.10. Spatial refinement analysis for Equation 5.24. Solution verification at the inner surface for displacement solution of the axisymmetric problem. Errors are quantified in terms of the L_2 norm.

5.6 Solution Verification of BISON's AGR-2 Results

The solution verification is a good exercise for real-world applications to verify the numerical solution, particularly in the absence of any analytical solutions. Here, we examine the convergence behavior of BISON's predictions for the AGR-2 validation to establish more confidence on the computed solution and eliminate numerical uncertainties in the simulation process. We selected a compact out of whole AGR-2 data sets to exercise the solution verification; AGR-2 Compact 6-2-1 as a demonstration in this study.

Figure 5.11 and Figure 5.12 show computed concentration and temperature predictions for 1-D linear and quadratic FEs, respectively. Here, we plotted the primary variables solved out of the four partial diffusion equations considered in the numerical simulation; silver, cesium, and strontium concentrations (C_{Ag}, C_{Cs}, and C_{Sr}) from the mass diffusion solutions for each fission product (FP) species, and temperature (T) from the heat conduction solution. In each plot, dashed lines represent the regions of the TRISO particle; (from left to right) fuel kernel, buffer, IPyC, SiC, and OPyC layers, respectively. Except for C_{Sr}, the solutions for C_{Ag}, C_{Cs}, and T instantaneously converge to the expected solution with a few elements (e.g., $N_{elems} = 4$). Due to the Sr diffusion characteristics, more elements are required for C_{Sr} converge to the expected behavior. As mentioned previously, the convergence behavior of uniform grid refinement is considered in this analysis to compute the observed orders of accuracy. However, we also plotted the computational results that employ the code's biased meshing capability, which is referred to as the baseline on the plots. The biased mesh capability allows to obtain converged behavior with a few number of fuel elements once true settings are established, which can particularly be useful for C_{Sr} calculations. For example, the converged C_{Sr} result is obtained with the uniform meshing using $N_{elems} \geq 128$ in the fuel kernel, while $N_{elems} = 20$ using the biased meshing towards the kernel–buffer region. Both uniform grid meshing and biased meshing can be useful once they are both utilized together to determine true grid settings for the converged solution with the biased meshing to benefit from the computational time in practical applications.

Figure 5.13 shows the conducted spatial refinement analysis with a spatial refinement factor of two ($r_x = 2$) at a fixed time-step. All results match with the expected behavior discussed previously. Norms are calculated by comparing successively refined solutions for C_{Ag}, C_{Cs}, C_{Sr}, and T. For linear FE, the formal spatial order is two. For quadratic FE, the formal spatial order is three. In the asymptotic regions, all errors converge with the correct order of accuracy. As observed in previous two plots, the C_{Ag}, C_{Cs}, and T solutions converge with the correct order of accuracy using a few number of elements. For example, the errors for C_{Ag} and C_{Cs} vary between 10^0 and 10^{-4} using coarse mesh sizes, $h \sim 10^{-4}$–10^{-5} m. Similarly for T, the errors locate in the range of 10^{-1} to 10^{-8} for the same mesh sizes. On the other hand, the computed solution for C_{Sr} converge with the correct order of accuracy for finer mesh sizes $h \sim 10^{-5}$–10^{-7} m for the linear FEs and $h \sim 10^{-5.5}$–10^{-6} m for the quadratic FEs. With quadratic elements, numerical error begins to pollute the solution when the mesh is refined greatly. This is a common occurrence with very fine meshes, which corresponds to Region III in Figure 5.1.

The code user can apply different grid refinement strategies (i.e., grid refinement in all regions simultaneously or having same mesh sizes in each region). In this exercise, the grid refinement is only performed for

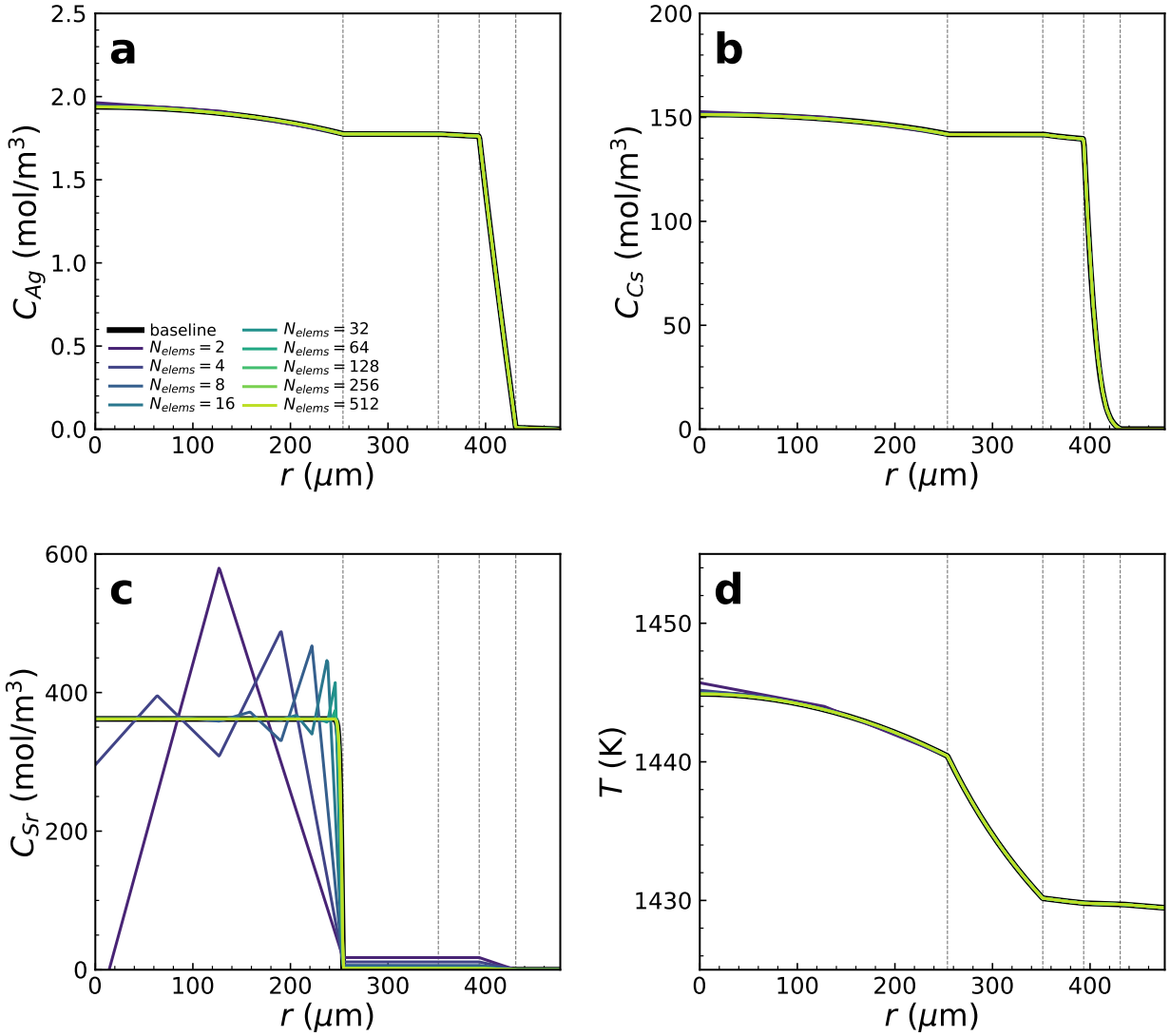

Figure 5.11. Computed solutions for the AGR-2 Compact 6-2-1 at the end of simulation time for (a) C_{Ag}, (b) C_{Cs}, (c) C_{Sr}, and (d) T, using one-dimensional linear elements. Baseline refers to the biased grid exercised in the validation exercise. The rest refers to the computed solution at various number of elements (N_{elem}) in the constant grid refinement study. The dashed lines represent the regions of TRISO particle; (from left to right) fuel kernel, buffer, IPyC, SiC, and OPyC layers, respectively.

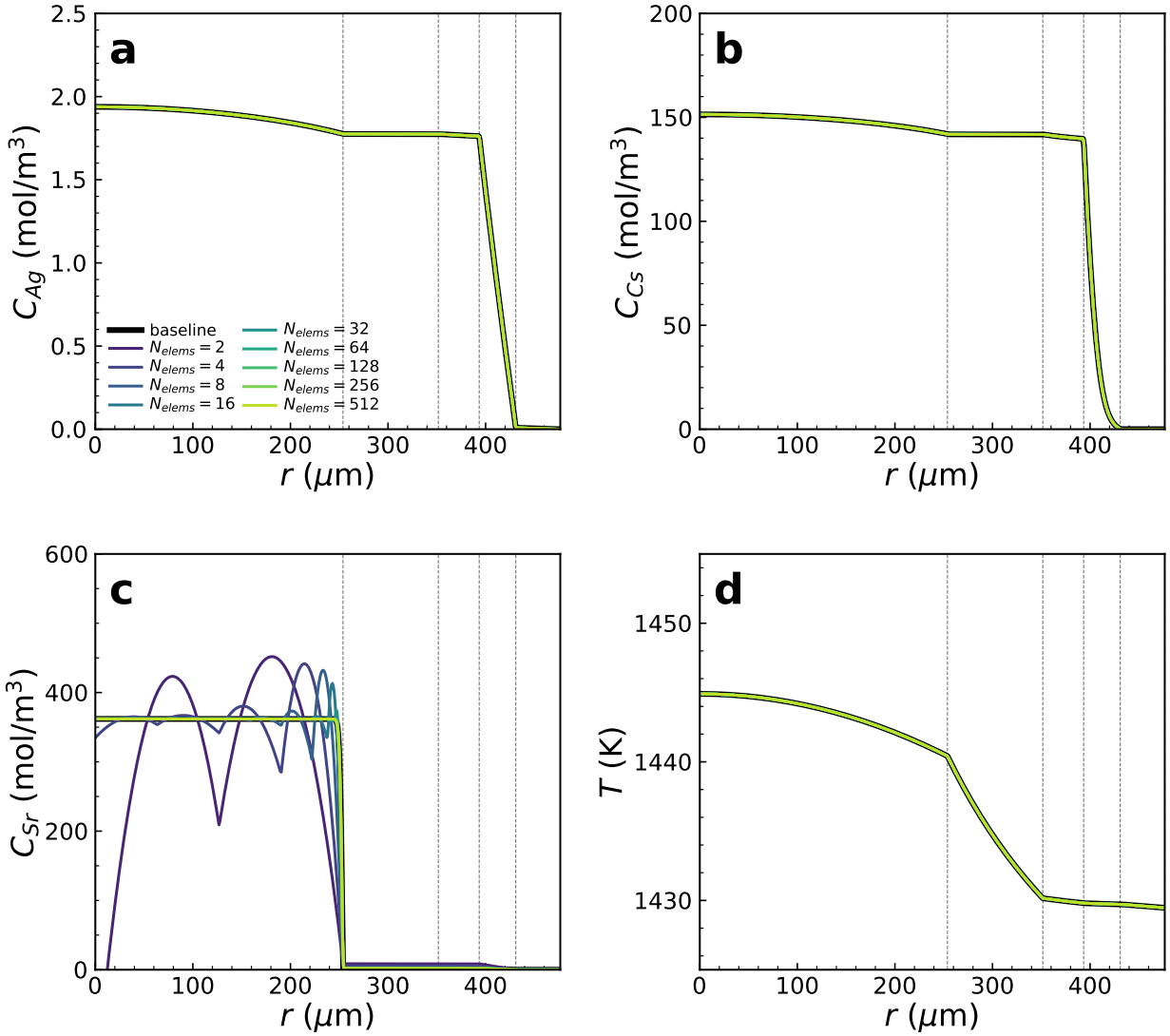

Figure 5.12. Computed solutions for the AGR-2 Compact 6-2-1 at the end of simulation time for (a) C_{Ag}, (b) C_{Cs}, (c) C_{Sr}, and (d) T, using one-dimensional quadratic elements. Baseline refers to the biased grid exercised in the validation exercise. The rest refers to the computed solution at various number of elements (N_{elem}) in the constant grid refinement study. The dashed lines represent the regions of TRISO particle; (from left to right) fuel kernel, buffer, IPyC, SiC, and OPyC layers, respectively.

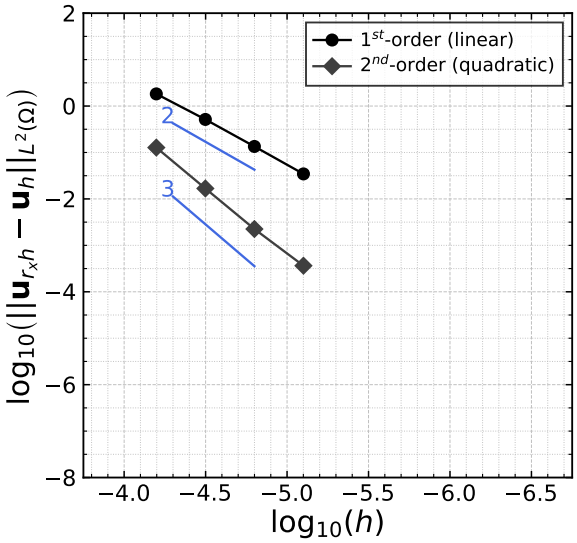

(a) Ag concentration, C_{Ag}, where $\mathbf{u} = \mathbf{C_{Ag}}$

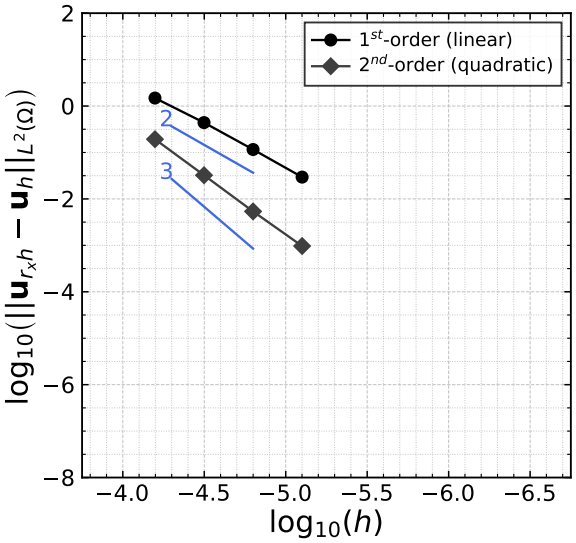

(b) Cs concentration, C_{Cs}, where $\mathbf{u} = \mathbf{C_{Cs}}$

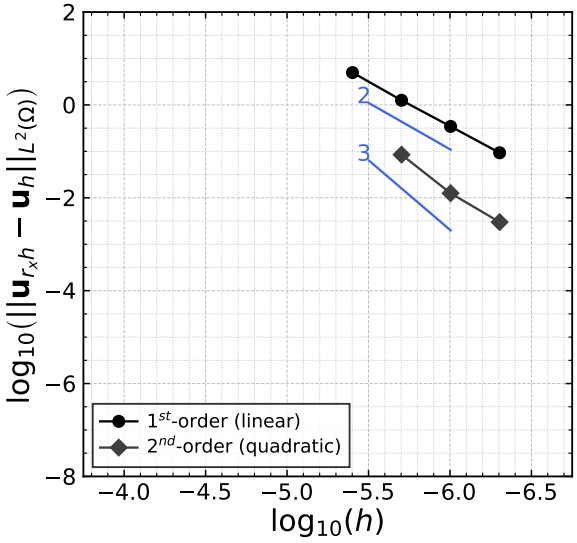

(c) Sr concentration, C_{Sr}, where $\mathbf{u} = \mathbf{C_{Sr}}$

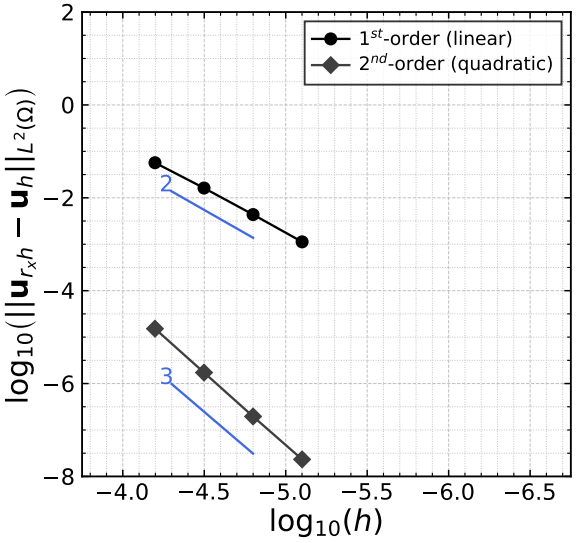

(d) Temperature, T, where $\mathbf{u} = \mathbf{T}$

Figure 5.13. Solution verification exercise for the AGR-2 Compact 6-2-1 with a constant grid refinement in the fuel kernel. The L_2-norm quantifies convergence of (a) C_{Ag}, (b) C_{Cs}, (c) C_{Sr}, and (d) T solutions. Slopes of second-, and third-order convergence are indicated.

the fuel kernel region since a sharp gradient is observed in the output quantity of interest (see Figure 5.11 and Figure 5.12 for the strontium concentration). However, the methodology can be applied to many different refinement strategies and the user can gather insights on the quality of mesh based on their application. In brief, we demonstrated here how the solution verification exercises are applied to the real-world application and we verified our computed solution before performing the validation exercises for AGR-2.

6. AGR-1 & AGR-2 Validation

Validation is the software development process for determining whether computed values match real-world conditions. It is the process of comparing code results to experimental data and is an essential part of determining whether a code is suitable for use as a design tool. This chapter discusses fission product diffusion validation based on AGR-1 and AGR-2 data.

U.S. Department of Energy (DOE)'s AGR program sponsored a series of irradiation tests on TRISO particle fuel. The first of these, AGR-1, included PIE to characterize the release of silver, cesium, and strontium. The details of AGR-1 are documented elsewhere (see Collin et al. (2015) and the references therein). AGR-2 was similar (Collin, 2018a). Power and temperature for the compacts in these experiments is available as daily values.

The analysis procedure is as follows. To avoid excessive time-consuming calculations of all 4,000 thermal nodes, volume-average values of the whole compact are used to analyze a single particle. The internal temperature of the particle depends on the power level, which provides an energy input due to fission in the fuel kernel, and the temperature at the outer surface of the particle, which is set to the compact average temperature. Fission product transport depends on diffusion coefficients (see Section 2.2), fission yields (see Section 2.3.4), and the computed temperature. The available diffusion coefficients used to model fission product transport in the compact matrix are high enough that they predict all fission products released from the particles are also released by the compacts.

The material in this chapter relies heavily on material in Hales et al. (2020, 2021).

6.1 AGR-1

6.1.1 Silver Release

To compare experimentally measured release fractions of silver, we follow the approach in Collin et al. (2015). In particular, we analyzed the 17 compacts listed in Table 3 of that work and plotted the results in a manner similar to its Figure 5. Our results, shown in Figure 6.1, include values from PIE, the Particle Fuel Model (PARFUME) code, and BISON. As seen from the figure, the BISON results compare very favorably with the PARFUME results.

Note that the calculation of silver release in this section (and of cesium and strontium) relies on effective

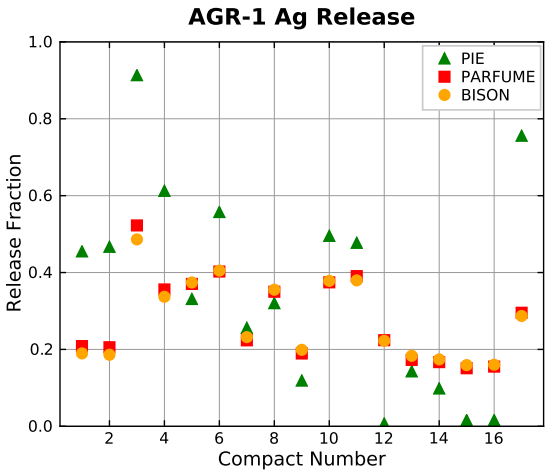

Figure 6.1. Comparison of measured and computed silver release fractions for seventeen compacts (6-4-3, 6-4-1, 6-2-1, 6-1-1, 5-3-3, 5-2-3, 5-1-3, 5-3-1, 4-4-3, 4-3-3, 4-3-2, 4-1-2, 4-4-1, 3-2-3, 3-3-1, 3-2-1, and 1-3-1).

fission yields and does not consider decay. This is done to follow the approach in Collin et al. (2015) and allows valid comparisons to PARFUME data.

6.1.2 Cesium and Strontium Release

The evaluation of cesium and strontium release mostly follows the same approach as for silver release. However, the comparisons for each fission product are made in two parts. In one set of comparisons, only compacts with no known particle failures are included. In the other set, compacts with either one or two failed particles are included.

The analysis procedure for compacts with no known particle failures is exactly the same as that described for silver.

Two analyses were run for each compact with failed particles. The first was the standard analysis already described. In the second, which targeted failed particles, the fission product diffusivity of the SiC layer was set to a large value (10^{-6} m^2/s (Collin et al., 2015)). The release fraction becomes:

$$f_{net} = \frac{f_i(n - n_f) + f_f n_f}{n} \tag{6.1}$$

where f_{net} is the overall release fraction, f_i is the release fraction from the intact particle, f_f is the release fraction from the failed particle, n is the total number of particles in the compact, and n_f is the number of failed particles in the compact.

The results for cesium release with intact particles are found in Figure 6.2, and results for cesium release with failed particles are in Figure 6.3. Aside from Compact 4-4-2, both PARFUME and BISON compute a higher release than seen in PIE for compacts with no failed particles (although for Compact 3-2-1, BISON's

prediction nearly matches the maximum PIE value). Both PARFUME and BISON compute a higher release than seen in PIE for compacts with failed particles. Compared to PARFUME, BISON predicts a slightly lower release for cesium with intact particles and a slightly higher release for cesium with failed particles.

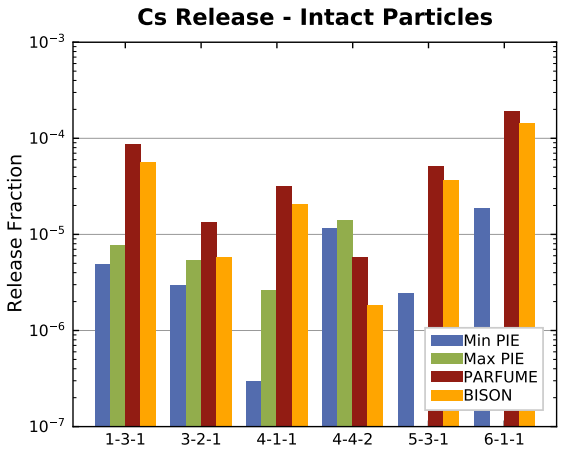

Figure 6.2. Comparison of measured and computed cesium release fractions for six compacts with no failed particles.

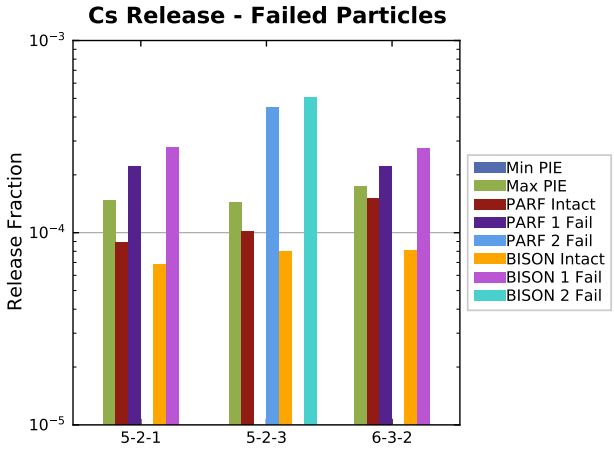

Figure 6.3. Comparison of measured and computed cesium release fractions for three compacts with one or two failed particles.

The results for strontium release with intact particles are in Figure 6.4, and results for strontium release with failed particles are in Figure 6.5. For compacts with intact particles, the PARFUME and BISON results are fairly consistent from compact to compact, while the PIE results show a large variation. These

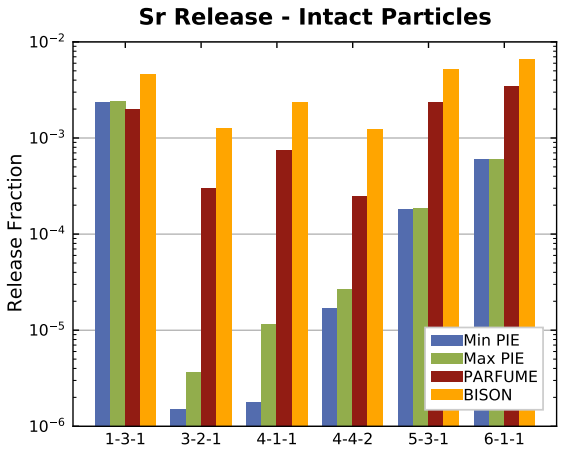

Figure 6.4. Comparison of measured and computed strontium release fractions for six compacts with no failed particles.

results show room for improvement, perhaps in the values of the diffusion coefficients. For compacts with failed particles, both PARFUME and BISON compute a higher release than seen in PIE. Compared to PARFUME, BISON predicts a slightly higher release for strontium, both with intact particles and with failed particles. In the case of strontium, it is interesting to note that predictions change only very slightly with the inclusion of failed particles. This is due to most of the strontium being held in the fuel kernel, never migrating outward to where a failed SiC layer would affect its release.

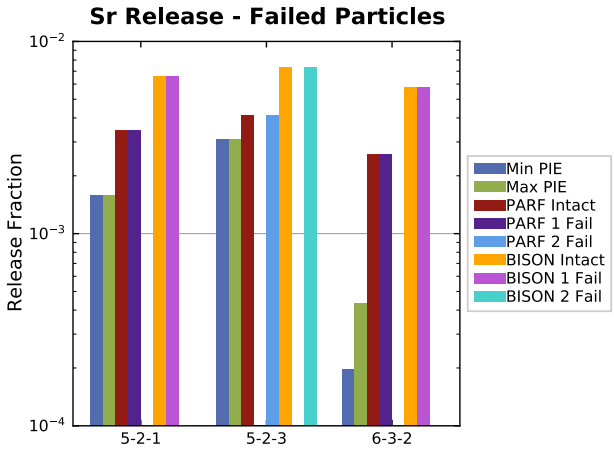

Figure 6.5. Comparison of measured and computed strontium release fractions for three compacts with one or two failed particles.

For silver, cesium, and strontium diffusion in AGR-1, BISON's computed results compare reasonably well to PIE values and values computed by PARFUME. BISON's results were computed using diffusion coefficients in IAE (1997). Considering the four compacts with known lower and upper bounds on release (based on PIE) in Figure 6.2, BISON's results are at or above the upper bound in three of the cases and below the lower bound in the other. Thus, it will likely be difficult to find diffusion model coefficients that accurately compute release fractions for all compacts. Subtleties, such as temperature variations within a compact, may play an important role and need to be included for more accurate validation of AGR-1 fission product release fraction calculations.

6.2 AGR-2

The AGR-2 irradiation occurred over 3.5 years at the Advanced Test Reactor at INL. Compact-average temperature is used as the thermal boundary condition for each day of irradiation. Results from 48 of the AGR-2 compacts are examined here (from Capsules 2, 3, 5, and 6). Some compacts have data available for more than one fission product.

Note that Capsules 2, 5, and 6 contained UCO kernels while Capsule 3 contained UO_2 kernels. The compacts with UCO kernels contained 3,176 kernels, and the compacts with UO_2 kernels contained 1543 kernels (Skerjanc, 2020).

PIE identified the release fraction of silver, cesium, strontium, and krypton for sets of compacts. Release fractions for the irradiation period and for the subsequent safety tests are available. Here we examine release fractions for silver, cesium, and strontium for the irradiation period. Comparisons for these fission products and for krypton during the safety test are underway.

Like for AGR-1, we have chosen to model only a single particle per compact, plus one additional failed particle for a compact if the compact was deemed to contain failed particles.

Results comparing release fractions computed by PARFUME to PIE values were presented in Skerjanc (2020). For the plots in the following subsections that compare BISON results to PIE data and PARFUME calculations, the PIE and PARFUME data points were digitized from that report.

6.2.1 Silver

Fractional release of silver for all 48 compacts within capsules 2, 3, 5, and 6 is available. Figure 6.6 shows the comparison between values computed by BISON and those from PIE and computed by PARFUME. Like for AGR-1 (Hales et al., 2021), BISON results match those of PARFUME very well. However, numerical predictions are generally low compared to PIE data for Capsules 6, 5, and 2. As discussed in Skerjanc (2020), those capsules on average experienced higher temperatures than Capsule 2. Thus, the models may be deficient for high-temperature release.

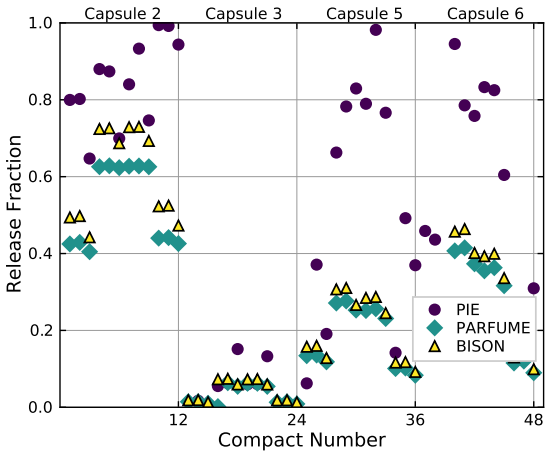

Figure 6.6. Comparison of silver release from PIE, PARFUME, and BISON for 48 compacts. BISON's computed values match those of PARFUME well. Both codes underpredict, in general, the PIE values.

6.2.2 Cesium and strontium, no failed particles

Figure 6.7 shows fractional release of cesium for three compacts at the end of irradiation. It can be seen that BISON results match those of PARFUME. The code predictions match the PIE values for two of the three compacts. For Compact 2-2-1, the predicted values are too high. Capsule 2 experienced relatively high temperatures (Skerjanc, 2020), which suggests that the model may diffuse cesium too readily at high temperatures.

Figure 6.8 shows fractional release of strontium for three compacts at the end of irradiation. The BISON predictions show good agreement with PIE data for two of the three compacts with an over prediction for one compact. BISON's predictions are higher than those of PARFUME, which follows the pattern seen in AGR-1 (Hales et al., 2021).

6.2.3 Cesium and Strontium, Failed Particles

The set of compacts used for comparing fractional release of cesium and strontium where one or more particles failed in the compact are 2-2-3, 5-2-3, 5-3-3, 5-4-2, and 6-2-3. The corresponding number of failed particles in these compacts is 6, 3, 1, 1, and 1.

Figure 6.9 shows fractional release of cesium for five compacts at the end of irradiation. It can be seen that BISON results match those of PARFUME well. The code predictions are within an order of magnitude of the PIE data except for one compact, 2-2-3. Like for the case of intact particles, the greatest overprediction is for a compact from Capsule 2. Since Capsule 2 saw generally higher temperatures, the model may diffuse cesium too readily at high temperatures.

Figure 6.8 shows fractional release of strontium for five compacts at the end of irradiation. The BISON

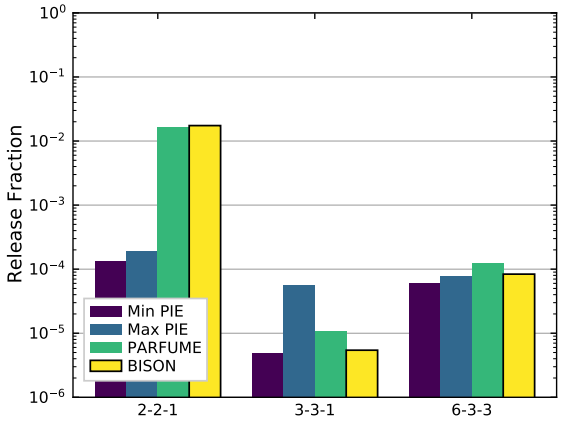

Figure 6.7. Comparison of cesium release from PIE, PARFUME, and BISON for three compacts. BISON's computed values match those of PARFUME well. Both codes overpredict release for compact 2-2-1, which sees a relatively high temperature.

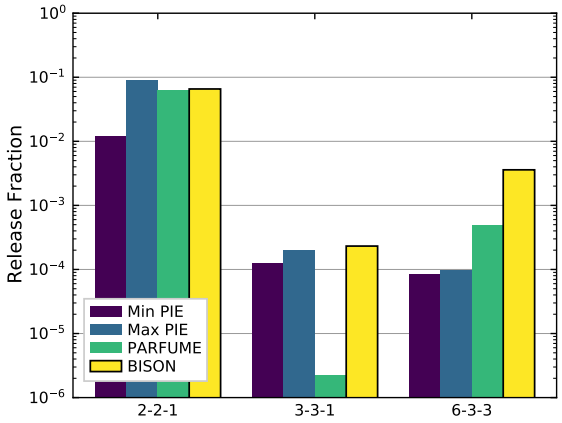

Figure 6.8. Comparison of strontium release from PIE, PARFUME, and BISON for 3 compacts. BISON's computed values are greater than those of PARFUME.

predictions show good agreement with PIE data for two of the three compacts with an over prediction for one compact. BISON's predictions are higher than those of PARFUME, which follows the pattern seen in AGR-1 (Hales et al., 2021).

These results indicate that representing failed particles with highly diffusive layers warrants further investigation. It seems likely that different species in a failed particle would require different diffusivities. Furthermore, a correction of the diffusivities for failed layers would be of greater value if a refined set of

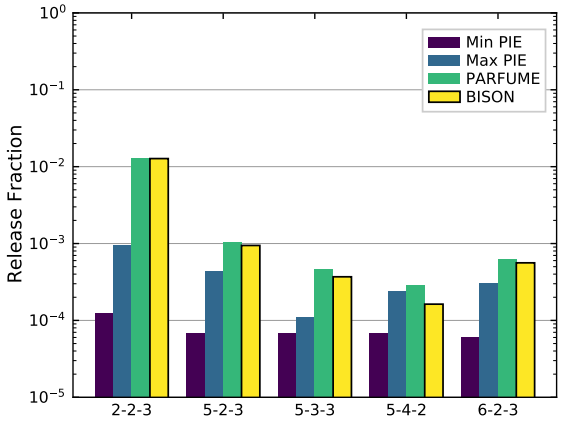

Figure 6.9. Comparison of cesium release from PIE, PARFUME, and BISON for five compacts. BISON's computed values match those of PARFUME well. Both codes tend to overpredict release.

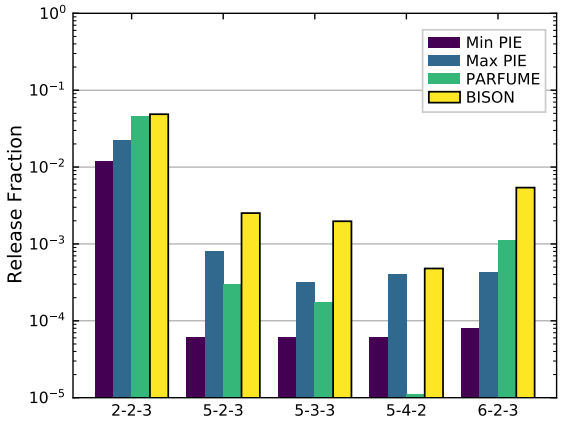

Figure 6.10. Comparison of strontium release from PIE, PARFUME, and BISON for 5 compacts. BISON's computed values are greater than those of from PIE and PARFUME.

diffusivities for intact particles were identified first.

Finally, failed particles are modeled through the use of highly diffusive layers from the beginning of the analysis. Particle failure may occur due to several mechanisms (Jiang et al., 2021) during irradiation or furnace testing. Improved predictions may be possible by estimating the time of particle failure and adjusting diffusivities at that time in the analysis.

7. Fission Product Transport in Fuel Element Matrix

7.1 Fuel Element Matrix Modeling Capability in BISON

Figure 7.1 depicts the BISON capability developed to solve species diffusion within the fuel pebble. This capability utilizes MOOSE's "MultiApps" system to couple TRISO particles Monte Carlo simulation to the pebble diffusion modeling. The fuel pebbles typically consist of over 10,000 five-layer TRISO particles. It would be very difficult to explicitly represent them in the pebble diffusion analysis. Therefore, a homogenization technique is applied to represent pebble as an equivalent continuous medium. The species release from TRISO particles are treated as point sources in the pebble model. The point sources can be directly obtained from the Monte Carlo simulation and their values are transferred to the pebble model at every time step. The failed particles that are identified by the Monte Carlo simulation will change their diffusivity coefficients and become the primary source of fission product transport in the pebble.

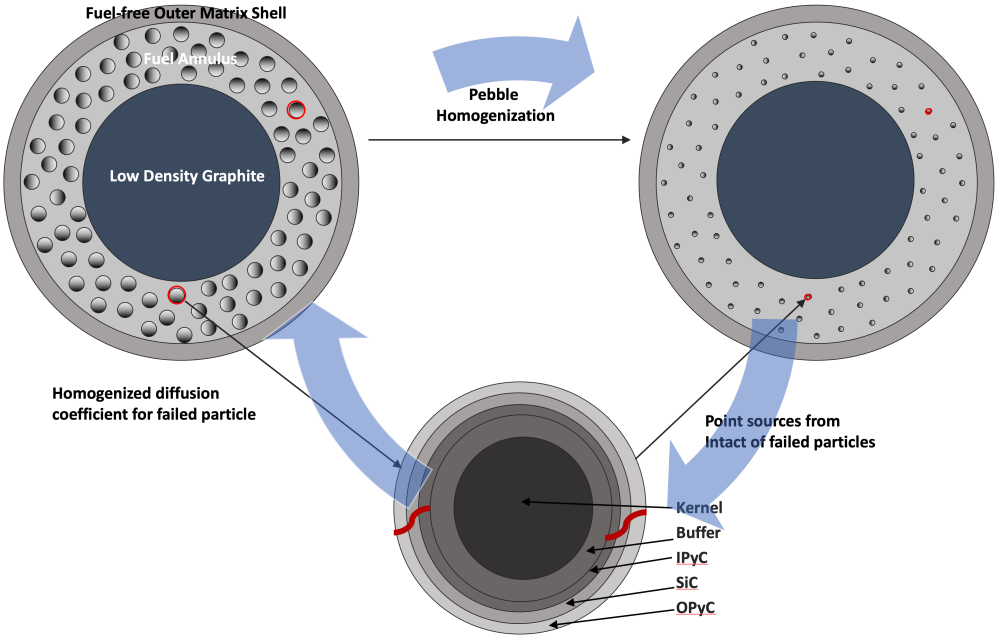

Figure 7.1. BISON pebble modeling illustration.

7.2 Mass Transfer Between the Buffer and IPyC layer

Due to significant shrinkage of the buffer layer under irradiation, a gap is typically formed between the buffer and IPyC layer. For species transport, mass transfer across gaps was modeled using the BISON's `ThermalContact` algorithms. The mass continuity condition is enforced by setting a sufficiently large gap conductivity value. An example of the input block is shown in Listing 7.1.

Alternatively, the mass transfer can be modeled with the `InterfaceKernel` system. An example of the input block is shown in Listing 7.2. The input parameters in the `InterfaceKernel` is easier to understand and avoids the naming confusion of using `GapHeatTransfer` on mass transfer within `ThermalContact` blocks. The comparison of these two mass transfer modeling approaches is shown in Figure 7.2. Their results agree very well.

Listing 7.1. The mass transfer block using `ThermalContact`.

```
[ThermalContact]
  [cesium_contact]
    type = GapHeatTransfer
    variable = conc
    primary = IPyC_left_boundary
    secondary = buffer_right_boundary
    tangential_tolerance = 1e-6
    gap_conductivity_function = d_gap
    gap_conductivity_function_variable = temperature
    appended_property_name = _conc
    quadrature = true
    gap_geometry_type = sphere
    emissivity_primary = 0.0
    emissivity_secondary = 0.0
    min_gap = 1e-7
    sphere_origin = '0 0 0'
  []
[]
```

Listing 7.2. The mass transfer block using `InterfaceKernel`.

```
[InterfaceKernels]
  [conc]
    type = CoupledPenaltyInterfaceDiffusion
    penalty = 10
    primary_coupled_var = conc
    secondary_coupled_var = conc
    boundary = IPyC_buffer
    variable = conc
    neighbor_var = conc
  []
[]
```

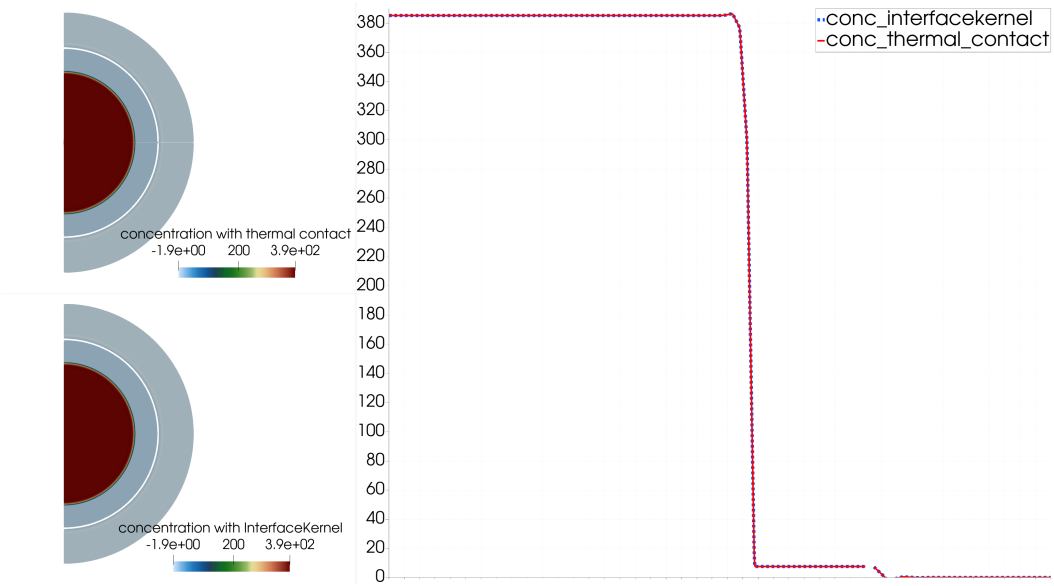

Figure 7.2. Comparison of two mass transfer modeling approaches.

7.3 KP-FHR Fission Product Transport Example

The KP-FHR fuel design is a spherical fuel element, or pebble, containing TRISO particle fuel. The fuel pebble contains an un-fueled central sub-dense core, surrounded by an annular region of TRISO particles packed into a partially-graphitized matrix. The outer layer of the fuel pebble is matrix material used as a protective layer to protect the TRISO particles from mechanical damage. Some key parameters of the generic FHR (https://kairospower.com/generic-fhr-core-model/) are listed in Table 7.1. A 1-D and 3-D finite element pebble model is shown in Figure 7.3 and Figure 7.4, respectively. They have the same number of elements along the radial direction. In this demonstration problem, 10,000 TRISO particles are simulated in the Monte Carlo simulation. The failure probability under the considered irradiation condition is less than 10^{-5}. Because the failure probability is less than $1/n_p$, where n_p is the number of particles in the compact, a given Monte Carlo simulation of that set of particles is unlikely to predict any failed particles. To show the effect of failed particles, 100 particles are manually set to fail in the Monte Carlo simulation. As shown in Figure 7.5, all TRISO particles are randomly located in the fuel annulus region and they are separated by a prescribed minimum distance. The silver concentration at the end of the simulation is shown in Figure 7.6 for 1D and Figure 7.7 for 3D. The 3D plot clearly shows that the primary source of fission product transport comes from those failed particles. As shown in Figure 7.8, the silver release history of 1D and 3D model is indistinguishable. This is largely due to the fact that the diffusion of silver in matrix is so fast that the spatial variation of point sources in 3D space has negligible effect on the silver release. More rigorous comparison between 1D and 3D model will be performed in the future to investigate the effect of mesh size, time step, types of species on the pebble diffusion. The example input file can be found in BISON

repository under `bison/examples/TRISO/pebble`.

Table 7.1. Generic FHR pebble parameters.

Radius (cm)	2.000
Shell layer thickness (cm)	0.200
Fuel layer thickness (cm)	0.420
AGR-5/6/7 TRISO	9022
U-235 enrichment (% WT)	19.55

Figure 7.3. 1-D finite element pebble model.

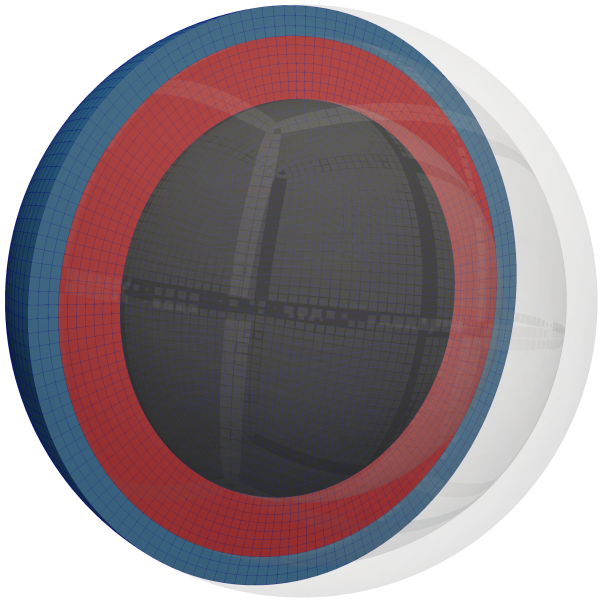

Figure 7.4. 3-D finite element pebble model.

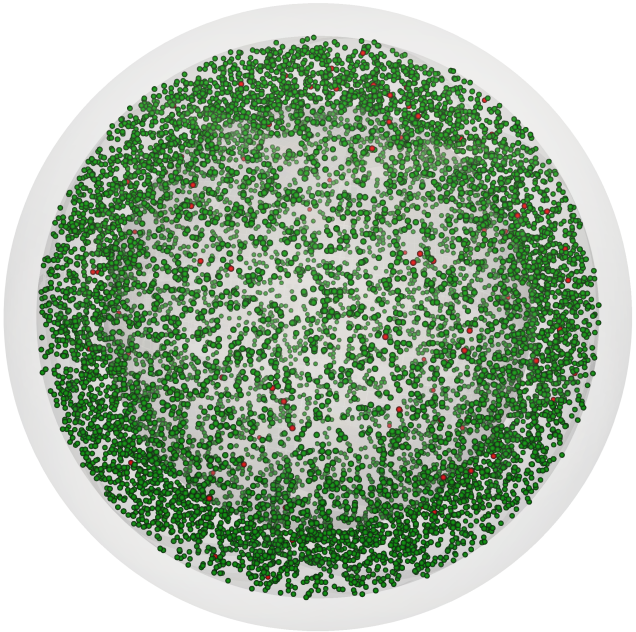

Figure 7.5. 10,000 TRISO particles are generated in the fuel annulus region. The red particles are failed and green particles are intact.

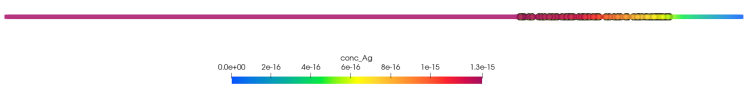

Figure 7.6. Silver diffusion in the 1D pebble (only failed particles are shown).

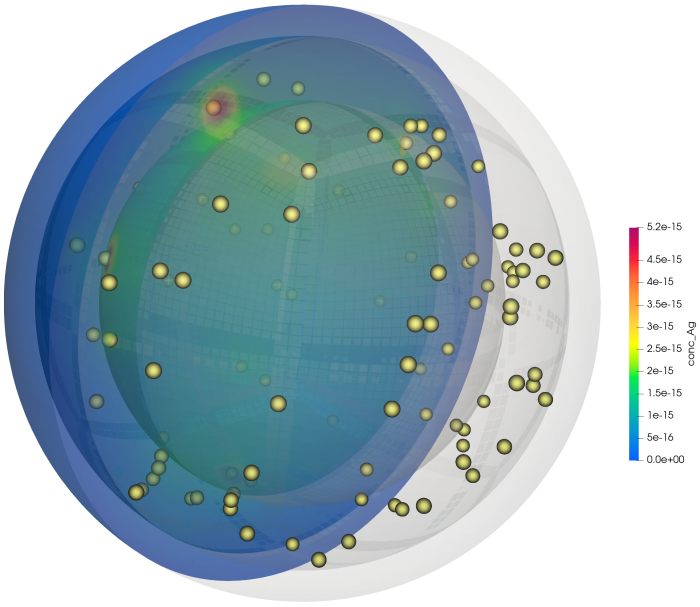

Figure 7.7. Silver diffusion in the 3D pebble (only failed particles are shown).

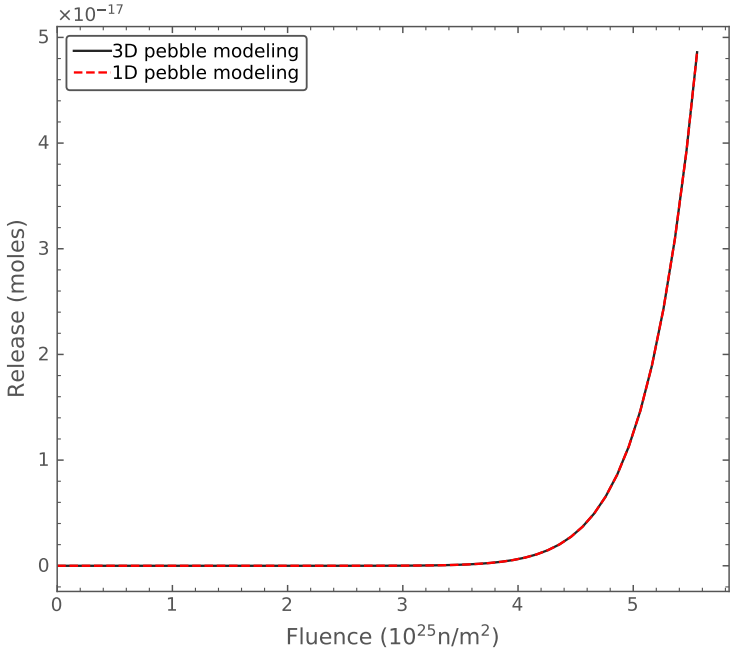

Figure 7.8. Silver release of 1D and 3D pebble simulation.

7.4 Modeling Fission Product Transport in AGR-3/4 Compacts

The BISON compact modeling capability was first applied to the modeling of AGR 3/4 experiments. Each AGR 3/4 compact contains driver fuel particles and 20 Designed-to-Fail (DTF) particles placed along its axis. The fuel compacts are surrounded by three concentric annular rings of a test material consisting of fuel-compact matrix material and fuel-element graphite. Figure 7.9 shows a BISON 3D model, with the DTF particles placed in the center line, and randomly distributed driver particles hosted in the fuel compact. The four regions of the BISON model are the fuel compact, matrix, graphite, and sink. They are separated blocks that do not share nodes between their interfaces. Their height is 12.5 mm, with a compact radius of 6.15 mm and ring wall thicknesses of 6.05, 6.30, and 13.14 mm, respectively.

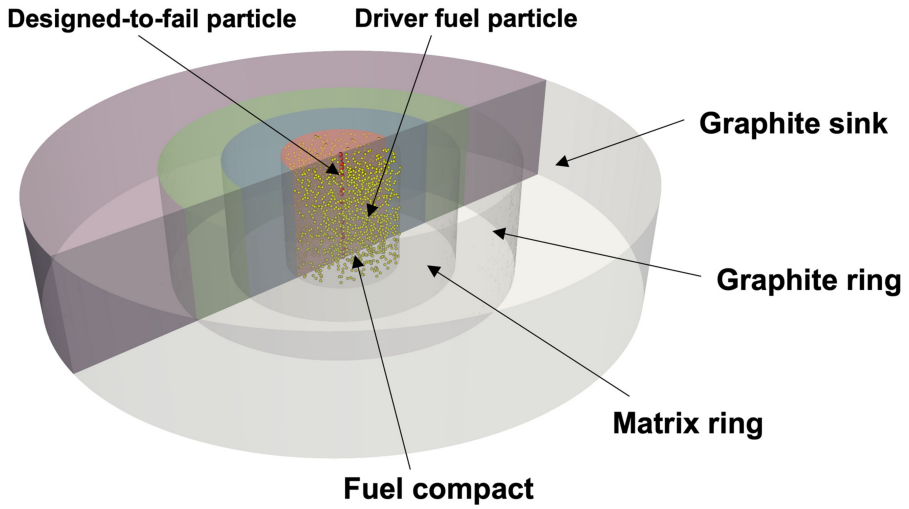

Figure 7.9. AGR 3/4 BISON representation. The four regions of the BISON model are the fuel compact, matrix ring, graphite ring, and graphite sink.

The temperature boundary conditions at the outer fuel compact surface, inner/outer matrix surface, inner/outer graphite surface, and inner/outer sink surface were obtained from prior numerical analysis. The presence of gaps results in discontinuities in the fission product concentration across rings. Established sorption isotherms are used to determine the surface concentration between the two surfaces.

The 1D BISON model was used to calculate the fission product concentration profiles across selected capsules' rings under daily as-run irradiation conditions, and compare them to measured PIE data. The detailed results are found in Skerjanc and Jiang (2021, 2022).

Although 1D simulation is extremely efficient, it might cause inaccuracy when the diffusion process is not uniform along the axial and circumferential direction. For such case, 3D simulation is typically desired. Additionally, a two-way coupling scheme is applied where the power in each particle is applied as heat source terms within the pebble, then the computed temperature within the pebble is assigned to the particle. This

allows for a variety of particle temperatures (according to location within the pebble, which wasn't possible in prior analyses) and thus more detail in fuel particle failure calculations. The code can easily be adapted to assign different powers to different particles for even more detailed calculations. Note that for the sake of efficiency the solution is not iteratively solved between the particle and compact, rather the compact temperature is assigned to the particle at time step begin and the calculations proceeds and updates in the next time step. For more tightly-coupled analysis, the MOOSE `Picard` iteration can be easily applied to make the coupling between the particle and compact solution to iteratively converge at each time step.

We simulated the capsule 7 in AGR-3/4 with both 1D and 3D BISON model. The silver, cesium and strontium concentration along different rings at half and full irradiation time are shown in Figure 7.10, Figure 7.11, and Figure 7.12, respectively. For 3D results, the concentration along the radial direction at different heights of 0m, -0.005m and 0.005m are plotted. Both DTF and driver particles are expected to release some amount of silver and the diffusion is mainly along the radial direction. Therefore the 1D and 3D results agree very well. For cesium, although the release is mainly from DTF, the diffusion is very fast within the graphite and matrix. The 1D and 3D results are comparable. For strontium, the diffusion through the matrix and graphite is very slow. This causes nonuniform diffusion along axial and circumferential directions. This can be seen from the slight different concentration profiles along lines at different heights. There is a large discrepancy between the 1D and 3D results.

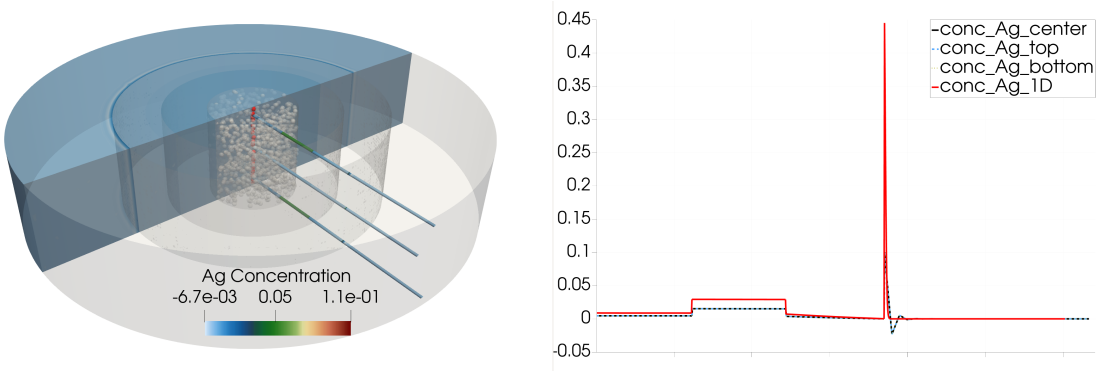

(a) Half irradiation time

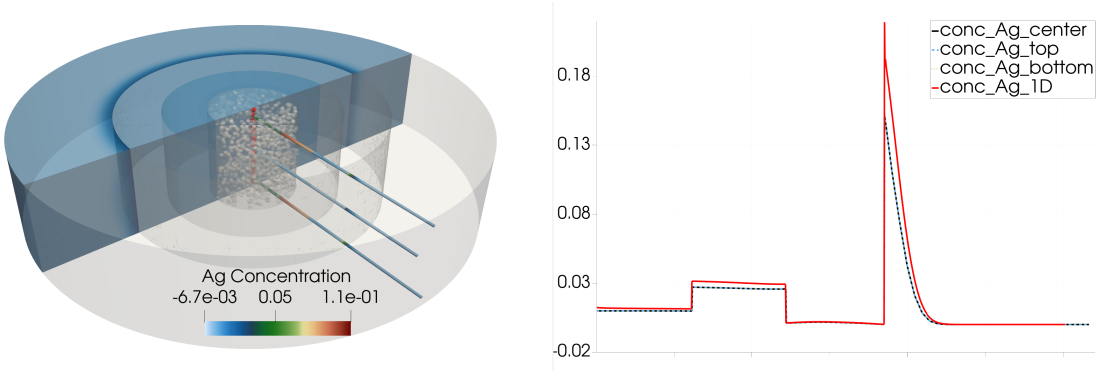

(b) Full irradiation time

Figure 7.10. 1D-3D comparison of silver diffusion of Capsule 7 in AGR-3/4.

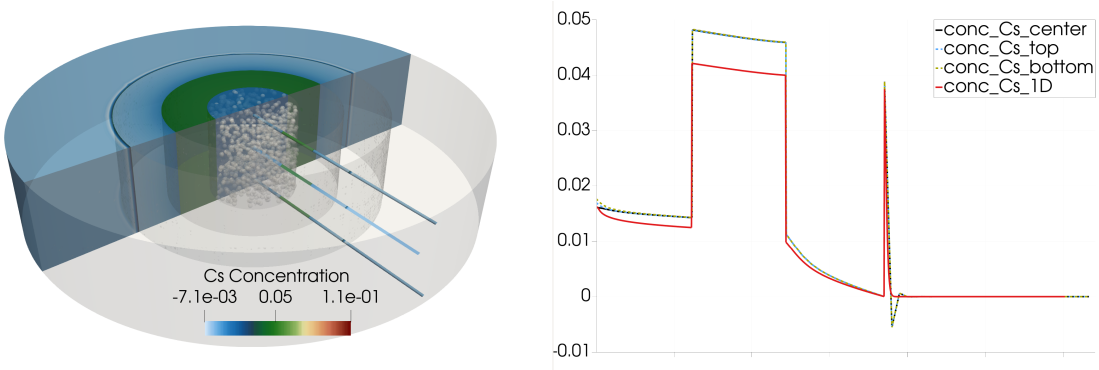

(a) Half irradiation time

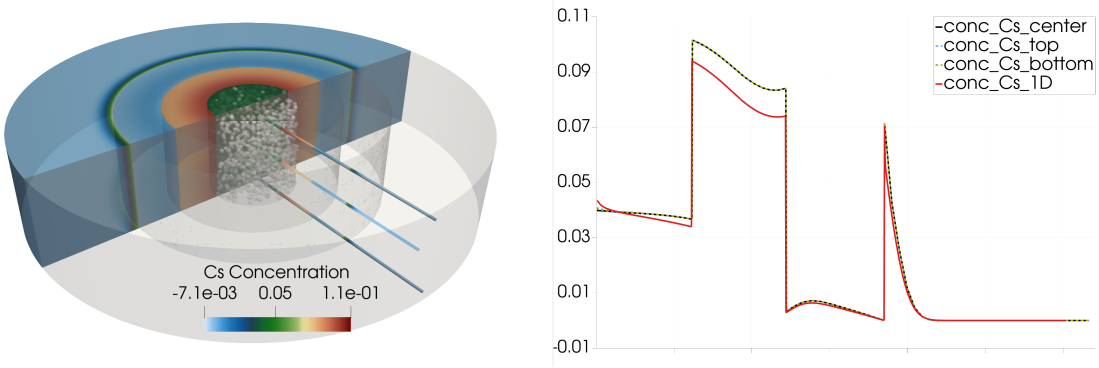

(b) Full irradiation time

Figure 7.11. 1D-3D comparison of cesium diffusion of Capsule 7 in AGR-3/4.

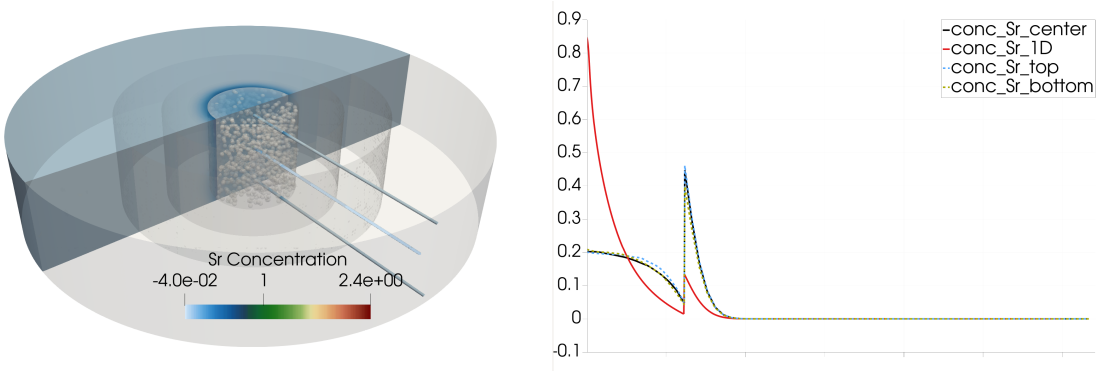

(a) Half irradiation time

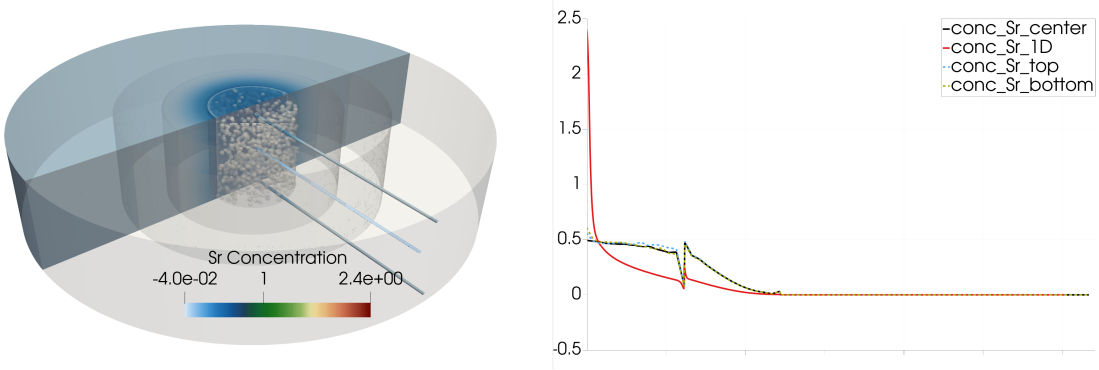

(b) Full irradiation time

Figure 7.12. 1D-3D comparison of strontium diffusion of Capsule 7 in AGR-3/4.

8. Conclusion and Future Work

This report documents completion of the milestone titled, "Establish 1D and 3D fission product transport capability in support of particle and pebble analysis," as specified in the FOA (LLC et al., 2018). BISON has expanded to include many advancements in the areas of mesh generation, failure probability, homogenization, and integrated TRISO-pebble simulation capability during the course of this project. This report also demonstrates verification of physics simulations that are critical to effective simulation of particle fuel. Further understanding of BISON simulation capabilities are shown via simulations and comparisons to measurements of the AGR-1-4 experiments. This work has enabled the capability to perform fission product release estimates as shown in the demonstration model of chapter Chapter 7, which will serve as a starting point to build specific models used in future licensing activities.

Future work plans include:

- Application of linear fracture mechanics to crack propagation in TRISO coating layers resulting in more accurate predictions in failure analysis
- Implementation of inter-layer sorptivity will result in more accurate and robust fission product release calculations
- Pd-SiC interactions, which will account for degradation of the SiC layer and could be applied to metallic interactions on the outside of the pebble and particle due to Flibe infiltration

Bibliography

Mass diffusion analysis. `https://abaqus-docs.mit.edu/2017/English/SIMACAEANLRefMap/simaanl-c-massdiffusion.htm`. Accessed: 2021-06-01.

Fuel performance and fission product behavior in gas cooled reactors. Technical Report IAEA-TECDOC-978, IAEA, 1997.

V. Barabash, I. Mazul, R. Latypov, A. Pokrovsky, and C.H. Wu. The effect of low temperature neutron irradiation and annealing on the thermal conductivity of advanced carbon-based materials. *Journal of Nuclear Materials*, 307-311:1300–1304, 2002. doi:10.1016/S0022-3115(02)00961-3.

A. H. Booth. A method of calculating gas diffusion from UO_2 fuel and its application to the X-2-f loop test. Technical Report AECL-496, Atomic Energy of Canada Ltd., 1957.

H. S. Carslaw and J. C. Jaeger. *Conduction of heat in solids*. Oxford University Press, 2nd edition, 1959.

B. P. Collin. AGR-2 Irradiation Test Final As-Run Report. Report INL/EXT-14-32277 (Rev.4), Idaho National Laboratory, 2 2018a.

B. P. Collin, D. A. Petti, P. A. Demkowicz, and J. T. Maki. Comparison of silver, cesium, and strontium release predictions using PARFUME with results from the AGR-1 irradiation experiment. *Journal of Nuclear Materials*, 466:426 – 442, 2015. ISSN 0022-3115. doi:10.1016/j.jnucmat.2015.08.033.

F. Deng and Q. Zheng. Interaction models for effective thermal and electric conductivities of carbon nanotube composites. *Acta Mechanica Solida Sinica*, 22(1):1–17, 2009. doi:10.1016/S0894-9166(09)60085-9.

J. K. Fink. Thermophysical properties of uranium dioxide. *Journal of Nuclear Materials*, 279:1–18, 2000. doi:10.1016/S0022-3115(99)00273-1.

J. Floury, J. Carson, and Q. T. Pham. Modelling thermal conductivity in heterogeneous media with the finite element method. *Food Bioprocess Technol*, 1:161–170, 2008. doi:10.1007/s11947-007-0001-6.

C. Folsom, C. Xing, C. Jenson, H. Ban, and D. Marshall. Experimental measurement and numerical modeling of the effective thermal conductivity of TRISO fuel compacts. *Journal of Nuclear Materials*, 458:198–205, 2015. doi:10.1016/j.jnucmat.2014.12.042.

R. Gontard and H. Nabielek. Performance Evaluation of Modern HTR TRISO Fuels. Report HTA-1B-05/90, Forschungszentrums Juelich, July, 1990.

J. Hales, S. R. Novascone, B. W. Spencer, R. L. Williamson, G. Pastore, and D. M.Perez. Verification of the BISON fuel performance code. *Annals of Nuclear Energy*, 71:2014, 81–90. doi:10.1016/j.anucene.2014.03.027.

J. D. Hales, R. L. Williamson, S. R. Novascone, D. M. Perez, B. W. Spencer, and G. Pastore. Multidimensional multiphysics simulation of TRISO particle fuel. *Journal of Nuclear Materials*, 443(1):531–543, 11 2013. doi:10.1016/j.jnucmat.2013.07.070.

J. D. Hales, W. Jiang, A. Toptan, and K. Gamble. BISON TRISO Modeling Advancements and Validation to AGR-1 Data. PEMP Notable Outcome 1.1.C Completion Report INL/EXT-20-59368, Idaho National Laboratory (INL), Idaho Falls, ID United States, 2020.

J. D. Hales, W. Jiang, A. Toptan, and K. A. Gamble. Modeling fission product diffusion in TRISO fuel particles with BISON. *Journal of Nuclear Materials*, 548:152840, 2021. doi:10.1016/j.jnucmat.2021.152840.

F. Ho. NP-MHTGR: Material Models of Pyrocarbon and Pyrolytic Silicon Carbide. Report CEGA-002820 Rev. 1, CEGA Corporation, July, 1993.

W. Jiang, B. W. Spencer, and J. E. Dolbow. Ceramic nuclear fuel fracture modeling with the extended finite element method. *Engineering Fracture Mechanics*, 223:106713, January 2020. doi:10.1016/j.engfracmech.2019.106713.

W. Jiang, J. D. Hales, B. W. Spencer, B. Collin, A. E. Slaughter, S. R. Novascone, A. Toptan, K. A. Gamble, and R. Gardner. TRISO particle fuel performance modeling and failure analysis with BISON. *Journal of Nuclear Materials*, 548:152795, 2021. doi:10.1016/j.jnucmat.2021.152795.

W. Jiang, G. Singh, J. D. Hales, A. Toptan, B. W. Spencer, S. R. Novascone, S. L. N. Dhulipala, and Z. M. Prince. Efficient high-fidelity TRISO statistical failure analysis using bison: Applications to AGR-2 irradiation testing. *Journal of Nuclear Materials*, 562:153585, 2022. doi:10.1016/j.jnucmat.2022.153585.

J. Kamm, W. Rider, and J. Brock. Combined space and time convergence analysis of a compressible flow algorithm. *AIAA Paper*, 2003-4041. doi:10.2514/6.2003-4241.

U. Littmark and J. F. Ziegler. Handbook of Range Distributions for Energetic Ions in All Elements. Technical report, Pergamon Press, 1980.

Kairos Power LLC, Idaho National Laboratory, Argonne National Laboratory, and Los Alomos National Laboratory. Modeling and Simulation Development Pathways to Accelerating KP-FHR Licensing. Report U.S. DOE FOA No. 001817, Kairos Power LLC, 10 2018.

G. K. Miller, D. A. Petti, J. T. Maki, D. L. Knudson, and W. F. Skerjanc. PARFUME Theory and Model Basis Report. Report INL/EXT-08-14497 (Rev.1), Idaho National Laboratory, September, 2018.

D. Mu, ZS. Liu, C. Haung, and N. Djilali. Prediction of the effective diffusion coefficient in random porous media using the finite element method. *J. Porous Mater.*, 14:49–54, 2007. doi:10.1007/s10934-006-9007-0.

H. Nabielek, H. Hick, M. Wagner-Löffler, and E. H. Voice. Performance limits of coated particle fuel, Part III: Fission product migration in HTR fuel. Tech. Rep. DP-Report-828(Pt.3), O.E.C.D High Temperature Reactor Project Dragon, 6 1974.

H. Nabielek, K. Fukuda, K. Minato, and T. Ogawa. Calculation of Particle Temperatures in NSRR Tests. Unpublished draft, Japanese Atomic Energy Agency, March, 1992.

L. E. Nielsen. The thermal and electrical conductivity of two-phase systems. *Ind. Eng. Chem. Fundam.*, 13 (1):17–20, 1974. doi:10.1021/i160049a004.

W. L. Oberkampf and C. J. Roy. *Verification and Validation in Scientific Computing*. Cambridge University Press, Cambridge, UK, first edition, 11 2010.

D. R. Olander. *Fundamental aspects of nuclear reactor fuel elements*. Technical Information Center, Energy Research and Development Administration, 1976.

D. Petti, P. Martin, M. Phelip, and R. Ballinger. Development of improved models and designs for coated-particle gas reactor fuels. Technical Report INL/EXT-05-02615, Idaho National Engineering and Environmental Laboratory, December, 2004.

J. J. Powers and B. D. Wirth. A review of TRISO fuel performance models. *J Nuclear Materials*, 405(1): 74–82, 2010. doi:10.1016/j.jnucmat.2010.07.030.

W. F. Skerjanc. Comparison of fission product release predictions using PARFUME with results from the AGR-2 irradiation experiment. Technical Report INL/EXT 20 59448, Idaho National Laboratory, 8 2020.

W. F. Skerjanc and W. Jiang. Bison as-run agr-3/4 irradiation test predictions. Tech. Rep. INL/EXT-21-65160, INL, Idaho Falls, ID (United States), 11 2021.

W. F. Skerjanc and W. Jiang. Comparison of fission product release predictions using PARFUME and BISON with results from the AGR-3/4 irradiation experiment. Tech. Rep. INL/RPT-22-69003, INL, Idaho Falls, ID (United States), 9 2022.

L. L. Snead, T. Nozawa, Y. Katoh, T.-S. Byun, S. Kondo, and D. A. Petti. Handbook of SiC properties for fuel performance modeling. *Journal of Nuclear Materials*, 371:329–377, 2007. doi:10.1016/j.jnucmat.2007.05.016.

R. Stainsby et al. Investigation of local heat transfer phenomena in a pebble bed HTGR core. Technical Report NR001/RP/002 R01, AMEC, 5 2009. URL `https://www.nrc.gov/docs/ML0909/ML090900017.pdf`.

A. Toptan, D. J. Kropaczek, and M. N. Avramova. On the validity of dilute gas assumption for gap conductance calculations in nuclear fuel performance codes. *Nuclear Engineering and Design*, 350:1–8, 2019. doi:10.1016/j.nucengdes.2019.04.042.

A. Toptan, J. D. Hales, R. L. Williamson, S. R. Novascone, G. Pastore, and D. J. Kropaczek. Modeling of gap conductance for LWR fuel rods applied in the BISON code. *J. Nucl. Sci. Tech.*, 57(8):963–974, 2020a. doi:10.1080/00223131.2020.1740808.

A. Toptan, N. W. Porter, J. D. Hales, B. W. Spencer, M. Pilch, and R. L. Williamson. Construction of a code verification matrix for heat conduction with finite element code applications. *ASME J. Verif. Valid. Uncert.*, 5(4):041002 (15 pages), 2020b. doi:10.1115/1.4049037.

A. Toptan, N. W. Porter, J. D.. Hales, R. L. Williamson, and M. Pilch. FY20 verification of BISON using analytic and manufactured solutions. Technical Report CASL-U-2020-1939-000; SAND2020-3887R, Consortium for Advanced Simulation of LWRs (CASL), 3 2020c.

A. Toptan, W. Jiang, J. D. Hales, A. Casagranda, and S. R. Novascone. FEA-aided investigation of the effective thermal conductivity in a medium with embedded spheres. *Nuclear Engineering and Design*, 381: 111355:1–16, 9 2021. doi:10.1016/j.nucengdes.2021.111355.

A. Toptan, W. Jiang, and J. D. Hales. Analytical homogenization techniques applied to the fickian diffusion: Effective diffusivity coefficient. In *ANS Winter Meeting and Technology Expo: Materials Science and Technology (MSTD), Nuclear Fuels*, Phoenix, AZ United States, November 13-17 2022a.

A. Toptan, N. W. Porter, J. D. Hales, W. Jiang, B. W. Spencer, and S. R. Novascone. Verification of MOOSE/Bison's heat conduction solver using combined spatiotemporal convergence analysis. *ASME Journal of Verification, Validation and Uncertainty Quantification*, 7(2):021006:1–18, 2022b. ISSN 2377-2158. doi:10.1115/1.4054216.

A. Toptan, W. Jiang, J. D. Hales, B. W. Spencer, and S. Novascone. Verification of the Bison fission product species conservation under TRISO reactor conditions. *Journal of Nuclear Materials*, 573:154105:1–17, 1 2023. doi:10.1016/j.jnucmat.2022.154105.

J. A. Turnbull, C. A. Friskney, J. R. Findlay, F. A. Johnson, and A. J. Walter. The diffusion coefficients of gaseous and volatile species during the irradiation of uranium dioxide. *Journal of Nuclear Materials*, 107: 168–184, 1982. doi:10.1016/0022-3115(82)90419-6.

I. J. van Rooyen, M. L. Dunzik-Gougar, and P. M. van Rooyen. Silver (Ag) transport mechanisms in TRISO coated particles: A critical review. *Nuclear Engineering and Design*, 271:180 – 188, 2014. doi:10.1016/j.nucengdes.2013.11.029.

K. Verfondern. 3.24 - TRISO fuel performance modeling and simulation. In R. J. M. Konings, editor, *Comprehensive Nuclear Materials*, pages 755–788. Elsevier, Oxford, 2012. doi:10.1016/B978-0-08-056033-5.00076-8.

E. W. Weisstein. "cubic formula." from mathworld–a wolfram web resource. Available at `http://mathworld.wolfram.com/cubicformula.html` [Online; accessed August 8, 2019].

R. L. Williamson, J. D. Hales, S. R. Novascone, G. Pastore, K. A. Gamble, B. W. Spencer, W. Jiang, S. A. Pitts, A. Casagranda, D. Schwen, A. X. Zabriskie, A. Toptan, R. J. Gardner, C. Matthews, W. Liu, and H. Chen. BISON: A flexible code for advanced simulation of the performance of multiple nuclear forms. *Nuclear Technology*, 207(7):954–980, 2021. doi:10.1080/00295450.2020.1836940.

W. C. Young and R. G. Budynas. *Roark's Formulas for Stress and Strain*. McGraw-Hill, New York, NY, 7th edition, 2002.

O. C. Zienkiewicz, R. L. Taylor, and J. Z. Zhu. *The Finite Element Method Its Basis & Fundamentals*. Elsevier, New York, NY, 2013. doi:10.1016/C2009-0-24909-9.